Analysis of MBE-grown II-VI Hetero-Interfaces and Quantum-Dots by Raman Spectroscopy

Dissertation zur Erlangung des naturwissenschaftlichen Doktorgrades der Julius-Maximilians-Universität Würzburg

vorgelegt von
Diplom Physiker Utz Baß
aus Reutlingen

Würzburg, Dezember 2011

Eingereicht am: 23.12.2011
bei der Fakultät für Physik und Astronomie

1. Gutachter: Prof. Dr. J. Geurts
2. Gutachter: Prof. Dr. J. Pflaum
3. Gutachter: Prof. Dr. R. Oppermann
der Dissertation.

Vorsitzender(r) Prof. Dr. A. Denner
1. Prüfer: Prof. Dr. J. Geurts
2. Prüfer: Prof. Dr. J. Pflaum
3. Prüfer: Prof. Dr. R. Oppermann
im Promotionskolloquium

Tag des Promotionskolloquiums: 16.10.2012

Doktorurkunde ausgehändigt am: .....

Contents

Chapter 1

Introduction

The material system of interest in this thesis are II-VI-semiconductors. As shown in fig. 1.1, the energy gap values of this material system cover an extremely wide range. Wide bandgap II-VI semiconductors, especially on the basis of ZnSe, CdSe and CdTe, have found great interest with regard to their opto-electronic properties and also because of their suitability as basic material system for spintronics. For these applications generally heterostructures are employed. Moreover, often the special features of quantum dots are exploited.

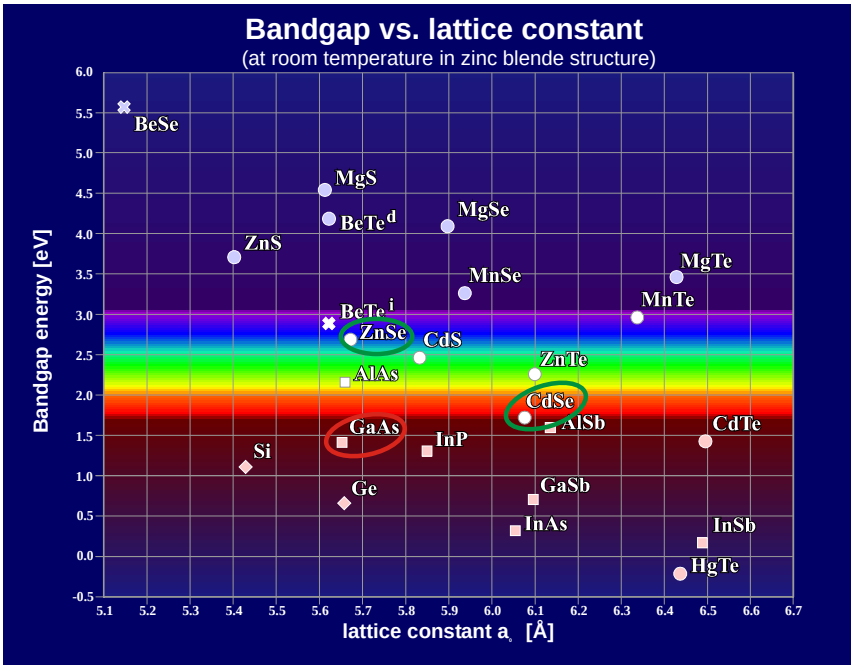

Figure 1.1: Fundamental bandgap energy E_g of binary compounds and the corresponding lattice constant a_0. The visible spectral range is indicated by the "rainbow coloured" region.

A quantum dot (QD) is a material object whose size is in the range of the wave-function of electrons/excitons. This confinement in three dimensions makes them perfect candidates for fundamental research of a zero dimension system. The impact implies basic

research as well as numerous applications:

- The optical absorption properties of QD are of high interest in the construction of solar cells with high efficiency. As the material and size of a QD determines its energy levels, it is possible to tailor them to a specific absorption wavelength.

  This concept applies to the visible (Kam08) and also to the near-infrared energy (LEEN$^+$07). The implementation of QDs in solar cells also includes organic solar cells and several concepts exist which take advantage of the possible positive effects on solar conversion (e.g. achieving up to 66% efficiency) (Noz02). Some of the envisaged improvements are still under discussion like overcoming the "phonon bottleneck", which is a crucial aspect of hot exciton relaxation (KKP09).

- In contrast to the absorption also the emission of light can be exploited. For example the application of QDs as active medium in Lasers for the telecommunication market. In the wavelength region $\approx$ 1.15 - 1.25 μm used in medical application, QD lasers play a prominent role (Led11).

- Besides the excitonic properties of a QD also the charging of a QD enables fundamental physics studies and applications. For instance in the case of a gated QD, it is possible to operate that device in a way of a single electron transistor (GRuKE11). This is a promising approach to keep Moores Law valid.

- Another striking feature of QDs concerns the spin of an included electron. For example the spin relaxation time of an electron in a QD is significantly enhanced and enables the construction of devices with totally new properties. This ranges from spin filters (FSE04) via spin memory (RSL00) to entangled states of two QDs (KCG$^+$11) which enable quantum computing or can be used in cryptography (LKS08).

The first part of this thesis focuses on the formation of self-assembled CdSe-based QDs on ZnSe. The lattice constants of ZnSe and CdSe differ as much as about 7% (see fig. 1.1) and therefore a CdSe layer grown on top of ZnSe experiences a huge strain. The aspired strain relief constitutes in the self-assembly of quantum dots (QD) (i.e. a roughened layer structure). This QD formation is by far less straightforward than the classical Stranski-Krastanow growth mode of III-V compound systems, such as e.g. (In,Ga)As on GaAs. Crucial effects in the II-VI QD formation are intermixing between the QD material and the underlying layer, as well as a thickness-dependent surface roughening instead of the canonical formation of QDs on a well-defined wetting layer in the Stranski-Krastanow mode. For CdSe on ZnSe, in Molecular Beam Epitaxy (MBE), various QD growth procedures are applied, resulting in different morphologies and areal densities of QDs, which consist of the non-stoichiometric ternary (Zn,Cd)Se, in which the intermixing of the Cd with the Zn from the underlying layer is an effective way to relieve the strain imposed on the CdSe layer. Central questions regarding the QDs are the material composition, i.e. the relative fractions of Zn and Cd, and the electronic band gap energy, as well as the interdependence of these properties and their development with increasing nominal CdSe

layer thickness.
ZnSe-based II-VI heterostructures are most commonly grown on GaAs substrates. As seen from fig 1.1, these both compounds are almost ideally lattice matched, the relative mismatch is as low as 0.27%. For the optimization of the ZnSe/GaAs interface two criteria have to be considered: (i) the crystalline quality, (ii) the electronic characteristics. The latter aspect is non-trivial because of the different valences of the cations and anions on both sides of this heterovalent interface. Different growth start procedures of the ZnSe epilayer may lead to different interface configurations with characteristic band-offsets and carrier depletion layer widths. The optimum may well depend an the envisaged application, i.e. the optimum configuration for optoelectronic devices which require a rather high current density may be different from that for low-current spin-polarized transport in spintronics applications. For these interfaces, a non-destructive analysis of the electronic properties, especially the depletion layer on each interface side, is highly desirable. This question is in the focus of the second part of this thesis.
The most prominent analysis method in this thesis is inelastic light scattering, Raman spectroscopy. By this non-destructive optical technique information is obtained about various sample properties. The most common application is Raman scattering from phonons. Besides material identification and crystalline quality assessment, this type of Raman scattering is also applied for the determination of strain and for compositional analysis of non-stoichiometric compounds. Because of these abilities it is eligible for the study of the intermixed and partially strained CdSe QDs on ZnSe. The successful application in this case is based on the exploitation of resonant Raman scattering. Here the resonance of the laser light excitation with an electronic transition yields the sensitivity which is required for analysing extremely low scattering volumina like QDs. Moreover, it gives the necessary selectivity for individual materials in heterostructures. Beside lattice-specific information from phonon Raman scattering, also information on free electrons in doped materials is obtained in scattering from coupled plasmon-phonon modes. They may yield carrier concentration and mobility. In this thesis, plasmon-phonon (PLP) modes are studied in heterostructures of n-doped GaAs and n-doped ZnSe, grown with different MBE growth-start procedures. From these PLP modes together with the LO phonons at the ZnSe/GaAs interfaces, the individual depletion layer widths at each side of the interface are quantitatively evaluated.
As an additional optical method photoluminescence (PL) is applied. Its aim is twofold. First, interband PL represents the bandgap energy, which is especially relevant for the various QDs, while PL from local centers reveals the incorporation of different atoms or the formation of vacancies, defects etc. Secondly, the PL-derived bandgap energies are applied in Raman spectroscopy for the appropriate choice of the laser line in order to achieve optimum conditions for resonant Raman scattering.
This thesis is ordered as follows: After the introduction (chapter 1), the fundamental aspects are discussed in part I, consisting of the chapters 2 and 3. They cover the Raman scattering theory (chapter 2) and the lattice dynamics and electronic properties of the relevant material systems (chapter 3). Subsequently, part II comprises in chapters 4 and 5 the presentation and discussion of the results. Chapter 4 addresses the epitaxial CdSe

quantum dots grown on ZnSe with different growth techniques, while chapter 5 deals with the interface between n-ZnSe and n-GaAs with reference to the impact of the ZnSe growth start procedure. Finally, the results are summarised in chapter 6.

Part I

Fundamentals

Chapter 2

Raman Scattering

2.1 Microscopic theory of phonon scattering

The principle of Raman scattering is described basically within the framework of the microscopic theory (YC01). It consists of a three-step process:

- The incident photon ω_i creates an excited state $|a\rangle$ in the medium (e.g. electron-hole pair)
- The electron-hole pair looses energy via the creation of a phonon (or gains energy by annihilation of an existing phonon) and is thus now in the state $|b\rangle$.
- Finally the electron-hole pair $|b\rangle$ recombines by emitting a photon ω_s

As this is a quantummechanical description of the Raman scattering process, the uncertainty principle applys. For the total process, energy conservation applies, but as the process is happening on a fast timescale the single steps can also be virtual.

This is reflected in the scattering probability which will be described here after the energy and momentum description. When a phonon is created its energy amounts to

$$\hbar\omega_{ph} = \hbar\omega_i - \hbar\omega_s. \tag{2.1}$$

As seen from eq. 2.1 the phonon frequency equals the energy difference of the two photons. In the common case of the Stokes Raman process which creates a phonon in the medium, the incident photon looses part of its energy. It is also possible that the incident photon gains energy by annihilation of an existing phonon, this process is called anti-Stokes scattering. The investigation of the anti-Stokes scattering is not very common, as Raman scattering is generally regarded as an energy loss spectroscopy. The frequency shift of the scattered photon with respect to the incident one is called Raman shift and is the abscissa of a Raman spectrum. The ordinate is the scattered phonon intensity.

Besides the photon energy shift also the change in momentum q has to be regarded. The maximum q change occurs in backscattering geometry. As the energy of the photon in Raman scattering is only slightly changed, the following approximation is valid:

$$q_{ph} = k_i - k_s \approx 2k_i \tag{2.2}$$

When assuming a refractive index n = 3, then for photons in the visible spectral range the maximum momentum values of the phonon wavevector q_{ph} range from amount to $0.52{\cdot}10^6 cm^{-1}$ for λ_i = 760 nm to $0.94{\cdot}10^6 cm^{-1}$ for λ_i = 400 nm. This limits the creation of a single phonon to the center of the Brillouin zone.

The scattering efficiency is calculated in the framework of third order perturbation theory and Fermis Golden Rule (Ric76). The main contribution to the susceptibility is given by

$$\chi_{\alpha,\beta}(\omega_i,\omega_s) \propto \sum_{a,b} \frac{\langle 0|\, p_s\, |b\rangle \langle b|\, H_{EL}\, |a\rangle \langle a|\, p_i\, |0\rangle}{(E_b - \hbar\omega_s)(E_a - \hbar\omega_i)}. \tag{2.3}$$

With p_s, p_i being the vector components of the dipole operator of the scattered and incident photon, H_{EL} describes the Hamiltonian of the electron-phonon interaction and E_a, E_b are the energies of the electronic states. The crucial consequence of eq. 2.3 is the enhancement of the scattering intensity when the incident and/or scattered photon energy is close to an electronic transition. The scattering efficiency for a common experiment (off resonant conditions) is in the range of $1{\cdot}10^{-6}$-10^{-7} (Lou63). This low scattering probability can be enhanced by resonant Raman scattering about several orders of magnitude. Of course Raman scattering with non-zero intensity only occurs for the numerator of eq. 2.3 being nonzero. This condition is determined by group theory rules. The possible polarization configurations are comprised in the Raman tensors eq. 2.15. The above statements only apply for first-order Raman scattering. The main difference for higher order scattering is that the phonons do not only arise from the Brillouin zone center. Two phonons with opposite q-vectors can be generated and thus fullfill the momentum conservation. The density of states determines which phonons contribute mostly to the Raman scattering intensity.

2.2 Macroscopic theory of light-wave interaction with lattice vibrations

The macroscopic theorie describes Raman scattering on the level of the interaction of an electromagnetic wave with a lattice deformation wave by means of a generalized model of the dielectric susceptibility (YC01). The electrical field of an electromagnetic wave in the medium can be described by

$$\mathbf{F}(\mathbf{r},\mathbf{t}) = \mathbf{F_i}(\mathbf{k_i},\omega_\mathbf{i})\mathbf{cos}(\mathbf{k_i}\cdot\mathbf{r} - \omega_\mathbf{i}\mathbf{t}). \tag{2.4}$$

This field induces a polarization $\mathbf{P}(\mathbf{r},t)$ in the medium of the form of a sinusoidal wave:

$$\mathbf{P}(\mathbf{r},\mathbf{t}) = \mathbf{P}(\mathbf{k_i},\omega_\mathbf{i})\mathbf{cos}(\mathbf{k_i}\cdot\mathbf{r} - \omega_\mathbf{i}\mathbf{t}). \tag{2.5}$$

For a rigid crystal without lattice vibrations the frequency and wavevector of the polarization reflect the corresponding values of the incident light wave. The proportionality of the polarization and the electric field is given by the susceptibility χ.

$$\mathbf{P}(\mathbf{k_i},\omega_\mathbf{i}) = \epsilon_\mathbf{0}\chi(\mathbf{k_i},\omega_\mathbf{i})\mathbf{F_i}(\mathbf{k_i},\omega_\mathbf{i}). \tag{2.6}$$

In the visible spectral range the dielectric susceptibility χ is governed by the electronic excitations. Their eigenfrequencies are about two orders of magnitude beyond those of the lattice vibrations. However, the susceptibility χ is influenced by some degree by the phononic atom movement. In the presence of lattice vibrations the dielectric susceptibility may be modulated by a contribution with the lattice vibration frequency. The atomic displacement of such a lattice oscillation can also by described as a plane wave and has the form:

$$\mathbf{Q}(\mathbf{r},\mathbf{t}) = \mathbf{Q}(\mathbf{q},\omega_\mathbf{0})\mathbf{cos}(\mathbf{q}\cdot\mathbf{r}-\omega_\mathbf{0}\mathbf{t}). \tag{2.7}$$

The variation of χ can be treated as a function of Q. As the displacement of the atoms due to phonons is significantly smaller than the lattice constant, χ can be expressed in a Taylor series in $\mathbf{Q}(\mathbf{r},\mathbf{t})$ (YC01):

$$\chi(\mathbf{k_i},\omega_\mathbf{i},\mathbf{Q}) = \chi_\mathbf{0}(\mathbf{k_i},\omega_\mathbf{i},) + \left(\frac{\delta\chi}{\delta\mathbf{Q}}\right)_\mathbf{0}\mathbf{Q}(\mathbf{r},\mathbf{t}) + \dots \tag{2.8}$$

The first summand: χ_0 is the electric susceptibility without atomic vibration. The second summand describes the influence of the distortion wave $\mathbf{Q}(\mathbf{r},\mathbf{t})$ on the susceptibility. With equation 2.8 the polarization 2.5 can be split into two parts:

$$\mathbf{P}(\mathbf{r},\mathbf{t},\mathbf{Q}) = \mathbf{P_0}(\mathbf{r},\mathbf{t}) + \mathbf{P_{ind}}(\mathbf{r},\mathbf{t},\mathbf{Q}). \tag{2.9}$$

P_0 describes a polarization wave, oscillating in phase with the incoming light wave:

$$\mathbf{P_0}(\mathbf{r},\mathbf{t}) = \epsilon_\mathbf{0}\chi_\mathbf{0}(\mathbf{k_i},\omega_\mathbf{i})\mathbf{F_i}(\mathbf{k_i},\omega_\mathbf{i})\mathbf{cos}(\mathbf{k_i}\cdot\mathbf{r}-\omega_\mathbf{i}\mathbf{t}) \tag{2.10}$$

The second summand of eq. 2.9, is the induced polarization contribution by the atomic vibrations of the lattice (e.g. phonons)

$$\mathbf{P_{ind}}(\mathbf{r},\mathbf{t},\mathbf{Q}) = \epsilon_\mathbf{0}\left(\frac{\delta\chi}{\delta\mathbf{Q}}\right)_\mathbf{0}\mathbf{Q}(\mathbf{r},\mathbf{t})\mathbf{F_i}(\mathbf{k_i},\omega_\mathbf{i})\mathbf{cos}(\mathbf{k_i}\cdot\mathbf{r}-\omega_\mathbf{i}\mathbf{t}) \tag{2.11}$$

To analyze the features of P_{ind}, it is converted to:

$$\begin{aligned}\mathbf{P_{ind}}(\mathbf{r},\mathbf{t},\mathbf{Q}) =& \epsilon_0\left(\frac{\delta\chi}{\delta\mathbf{Q}}\right)_0\mathbf{Q}(\mathbf{q},\omega_\mathbf{0})\mathbf{cos}(\mathbf{q}\cdot\mathbf{r}-\omega_\mathbf{0}\mathbf{t}) \\ &\times \mathbf{F_i}(\mathbf{k_i},\omega_\mathbf{i})\mathbf{cos}(\mathbf{k_i}\cdot\mathbf{r}-\omega_\mathbf{i}\mathbf{t}) \qquad (2.12)\\ =& \epsilon_0\frac{1}{2}\left(\frac{\delta\chi}{\delta\mathbf{Q}}\right)_0\mathbf{Q}(\mathbf{q},\omega_\mathbf{0})\mathbf{F_i}(\mathbf{k_i},\omega_\mathbf{i}\mathbf{t}) \\ &\times (cos[(\mathbf{k_i}+\mathbf{q})\cdot\mathbf{r}-(\omega_\mathbf{i}+\omega_\mathbf{0})\mathbf{t}] \\ &+ cos[(\mathbf{k_i}-\mathbf{q})\cdot\mathbf{r}-(\omega_\mathbf{i}-\omega_\mathbf{0})\mathbf{t}]) \qquad (2.13)\end{aligned}$$

The two contributions of P_{ind} represent the Stokes-frequency $\omega_S = \omega_i - \omega_0$ and the anti-Stokes frequency $\omega_{AS} = \omega_i + \omega_0$. They describe the process of the creation of a phonon (Stokes) and the annihilation of a phonon (anti-Stokes), as discussed above in the quantum-mechanical description of the scattering process. In Raman spectroscopy the Stokes process is mainly of interest, because normally the measurements take place at a low sample temperature to get the advantage of a narrow Raman linewidth. Low temperatures also mean that only a very small number of phonons are present in the sample and the anti-Stokes intensity is therefore vanishingly weak. Moreover, also for T = 300 K the thermal occupation of optical phonon modes is rather low. This is also the reason why Raman spectroscopy is referred to as an energy loss spectroscopy although it can in priciple also be an enery gain spectroscopy as the anti-Stokes signal contains the same degree of information.

2.3 Selection Rules

Throughout this thesis, Raman spectroscopy was performed in backscattering geometry on (100) surfaces of zincblende crystals, namely GaAs and ZnSe. In this subsection an excerpt of the selection rules for the tetrahedral crystal structure (e.g.T_d) is given. Scattering intensity is determined by

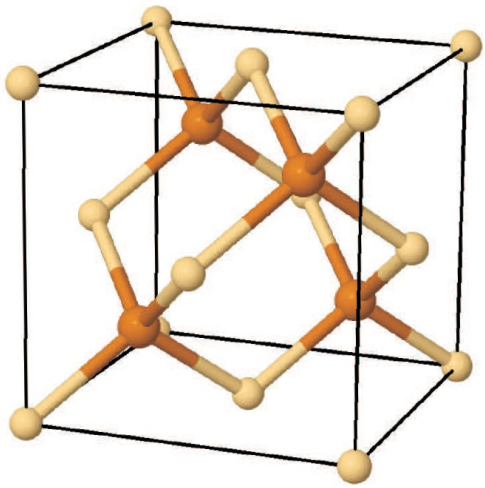

Figure 2.1: Cubic unit cell of the zincblende lattice, consisting of two fcc lattices, nested with tetrahedral bond symmetry, from (DDA08).

$$I_s \propto \left|\mathbf{e}_i \cdot \Re(j) \cdot \mathbf{e}_s\right|^2 . \tag{2.14}$$

With $\mathbf{e}_i, \mathbf{e}_s$ denoting the polarization vectors of incident and scattered photon and $\Re(j)$ being the Raman tensor with j=x,y,z representing the atomic displacement (elongation)

Surface	e_i	e_s	TO	LO
(100)	[010]	[001]	-	DP
	[010]	[010]	-	F
	[001]	[001]	-	F
	[011]	[011]	-	DP + F
	[011]	[01$\bar{1}$]	-	-

Table 2.1: Selection rules for optical phonons in backscattering geometry on the [100] surface

direction. The distinction between longitudinal (LO) and transversal (TO) phonon follows by additionally considering the propagation direction (k-vector) of the lattice vibration wave.

For a scattering experiment on the (100) surface of a zincblende crystal the Raman tensors, induced by the lattice deformations in the different directions, are:

$$\Re(x) = \begin{pmatrix} 0 & 0 & 0 \\ 0 & 0 & a \\ 0 & a & 0 \end{pmatrix}, \Re(y) = \begin{pmatrix} 0 & 0 & a \\ 0 & 0 & 0 \\ a & 0 & 0 \end{pmatrix}, \Re(z) = \begin{pmatrix} 0 & a & 0 \\ a & 0 & 0 \\ 0 & 0 & 0 \end{pmatrix}. \tag{2.15}$$

With the additional assumption of backscattering geometry, k_i and k_s have to be antiparallel, i.e. along the x- and the -x axis, respectively. Hence, because of the transversal character of the electromagnetic waves, only the yy, yz, zz components of $\Re$ are relevant for the scattering and thus only $\Re(x)$ has to be regarded. Finally the wavevector conservation only allows a momentum transfer in [100] direction. Therefore the Raman tensor $\Re(x)$ which allows the Raman scattering belongs to the LO phonon, and TO phonons are excluded in this scattering geometry.

2.4 Scattering Mechanisms

For undoped samples two scattering mechanisms, namely deformation-potential and Fröhlich scattering, can lead to a lattice vibration detectable by Raman spectroscopy.

Deformation-potential scattering

This scattering mechanism concerns polar and unpolar crystal lattices. As the bandgap energy depends on the lattice constant, it may be modulated by the phonon-induced modulation of the bond length or bond angle. Since the arrangment of the atoms in the lattice is deformed by the phonon, this scattering is known as deformation-potential (DP) scattering.

The exchange interaction of the DP can be described phenomenologically by the rela-

tion (YC01):

$$H_{DP} = D_{n,k}\frac{\Delta a}{a_0} \tag{2.16}$$

$D_{n,k}$ describes the optical phonon deformation potential for the electronic band states indexed by n and k. The distance of the two atoms of the primitive unit cell of the zincblende lattice is a_0 and its variation due to the phonon modulation is Δa. As seen from eq. 2.16 there is no dependence on the wavevector and thus the interaction is also valid in the short-range regime. The Raman tensors which were introduced above apply for this scattering mechanism.

Fröhlich scattering

While deformation potential scattering can happen in all semiconductors regardless of the bond type, in polar semiconductor an additional scattering mechanism exists, which is called Fröhlich scattering. An optical phonon with long wavelength can displace the anion/cation lattice atoms resulting in a macroscopic polarization and thus resulting in a macroscopic electric field E_{LO} (YC01). This electric field oscillates with the phonon frequency. The proportionality between the relative displacement of the positive and negative Ion Δa_{LO} and the generated field is given by the Fröhlich constant F

$$E_{LO} = -F\Delta a_{LO}. \tag{2.17}$$

The Fröhlich constant is defined by:

$$F = -\sqrt{4\pi N\mu\omega_{LO}^2(\frac{1}{\epsilon_\infty} - \frac{1}{\epsilon_S})}\frac{1}{\sqrt{4\pi\epsilon_0}} \tag{2.18}$$

The number of unit cells per unit volume is denoted by N and μ is the reduced mass of the primitive cell defined by

$$\mu^{-1} = M_1^{-1} + M_2^{-1}. \tag{2.19}$$

The mass of anion/cation are $M_{1,2}$. The longitudional electric field of eq. 2.17 can be described by a scalar potential ϕ_{LO}:

$$\phi_{LO} = (\frac{F}{iq})\Delta a_{LO} \tag{2.20}$$

The Fröhlich interaction describes the interplay of an electron and the macroscopic Coulomb potential ϕ_{LO}. The Hamiltonian of this interaction is given by:

$$H_{Fr} = (-e)\phi_{LO} = (\frac{ieF}{q})\Delta a_{LO} \tag{2.21}$$

According to (YC01) by the theory of H. Fröhlich (H.54) the Hamiltonian can be written as:

$$H_{Fr} = \sum_{\mathbf{q}} (iC_F/q) \left\{ c_q^+ exp[i(\mathbf{q} \cdot \mathbf{r} - \omega_{\mathbf{LO}}\mathbf{t}] - \mathbf{c.c.} \right\} \tag{2.22}$$

with the phonon creation operator c_q^+. The coefficient C_F comprises

$$C_F = e\sqrt{\frac{2\pi\hbar\omega_{LO}}{NV}\left(\frac{1}{\epsilon_\infty} - \frac{1}{\epsilon_S}\right)}\frac{1}{\sqrt{4\pi\epsilon_0}}. \tag{2.23}$$

Two properties of C_F should be mentioned: First, the Fröhlich interaction can be calculated by macroscopic parameters like ϵ_∞ and ϵ_S. Their difference is a direct measure of the bond polarity, whose value is considerable in many II-VI-compounds (LB99). Secondly the dependence of the Fröhlich coupling is inverse to the wavevector q. This has important influence on the interaction strength of short- and longwavelength phonons.

Chapter 3

Lattice dynamics and electronic properties

3.1 Mode behaviour of ternary compounds

One essential aspect within the Raman analysis of II-VI layers is interdiffusion-induced formation of ternary compounds during growth and their stoichiometry. This stoichiometry is reflected in the lattice dynamics. Therefore we start with a survey of the phonon mode behaviour of ternary compounds.

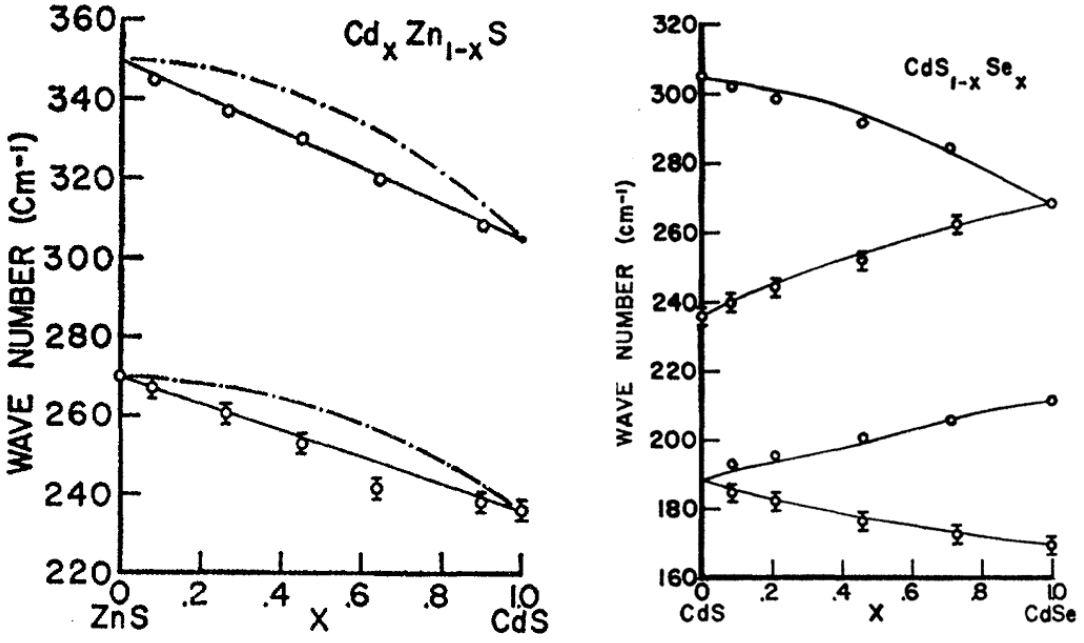

Figure 3.1: Phonon modes of ternary compounds: Single mode behaviour of $Cd_xZn_{1-x}S$ (left side) and the two mode behaviour of $CdSe_{1-x}S_x$ (right side), from (CM68).

The energy of a lattice vibration of a ternary compound depends on the mode characteristics. In principle it can be a single or two mode behaviour. As an example the mode

behaviour of two II-VI ternary compounds are shown in fig. 3.1. The left hand side shows the single mode behaviour with only one LO and TO frequency for each composition ratio of the components. The other possibility is the two mode behaviour with two LO and TO frequencies for each mixing ratio (right hand side). A systematic treatment of a wide variety of mixed compounds was performed within the Modified Random Element Isodisplacement (MREI) Model by Chang and Mitra (CM68). However, there is some controversy on the mode behaviour of the $Cd_{1-x}Zn_xSe$ system. According to Raman results from Alonso et al. (ASR$^+$89) and Gamacho et al.(CLC$^+$03), the $Cd_{1-x}Zn_xSe$ compound is not classified in the classical scheme of 1 or 2 mode behaviour, as it shows a mixed mode behaviour 3.2 with three possible lattice vibration energies. Other authors claim that it indeed exhibits single mode behaviour ((MHB$^+$96), (LSSF98), (LV04)). However, the main LO mode frequency, also in the mixed mode characteristics, is continuously redshifted from 256 cm^{-1} for ZnSe to 210 cm^{-1} for CdSe, so the main contribution to the Raman scattering intensity is definitely single mode like.

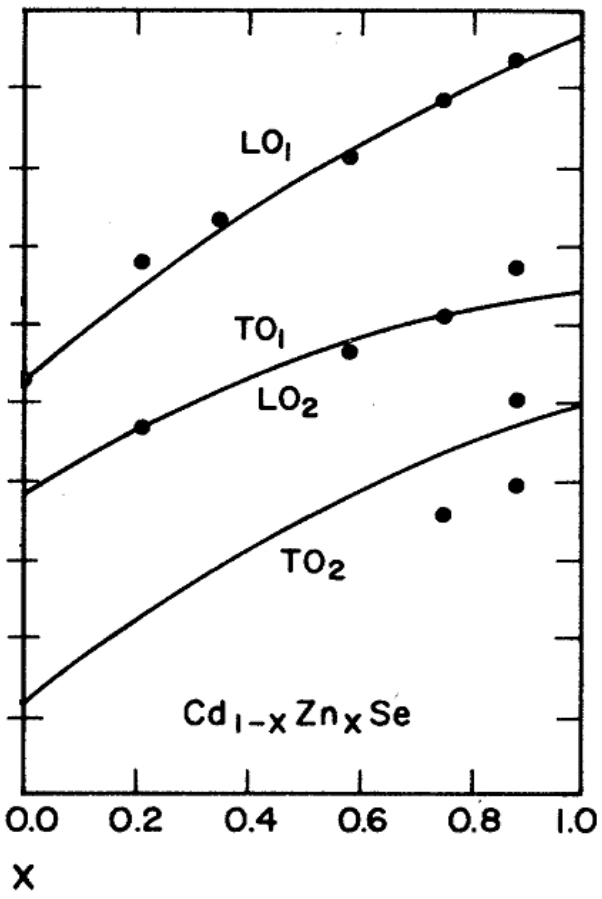

Figure 3.2: Composition dependence of the zone-center optical phonons for zincblende $Cd_{1-x}Zn_xSe$, from (ASR$^+$89)

Additionally, the ab-initio DFT calculations for biaxially strained pseudomorphic $Cd_{1-x}Zn_xSe$ on ZnSe which were performed for the investigations of this thesis within

a cooperation with Prof. Khellil Bouamama, yield single mode behaviour as shown in fig. 3.3. The splitting of the LO phonons here only results from the biaxial strain. The phonon energy values of in-plane and in growth direction are energetically shifted to each other due to the distortion of the elementary cell.

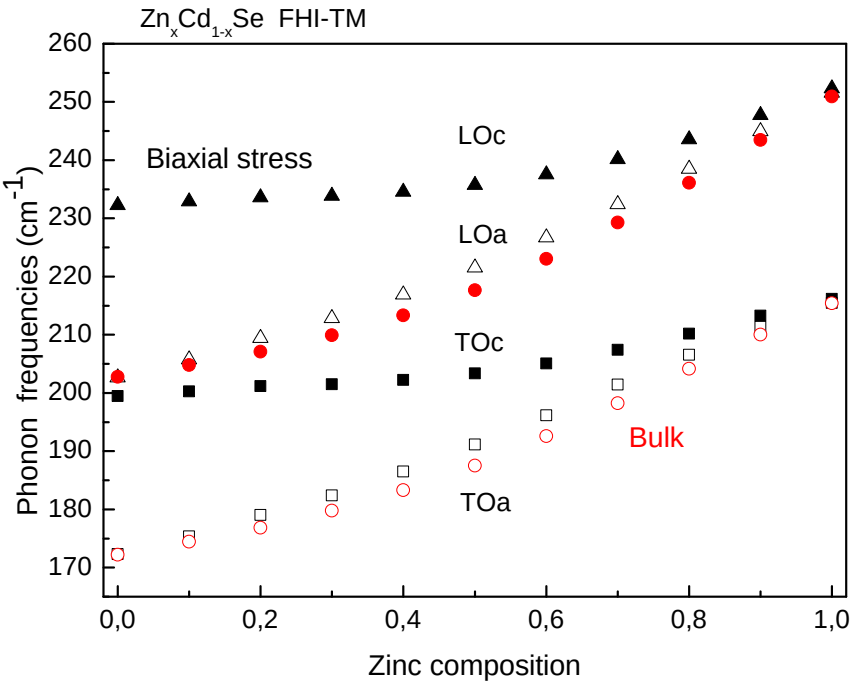

Figure 3.3: Ab-initio calculation by density functional theory of LO and TO phonon mode energies for a pseudomorphic ZnCdSe layer with the lateral latttice constant impressed by the GaAs substrate. LOa,TOa modes: atomic vibration in lateral direction (=in-plane movement). LOc,TOc modes: atomic vibration in growth direction (=perpendicular to interface).

In principle the diagram 3.2 is sufficient for a stoichiometric analysis by Raman spectroscopy. But this only fully applies for bulk materials and not for pseudomorphically grown strained epitaxial layers. In the samples which are investigated in this work the ZnSe and CdSe are compressively strained on the GaAs. This induces a partially compensating blueshift contribution in addition to the Cd-induced redshift of the LO phonon frequency. This compensating contribution increases with increasing Cd-content as the strain rises from 0.27 % (strain of the ZnSe on the GaAs substrate) to 7 % (lattice mismatch of CdSe with respect to the GaAs lattice constant). The actual dependency of the phonon frequency on the concentration of the $Cd_{1-x}Zn_xSe$ mixture will be deduced in the following for two different approaches as each bears some uncertainties. In the first approach, the frequencies are calculated, using the elastic constants and phonon deformation potential constants. The second approach utilizes the experimental determination of the phonon frequency from a calibration sample with a strained ZnCdSe layer of well-known composition.

3.2 Calculation of the strain induced phonon shift

When compressing a semiconductor the phonon frequency is increasing and vice versa. For pseudomorphically strained epitaxial layers, the elementary cell is laterally compressed to match the lattice constant of the substrate. This lateral compression induces an elongation of the elementary cell in growth direction (z-axis). Both values are connected by the material-specific Poisson number. For the LO phonon with elongation in growth direction, the altered phonon frequency $\omega_{LO,strain}$ due to the biaxial strain in pseudomorphic layers is according to (Her96) derived by:

$$\omega_{LO,strain} = \omega_0 + \frac{q\epsilon_{||}}{\omega_0} + \frac{p\epsilon_{||}S_{12}}{\omega_0(S_{11}+S_{12})}, \tag{3.1}$$

taking into account the bulk phonon frequency ω_0, the amount of strain $\epsilon_{||}$, the elastic compliances S_{12},S_{12} (for ZnSe: 23.9$\cdot$ 10^{-12}Pa^{-1} and -8.52$\cdot 10^{-12}$Pa^{-1} (OSPC87), for CdSe: 25.1$\cdot$ 10^{-12}Pa^{-1} and -9.51$\cdot 10^{-12}$Pa^{-1} (LB99) and the phonon deformation potentials p, q (for ZnSe: -0.97$\cdot\omega_0^2$ and -2.21$\cdot\omega_0^2$ (CG89). In the calculation the phonon deformation potentials p, q for CdSe which are undefined in literature were substituted by the values for ZnSe, because of the high similarity of these two compounds with adjacent constituents. This leads for fully strained CdSe on ZnSe to a phonon shift of +22.3 cm^{-1} with respect to the CdSe bulk LO phonon energy , for which values are reported between 208 and 211 cm^{-1} (LB99). The limitations of this approach and its linear extrapolation to the concentration variation of $Cd_{1-x}Zn_xSe$ are the following:
-The elastic constants of CdSe are only tabulated for the bulk wurtzite phase and not for the substrate-stabilized zincblende structure.
-Additionally the elastic constants are assumed to exhibit a linear dependency on the concentration.
-The lattice constant is assumed to be linear between the values for ZnSe and CdSe according to Vegards law (Veg21).
The most important fact is the applicability of the formula 3.1 when calculating the phonon shift of epilayers in case of the enormously high strain of around 7 %. Another aspect is the possible temperature dependency of the elastic constants and phonon deformation potentials when evaluating the low-temperature Raman spectra with the calculation which was performed for the lattice parameters at 300 K.

Frequency calibration by a ternary reference

In priciple the frequency calibration by ternary $Cd_{1-x}Zn_xSe$ reference samples with a known ratio of mixture seems like the most eligible way to derive the phonon energy dependence on the stoichometry. However this approach is hampered by the high lattice mismatch of Cd-rich $Cd_{1-x}Zn_xSe$ layers with respect to the GaAs lattice constant. The lattice mismatch of pure CdSe on GaAs amounts to 7 % and is the driving force for the QD formation 4 and thus it is not possible to fabricate homogeneous Cd-rich layers with a well-defined Cd-concentration. In contrast to Cd-rich samples it is indeed possible to grow homogeneous layers when the Cd-concentration is sufficiently low. Respecting this condition a 6 nm thick $Cd_{0.33}Zn_{0.67}Se$ layer sandwiched between 55 nm thick ZnSe layers was grown. The substrate was GaAs as for the other samples used within this thesis, thus ensuring the same lattice constant and mismatch. The Raman spectrum for 477 nm excitation wavelength and a sample temperature of 80 K is displayed in 3.4. The two prominent features are the scattering intensities of the LO phonon from the $Cd_{0.33}Zn_{0.67}Se$ and the LO phonon of the ZnSe. The small peak at 294 cm^{-1} is originating from the GaAs LO phonon of the substrate. The shift between pure ZnSe on GaAs and

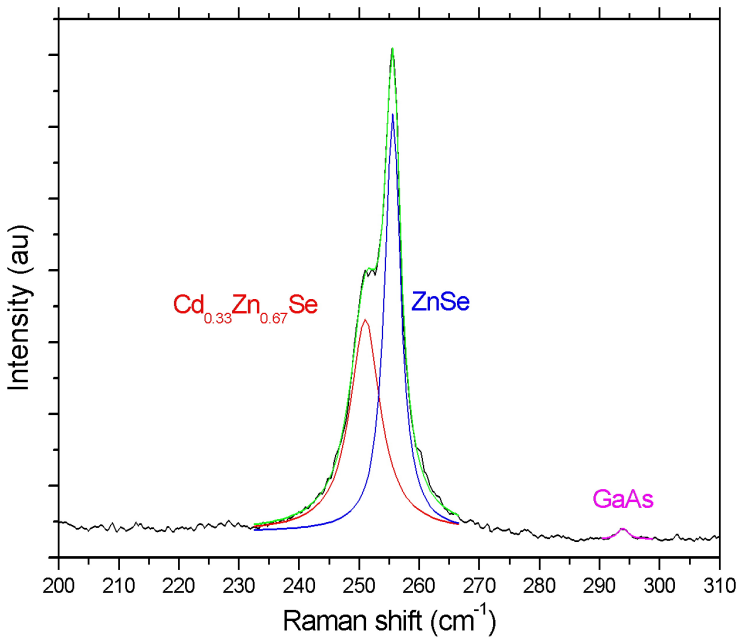

Figure 3.4: Raman spectrum of a pseudomorphic ternary $Cd_{0.33}Zn_{0.67}Se$ layer sandwiched between ZnSe layers on GaAs(001) substrate, excitation wavelength: 477nm, sample temperature: 80K.

the ternary $Cd_{0.33}Zn_{0.67}Se$ layer amounts to 5.9 cm^{-1}, i.e. a redshift of 0.197 cm^{-1} per percent Cd. Assuming a linear dependence, this extrapolates to a LO frequency of 239.8

cm^{-1} for pseudomorphic CdSe on a ZnSe layer with a biaxial strain of 0.27 %, i.e. with the lateral lattice constant of the GaAs substrate. The photoluminescence spectrum of this reference sample shows a very narrow halfwidth (FWHM<10meV @80K) of the exciton recombination in the $Cd_{0.33}Zn_{0.67}Se$ layer. This indicates a very good homogeneity of the layer concerning thickness and concentration. With this reference sample the phonon energies from scattering in the $Cd_{1-x}Zn_xSe$ layer and quantum dots of the sample series in this work can be linked with the actual Cd-concentration. As the sample layout is almost equal to the samples in the forthcoming measurements and the measurement temperature is identical, there are almost no uncertainties left, except the implementation of a linear extrapolation for the other Cd-concentration values.

3.3 Plasmon modes

The phonon modes of a crystal are strongly influenced by the presence of free carriers, this is due to the fact that the macroscopic E-fields of phonon and plasmon are coupling/interacting. The result are new elementary modes, the Plasmon-Longitudinal-Phonon (PLP) modes. Their origin is considered in the following.

PLP-Modes

Both PLP oscillations $\omega_\pm$ are longitudinal modes so their frequency position is determined by the roots of the dielectric function. The dielectric function is composed of the contributions from the valence electrons ϵ_∞, the phonons $\chi_{PH}(\omega)$ and the free carriers $\chi_{FC}(\omega, q)$.

$$\epsilon(\omega, q) = \epsilon_\infty + \epsilon_\infty \frac{\omega_{LO}^2 - \omega_{TO}^2}{\omega_{TO}^2 - \omega^2} - \frac{\omega_{PL}^2}{\omega^2 - \frac{3}{5} v_F^2 q^2} \tag{3.2}$$

v_F denotes the fermi velocity, q is the wave vector and ω_{PL} is the plasma frequency from eq. 3.8. In the equation above, no damping effects are considered.

The roots of the dielectric function are two frequencies, namely the $\Omega^\pm$ modes. For q=0, i.e. without considering dispersion effects, the roots are:

$$\Omega^\pm = \sqrt{\frac{1}{2}\left[(\omega_{PL}^2 + \omega_{LO}^2) \pm \sqrt{(\omega_{PL}^2 - \omega_{LO}^2)^2 + 4\omega_{PL}^2(\omega_{LO}^2 - \omega_{TO}^2)}\right]} \tag{3.3}$$

The dependence of the $\Omega^\pm$ modes on the doping level is shown in fig. 3.5. The graph was calculated for GaAs.

The q-dependent dispersion of the PLP modes in the near-center range of the Brillouin zone and the half width of the PLP peaks are different from those of the phonon excitations. In the relevant q-vector range for backscattering with visible light, i.e. below 1% of the Brillouin zone width, phonon excitations are almost independent of the wave vector transfer. However this approximation is not applicable to coupled Plasmon-phonon

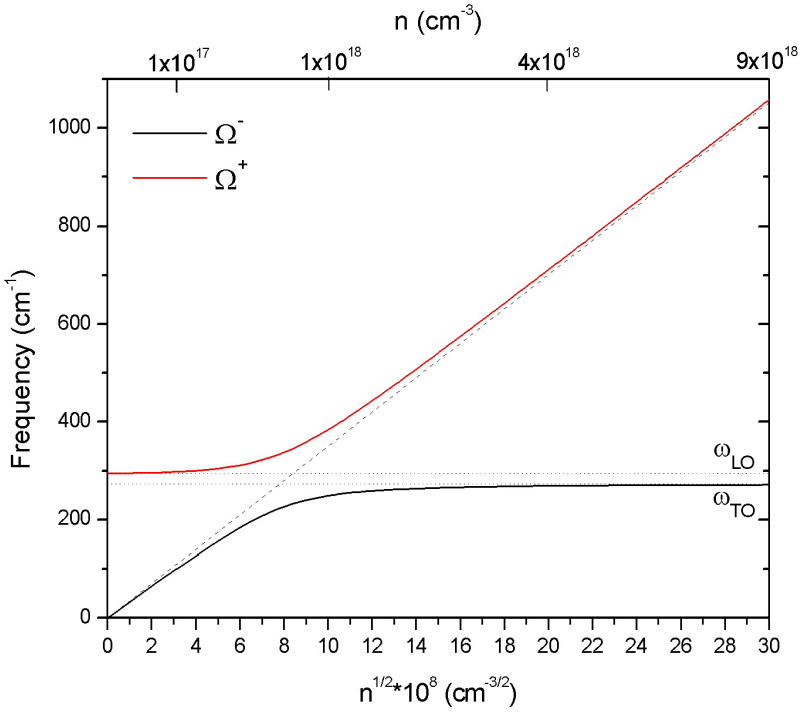

Figure 3.5: PLP-mode frequency dependence on doping level for GaAs. Dotted lines are the LO and TO phonon frequencies. The dashed line represents the plasma frequency.

excitation modes. Their plasmonic contribution induces a non-vanishing dispersion. This manifests itself as an increasing frequency due to the additional restoring force from the spatial charge density modulation which occurs at a finite wave vector of the collective charge density oscillation (ABV+07).

$$\Omega_p(n,q)^2 = \omega_p^2 + \frac{3}{5}v_{Fermi}^2 q^2 = \frac{ne^2}{m_{eff}\epsilon_0} + \frac{3}{5}v_{Fermi}^2 q^2 \tag{3.4}$$

$$v_{Fermi} = \hbar/m_{eff}(3\pi^2 n)^{1/3} \tag{3.5}$$

Furthermore, with increasing wave vector the PLP-modes approach the dispersion range of single particle excitations (SPE) in the conduction band. These constitute a decay channel for the collective oscillations. This results in a leveling-off of the PLP dispersion curves (NRS81). A detailed description of the frequency dependence on the wavevector can be found in (Bui10).

Another important property of the PLP modes are their half widths. Due to the amphoteric plasmon-phonon character of the PLP modes, the full width at half maximum (FWHM) of a PLP mode is governed by the phonon when this PLP mode is essentially phonon-like, i.e. its frequency is close to the LO phonon frequency. In contrast, for plasmon-like PLP modes, i.e. PLP frequencies far from the LO one, the FWHM value is

substantially enhanced due to charge carrier damping. As a consequence, for low doping levels a broad Ω^--mode and a narrow Ω^+-mode are observed, while the opposite behaviour applies for high doping levels.

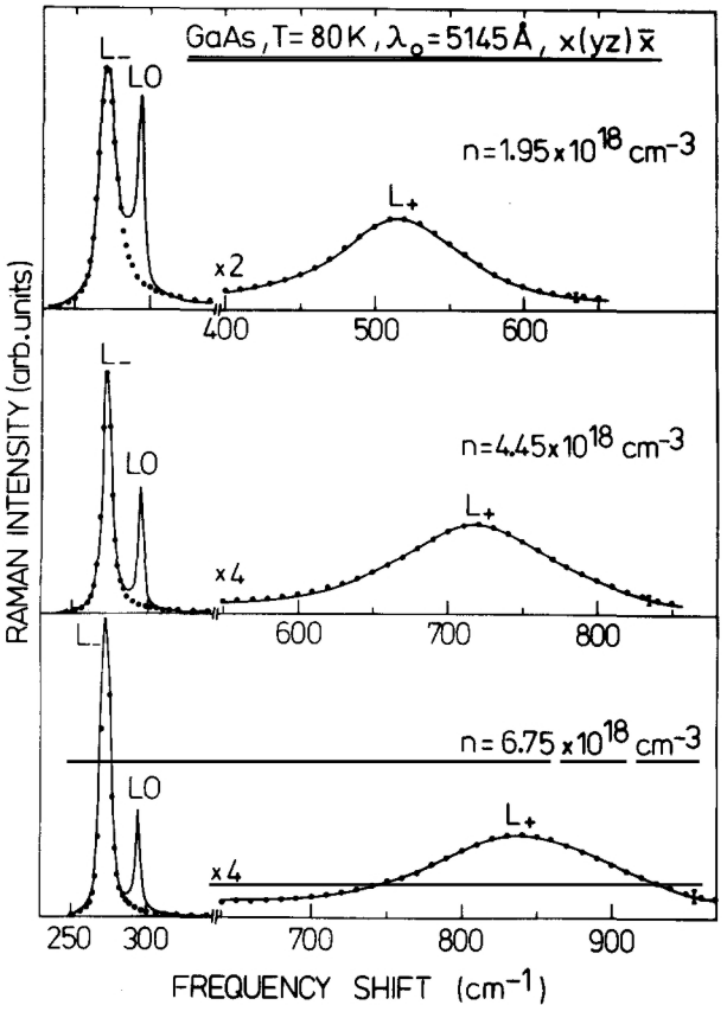

Figure 3.6: Experimental results of the PLP-mode frequency from GaAs for three different doping densities. Beside the PLP-modes, the spectra also show the LO phonon from the depletion layer (from (ATCP79)).

3.4 Plasmon-LO-Phonon coupling

Besides the elementary phonon excitation in a sample, as another elementary excitation the plasmon has to be considered for a complete description of the interaction with light in a doped sample. As the free charge carriers act collectivly they can be described macroscopically. The following description of the plasmon is closely oriented at (Kli07). In a sample with high free carrier density (above $10^{17}\mathrm{cm}^{-3}$ a collective oscillation of the free carriers can occur. The subsequent illustration is shown for electrons (holes can be

treated similar). If the electron gas is oscillating by a displacement Δx a net charge occurs at the sample surface:

$$\rho_s = ne\Delta x \tag{3.6}$$

Thus creating the electric field E_x

$$E_x = \frac{ne\Delta x}{\epsilon\epsilon_0} \tag{3.7}$$

This consideration is true for a macroscopic 3D-sample. This case normally occurs if the sample is not of a quantum well or wire design.

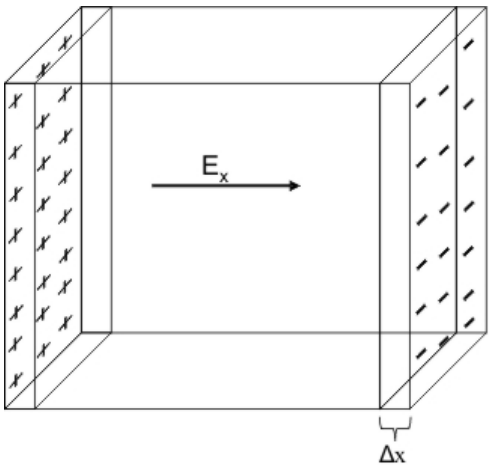

Figure 3.7: Schematic picture of the origin of the free-carrier plasmon eigenmode in a doped semiconductor.

The equation of motion of this plasma oscillation is given by

$$eE_x = \frac{ne^2\Delta x}{\epsilon\epsilon_0} = m_e\frac{\partial^2}{\partial t^2}(\Delta x) \tag{3.8}$$

The movement of the electrons can be described by a common harmonic oscillator, leading to the following dependence of the eigenfrequency on the carrier concentration n:

$$\omega_{PL}^0 = \sqrt{\frac{ne^2}{m_e\epsilon\epsilon_0}} = \omega_L, \quad \omega_T = 0 \tag{3.9}$$

Here the dielectric constant $\epsilon = \epsilon_s$ which is valid for $\omega_{PL} << \omega_{LO}$. For $\omega_{PL} >> \omega_{LO}$, the corresponding parameter is ϵ_∞. Additionally the transverse frequency $\omega_T = 0$, this is an obvious result as for gases there is no restoring force due to shear displacement.

The above consideration only deals with plasmons, but it is also possible that this oscillation is interacting with phonons which leads to a new excitation: the Plasmon-Longitudinal-Phonon (PLP) mode. The properties of the PLP excitation will be discussed in the next subsection.

3.5 Band bending at interfaces

As shown previously, doped semiconductors exhibit characteristic vibration spectra due to the plasmon oscillation. While this situation applies for the bulk, at interfaces (or surfaces) the free charge carrier density can be considerably different. Especially surfaces with their unsaturated bonds trap free charge carriers from the bulk, leaving the ionized donors behind. This charge accumulation at the interface is accompanied with a perpendicular electric field E_s repulsing the remaining free carriers in the bulk from the surface. The charge transfer can be described by the simple Schottky model. The volume density ρ_D in the depleted layer is constant and zero in the bulk. This step like behaviour is in most cases a good approximation, although in reality the step-like density of the free carriers is smeared out. This carrier free region is the depletion layer d_D. The depletion layer thickness can be calculated as follows. The absolute value of surface charge Q_S equals the charge in the depletion layer Q_D. So the charge density in the depletion layer is only governed by the ionized donors.

$$\rho_D = eN_D \tag{3.10}$$

For this situation Poisson´s equation is formulated as

$$\frac{d^2\Phi}{dz^2} = -\frac{\rho(z)}{\epsilon_s\epsilon_0} = -\frac{eN_D}{\epsilon_s\epsilon_0} \tag{3.11}$$

Twofold integration of eq. 3.11 with the boundary conditions $n = 0$ for $0 < z < d_D$ results in the electric field E_s and potential V_{bb} (Her96).

$$E_s(z) = (1 - \frac{z}{d_D})\sqrt{\frac{2eN_DV_{bb}}{\epsilon_s\epsilon_0}} \tag{3.12}$$

$$V_{bb}(z) = \frac{eN_D}{2\epsilon_s\epsilon_0}(d_D - z)^2 \tag{3.13}$$

The resulting depletion layer width d_D amounts to

$$d_D = \sqrt{\frac{2\epsilon_s\epsilon_0V_{bb}}{eN_D}}. \tag{3.14}$$

Fig. 3.8 shows the doping level dependence of the depletion width d_D in GaAs for mid-gap pinning of the Fermi level at the surface/interface, i.e. $V_{BB} = 0.7eV$. A roundup of the situation at the interface is shown in fig. 3.8. For an optical experiment this situation of a sample having a depleted region and bulk doping enables the analysis of phonons from the depleted region and PLP-vibrations from the bulk. It is obvious that in this case the scattering intensity of the depleted region is directly correlated with the depletion layer thickness d_D (providing that the penetration depth exceeds the depletion layer thickness, which is always fulfilled if the bulk PLP modes appear in the Raman spectrum.).

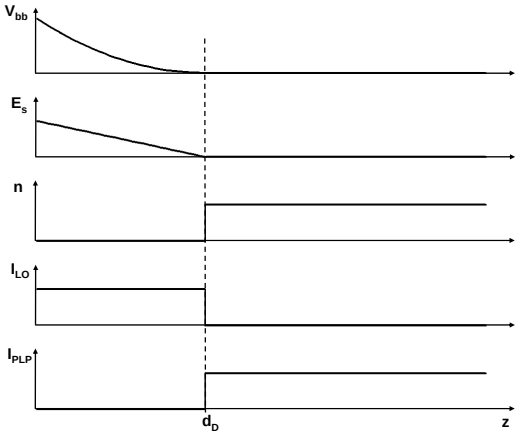

Figure 3.8: Schematic plot of the impact of surface band bending. The diagrams show the depth-dependence of band bending potential V_{BB} (parabolic decrease), electric surface field E_s (linear decrease), free carrier density n (step function), and Raman contributions I_{LO} from the LO phonon and I_{PLP} for the Plasmon-LO-Phononmode (complementary step functions).

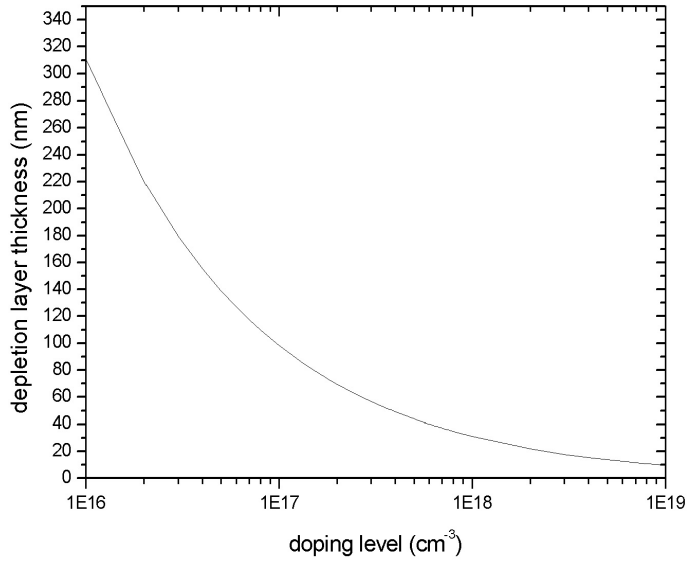

Figure 3.9: Depletion layer thickness of GaAs at mid-gap pinning as a function of the bulk free-carrier concentration.

Penetration Depth

For optical experiments on heterostructures, surfaces and interfaces the strength of the interaction of the incoming light with the materials in the different sample layers is crucial for the sensitivity and selectivity. The light-matter interaction strength strongly depends

on the material as well as on the incoming photon energy. This dependence originates from the fact that in the visible spectral range the interaction is governed by resonant excitation of electronic transitions between valence- and conduction band states, leading to strongly material- and energy-dependent transition probabilities. The resulting values of the light penetration depth range between $> 10\mu m$ for photon energies immediately above the fundamental band gap and a minimum value of about $10nm$ at higher energy gaps (E_1, E_2).

The penetration depth δ is defined as the length after which the intensity is decreased to $1/e$. It is directly connected with the imaginary part κ of the complex index of refraction $\tilde{n}$:

$$\delta = \frac{c}{\kappa\omega} = \frac{\lambda}{\kappa 2\pi} \tag{3.15}$$

For Raman spectroscopy where $\omega_i \approx \omega_s$ holds and additionally backscattering geometry is fulfilled, the information depth is half of the penetration depth. This has to kept in mind when choosing the appropriate excitation energy and interpreting the spectra. The frequency dependence of the light penetration depth for GaAs is shown in fig. 3.10.

The dependency of the penetration depth on the photon energy of GaAs is of particular importance for this thesis as ZnSe is transparent for the employed photon energies ($h\nu_{max} = 2.71eV$) at a sample temperature of around 80 K.

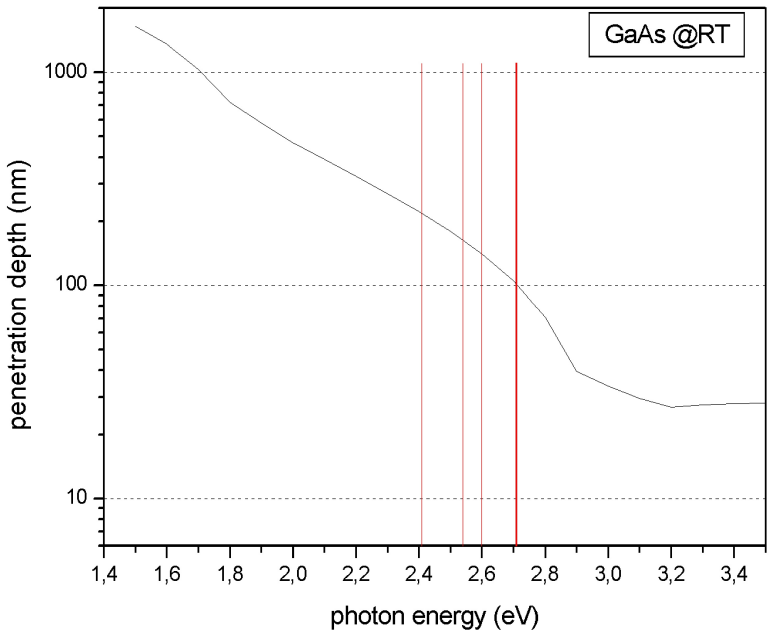

Figure 3.10: Light penetration depth of GaAs at RT (AS83). Vertical lines indicate the main visible Argon-ion laserlines

3.6 Photoluminescence Spectroscopy

In the framework of this thesis the most important information from photoluminescence measurements are the energies of the electronic transitions in the sample. The knowledge of these energy values is not only of interest with respect to the characterization of the different samples, but also constitutes a valuable support for achieving resonance conditions in the Raman experiment. To gain significant Raman scattering intensity from sample volumes in the monolayer range (e.g. quantum dots) the transition energies are vital for resonant excitation and thus choosing the appropriate excitation wavelength. For an undoped semiconductor with a direct bandgap the photoluminescence spectrum reflects the fundamental bandgap energy, or the corresponding exciton energy, respectively. The situation is different for a sample including quantum dots. The intuitive transition energy in a 3D confined space is the bulk transition energy of the QD material, enhanced by the confinement energy of the quantum dot levels. The energy level of an electron in a quantum dot is defined by

$$E_{lmn} = \frac{\hbar^2\pi^2}{2m_0}\left[\left(\frac{l}{L_1}\right)^2 + \left(\frac{m}{L_2}\right)^2 + \left(\frac{n}{L_3}\right)^2\right] \tag{3.16}$$

with l,m,n being the energy level indices in the confinement directions and L_1, L_2, L_3 confinement lengths. For realistic quantum dots, such as CdSe in ZnSe, the description of the transition energy is not that simple. The lattice constant of the dot material is dictated by the surrounding matrix lattice constant. This results in strain of the quantum dot and thus the bulk bandgap value of the dot material is changed. Additionally the quantum dot material is not necessarily pure. Especially in the CdSe/ZnSe system a significant intermixing occurs which also alters the bandgap. As seen from eq. 3.16 the energy levels of a dot strongly depend on its dimensions. The lateral dimensions for the quantum dots are in the range of 20 nm and the height is around 2 nm (derived by AFM-studies for an uncapped quantum dot layer with a nominal coverage of 3 ML and prepared by the in-situ annealing technique (Mah07)). Finally the dots are not uniform in size and show a large spreading. Because of this size spread and the high areal density of the dots ($10^{11}\mathrm{cm}^{-2}$), the PL measurement performed with a laser spot size in the range of some 100 μm diameter gives information about the averaged properties of the quantum dot ensemble. This explains the high width of the recorded spectral features.

Part II

Results and discussion

Chapter 4

Epitaxial CdSe/ZnSe quantum dots

4.1 Quantum dot introduction

In this chapter the stoichiometry of self-assembled CdSe quantum dots (QD) embedded in ZnSe is investigated with special reference to the impact of different growth methods. At the beginning a short outline of the measurement procedure, the fabrication process, and nomenclature for their description used within this work is given.

The analysis of the QD samples usually starts with a photoluminescence measurement followed by Raman spectroscopy. The photoluminescence spectra are employed to derive the energy level distribution of the QDs thus enabling the choice of the appropriate excitation energy for resonant Raman excitation. The PL halfwidth is basically an indication of the size and Cd concentration homogeneity of the QDs. As will be seen in following the inhomogeneous broadening effect due to the spatial variation of the Cd concentration by far exceeds the thermal broadening at the measurement temperature of 80 K. With the band gap information of the QDs derived by the PL measurements, the QDs are subsequently analyzed by resonant Raman spectroscopy (RRS). Although the Argon-ion Laser only has discrete excitation energies (i.e. laserlines) it is still possible to resonantly excite the QDs due to their broad band energy distribution and because the QD energies of the examined CdSe QDs are located in the region of the Argon-ion laserlines. Due to the macro-Raman setup and the high density of the QDs in the samples, the signal comprises the weighted sum of contributions of QDs, including possible slight variations of size and Cd-concentration. The weighting originates from the increased scattering efficiency of those dots for which the resonant excitation condition is most closely fulfilled.

The samples with the QD structures are prepared by the self-assembled growth of CdSe on ZnSe during the molecular beam epitaxy (MBE) fabrication process. Self-assembly in this context means that the QD structures are formed spontaneously during the epitaxial growth process. This is in contrast to lithographically defined dots or nano particles which also act as QDs.

One classic example of self-assembled growth of QDs is the InAs/GaAs system. When depositing InAs on GaAs the growth consists of two stages. Until a critical thickness of

1.5-1.8 ML is reached the InAs forms a flat layer on the GaAs (LPP94),(JKB$^+$00). After this wetting layer is completed, the additional InAs piles up in island shaped structures whose size increases with increasing amount of deposited InAs. These uniform islands are the QD structures as they confine excitons. This growth mode behaviour is called Stranski-Krastanow. The driving force for the self-assembly into islands is the partial strain relaxation in these islands albeit the accumulation of surface energy. On the sides of the islands the compressed InAs cubic cell can extend itself a bit to the outside and thus enhance to some degree its lattice constant, which was originally impressed by the GaAs substrate. In fig. 4.1 a TEM image of a cut trough an uncovered InAs island is shown. The enlargement of the lattice constant at the sidefaces is depicted by the slight fanning-out of the bowed vertical lines.

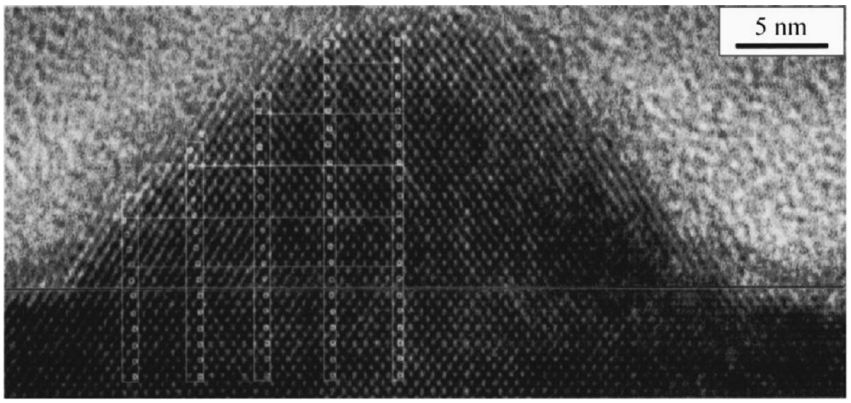

Figure 4.1: TEM image of an InAs island cross-cut, self-assembled of 2.25ML InAs deposited on GaAs(001). The vertical lines indicate the increasing lattice constant resulting from the elastic strain relaxation (CABA99).

In principle the same growth mode behaviour can be expected for the CdSe/ZnSe system. The lattice mismatch of InAs/GaAs of around 7 % (KML$^+$00) is very similar to the CdSe/ZnSe lattice mismatch. However, other material properties like ionicity or the vapor pressure differ significantly. The bond polarity α_p of II-VI materials ($\alpha_{p,ZnSe}$=0.75, $\alpha_{p,CdSe}$=0.79) is around twice the value of GaAs ($\alpha_{p,GaAs}$=0.47) (Har89). As this results in a decreased shear-stiffness, the II-VI compounds are more prone to reduce strain by formation of dislocations rather than by elastic deformation. The higher vapour pressure of the II-VI materials entails a significantly reduced growth temperature. This decreases the surface diffusion length of the adatoms and thus humbles the creation of flat surfaces (GM93). Still, in literature the growth mode of CdSe on ZnSe is often referred as Stranski-Krastanow (KJS$^+$10),(SDH$^+$00). This is due to the fact that at least for some growth procedures, in-situ RHEED experiments reveal a Stranski-Krastanow growth mode behaviour (PFG01). However, when dealing with samples for experimental application purposes the CdSe-layer is usually capped and for capped samples all TEM pictures reveal that the CdSe layer is of a varying thickness and Cd-concentration e.g. fig. 4.3.

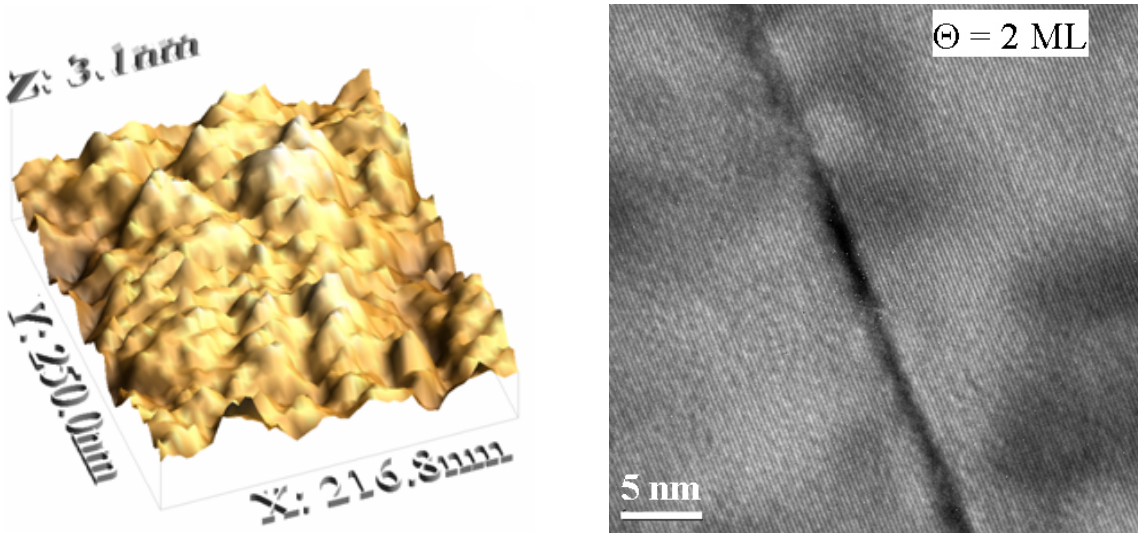

Figure 4.2: AFM image of 3 ML uncapped CdSe (left side) and a bright field HRTEM cross section of 2 ML CdSe (right side). Both samples were grown by the conventional MBE technique (Mah07).

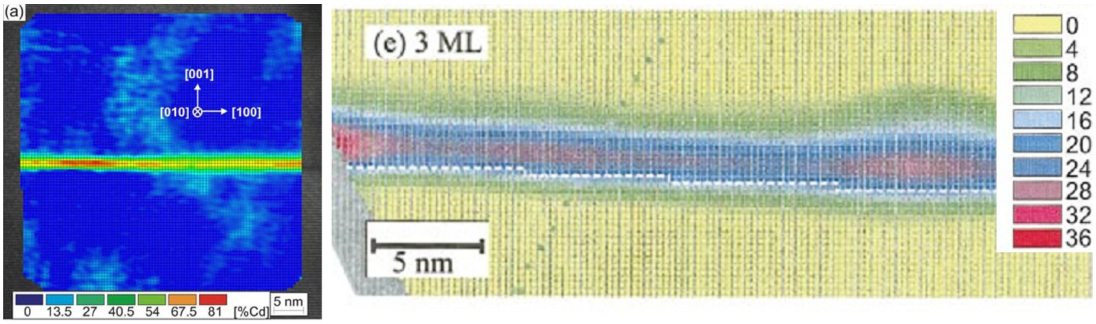

Figure 4.3: TEM cross-section images of 3ML CdSe embedded in ZnSe. The left hand side shows the Cd-concentration of a sample from (LSR$^+$08) while the right hand side is the result for a sample from (PRG$^+$00). The colour coding represents the Cd-content in the heterostructure, determined by high resolution lattice fringe images by the CELFA method. Noticeable are the high differences in the Cd-content of those two examples.

So the resulting layer after overgrowth with ZnSe is adequately described as consisting of a roughened ternary $Cd_xZn_{1-x}Se$ quantum well with thickness fluctuations and a locally varying Cd-content. Albeit not owning the nice shape of canonical SK-islands, the areas with a high Cd-content can still be called QDs as they for example bind excitons. Another criterion against canonical SK-QDs are the PL-peak energy positions vs. the nominal CdSe coverage. For QD structures resulting from pure SK growth, the position of the PL-energy should exhibit a distinct redshift for coverages above the wetting layer thickness. But for the CdSe QDs, the PL-energy is essentially only a monotonic progression with increasing CdSe-coverage (LSR$^+$08), (MYM$^+$00), (IOY$^+$08). Although the CdSe on ZnSe clearly does not grow in Stranski-Krastanow mode, the morphology does depend on the

applied growth procedure. The influence of the growth technique on the stoichometry of the $Cd_xZn_{1-x}Se$ layer will be addressed in this chapter.

Another aspect should be mentioned as it is sometimes overlooked. The structural arrangement of the CdSe layer before capping with the ZnSe is usually determined by atomic force microscopy (AFM). Hereby, the size (diameter and height) and the density of the QD formation are measured. In this way the effect of different growth procedures on the morphology can be compared. However, AFM can only detect the structural properties and is not element specific. So there is no information on the surface composition. Another fact which has to be kept in mind is that the surface morphology and/or composition is altered during the capping with the ZnSe. Transmission electron microscopy (TEM) pictures of the capped samples always reveal that there is a significant intermixing of Cd with the ZnSe-matrix. As this happens during the capping process of the QD structures, the morphology and composition of the CdSe QDs are also changed.

In the following the nomenclature for describing the CdSe layer is:

- QDs are a synonym for Cd rich areas of the nominal CdSe layer, which actually also contains intermixed Zn.
- Wetting layer is used to describe the rest of the nominal CdSe layer.

4.2 QDs from conventional growth

The conventional MBE growth process for CdSe Qds basically consists of quite elementary fabrication steps. Before the growth of the II-VI material, the commercial GaAs substrate is thermally deoxidized and is overgrown with a GaAs buffer layer (thickness around 200 nm). This is an essential requirement for a good crystalline growth start of the subsequent layers. This buffer is then overgrown with a ZnSe layer (around 40-50 nm) at a substrate temperature of 300 °C. The substrate temperature remains constant during the subsequent steps. Without growth interruption a CdSe layer with the desired nominal thickness (1-4 ML) is grown atop the ZnSe. Due to the lattice mismatch this CdSe layer forms the CdSe QDs. The growth rate in this case is in the order of 0.06 ML/s. The QD layer is finally covered with the ZnSe cap layer also around 40-50 nm thickness.

4.2.1 PL-Measurements

A conventionally grown QD sample series was first characterized by 300 K PL spectroscopy, fig. 4.4. The excitation energy in this case was 2.71 eV. All samples show a PL-signal originating from the CdSe layer (i.e. QDs) already at 300 K. This is an important fact for a possible commercial application. The PL intensity rises with increasing nominal thickness up to 3 ML. For higher coverages the PL intensity is decreasing due to the onset of dislocations which are non-radiative decay channels for the excitons. This generation of defects drastically reduces the PL intensity, because it preferentially affects the biggest QDs, i.e. those dots which are most essential for the exciton recombination,

because they are sinks for the excitons in their vicinity due to their reduced bandgap values. For lower coverages than 3ML the PL intensity is also decreasing, to a point where the PL and the Raman intensity are more or less equal, i.e. the 1 ML sample. The 1 ML sample shows a double peak structure. The additional peak originates from Raman scattering, whose resonantly enhanced intensity is comparable with the PL peak. So the observed spectrum is a superposition of both contributions. Thus the PL information of the 1ML sample was not evaluated by fitting a Gaussian shape on the intensity profile as it was done for the other CdSe coverages. The dependency of the peak position vs. the nominal coverage is comprised in fig. 4.5. It shows a nice linear descent with increasing nominal CdSe thickness which is explained by the reduction of the confinement-induced blueshift with increasing dot size, and possibly at the same time redshift of the gap energy due to increasing Cd content.

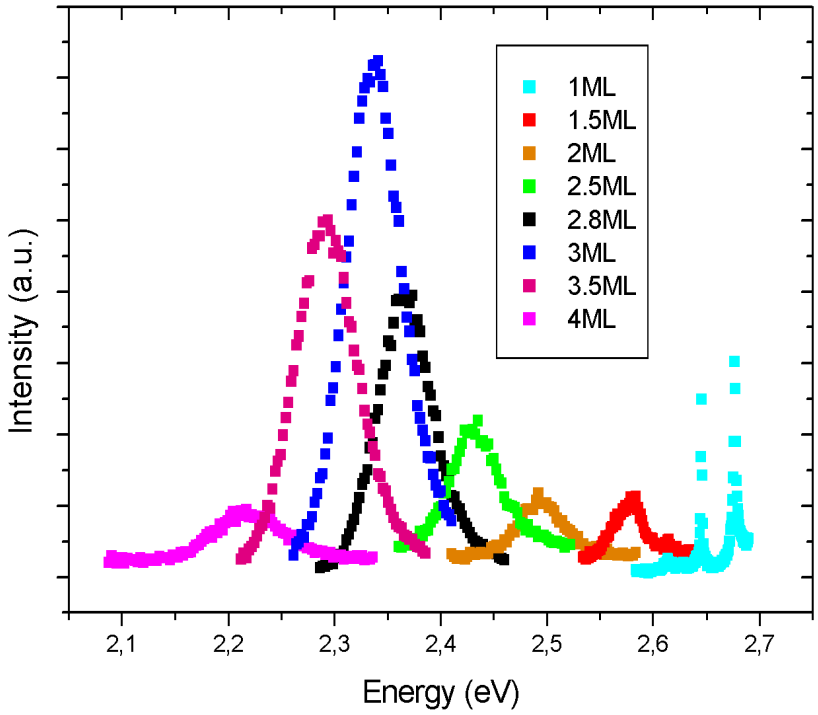

Figure 4.4: 300K photoluminescence spectra of conventionally grown CdSe QDs on ZnSe with different nominal thickness of the deposited CdSe.

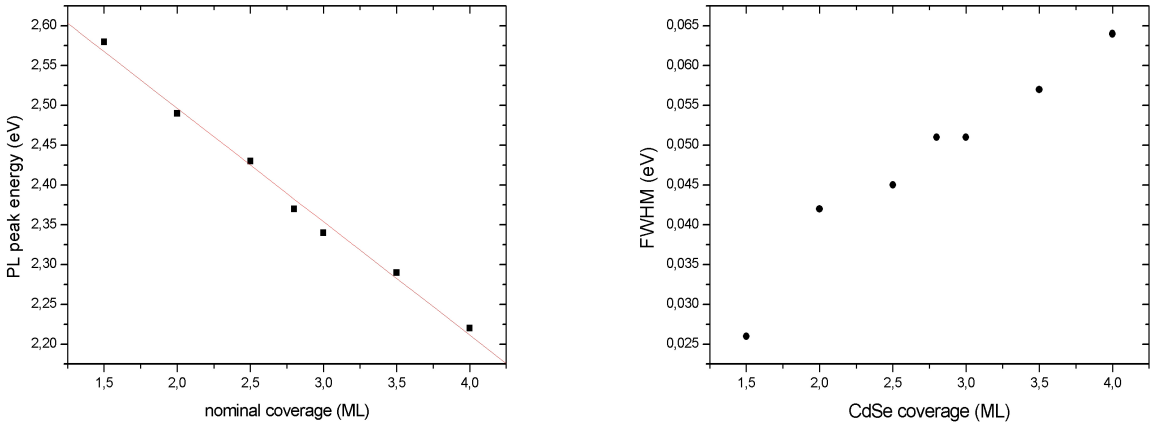

Figure 4.5: 300K PL peak energy position and corresponding FWHM of conventionally grown CdSe QDs on ZnSe with different nominal thickness of the deposited CdSe

For 80 K measurements the PL peak positions are shifted as expected to higher energies fig. 4.2.1. Here the peak intensities of the sample series are normalized to each other as the evaluation does not focus on the maximum luminescence efficiency but rather on the position and halfwidths. The energy position is correlated with the size and Cd-content of the QDs 4.2.1 and the halfwidth is an indication of their homogeneity 4.2.1. The morphological and stoichiometric fluctuations make up the high FWHM values of the sample series which by far exceeds the thermal broadening effect at 80 K. For comparison the PL of the ternary $Cd_{0.33}Zn_{0.67}Se$ reference sample was recorded at the same sample temperature and excitation energy 4.8. The halfwidth of this ternary layer only amounts to less than 7 meV which is a factor of three smaller than the narrowest halfwidth of the QD sample series.

Apart from the high values of the halfwidth of the QD samples, the FWHM derived for both measuring temperatures shows a linear increase with higher nominal CdSe coverages. Only the FWHM of the sample with 2 ML CdSe thickness does not follow this linear trend. This could be interpreted as the starting point for QD formation as low CdSe coverages are consumed in the wetting layer construction and thereafter the additional CdSe material could be arranged in the self-assembled QDs. However, this assumption is not backed by the PL peak position vs. the nominal CdSe coverage and it leads to the conclusion that the high FWHM values indicate an inhomogeneous CdSe layer and the growth process is not of the Stranski-Krastanow type. To which extent the CdSe layer is additionally a ternary compound will be analyzed by Raman spectroscopy in the following section.

4.2.2 Raman results

After the evaluation of the gap energy distribution of the QDs by the PL characterization the Raman spectra were recorded in order to assess the Cd concentration of the QDs. The

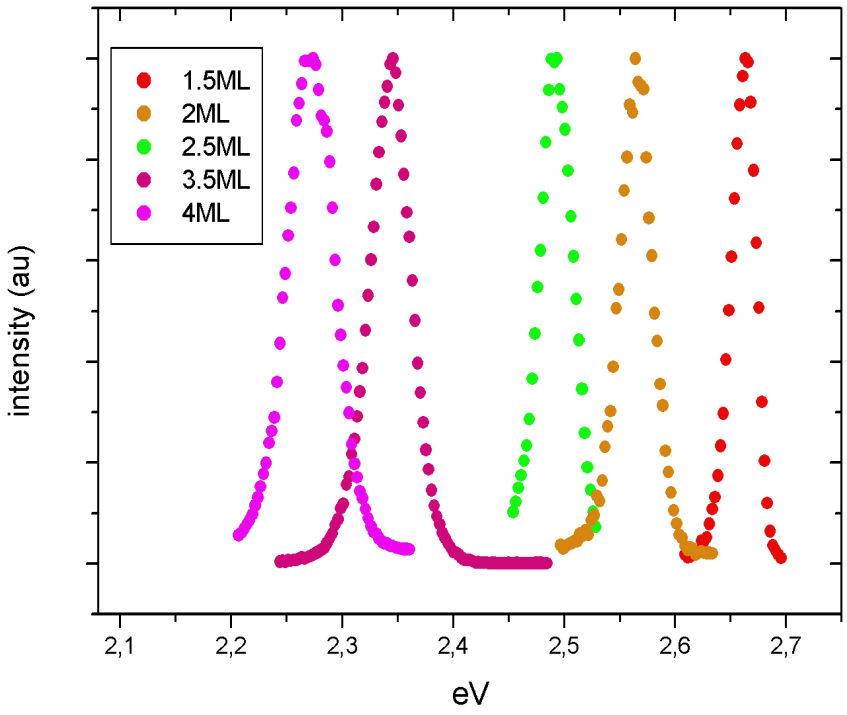

Figure 4.6: 80 K PL spectra of conventionally grown QDs with different nominal thickness, normalized to the same peak intensity.

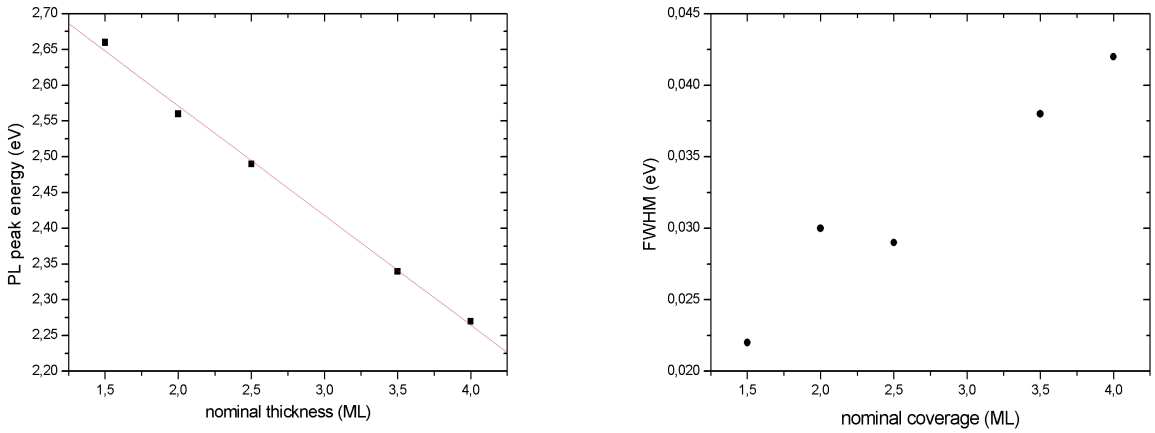

Figure 4.7: 80 K PL peak energy position and corresponding FWHM of conventionally grown CdSe QDs on ZnSe with different nominal thickness of the deposited CdSe

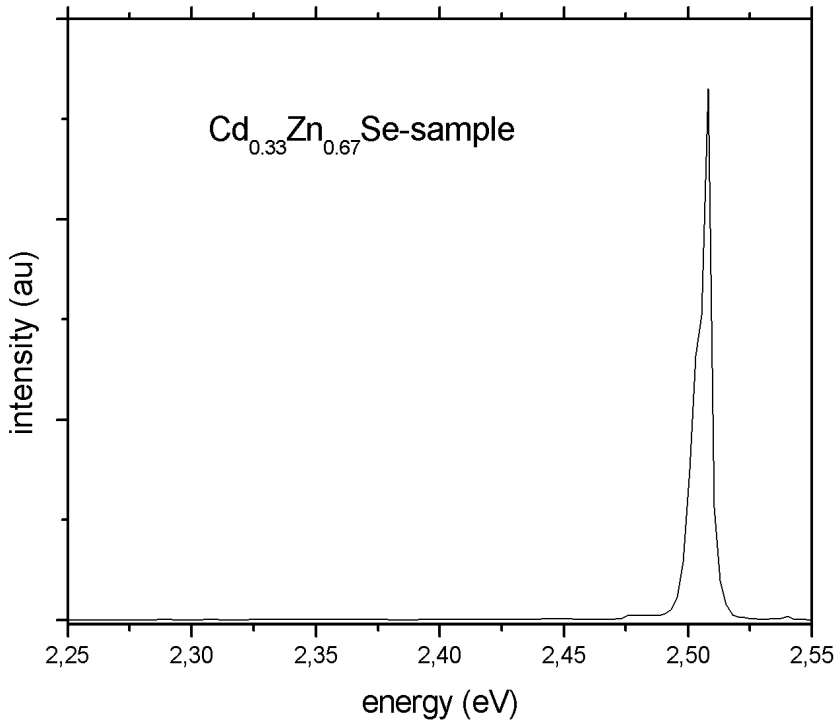

Figure 4.8: 80 K PL spectrum of the ternary $Cd_{0.33}Zn_{0.67}Se$ calibration sample.

spectra were all collected in backscattering geometry from the (001)-surface, thus allowing Raman scattering from LO phonons, while for ideal backscattering geometry contributions from TO phonons are excluded due to symmetry selection rules. The incident polarization was along the [110]-axis of the samples and no polarization analyzer was applied. For this polarization setup the LO phonon may appear from deformation-potential as well as from the Fröhlich scattering mechanism, because both are allowed in the $001(110, 110)00\bar{1}$ configuration (Porto notation) (CG82). The excitation wavelength was varied stepwise from 514 nm (2.41 eV) to 457 nm (2.71 eV). The sample temperature was kept at around 80 K. As an example, all spectra from the 4 ML and 2 ML samples are shown in fig. 4.9 and fig. 4.10.

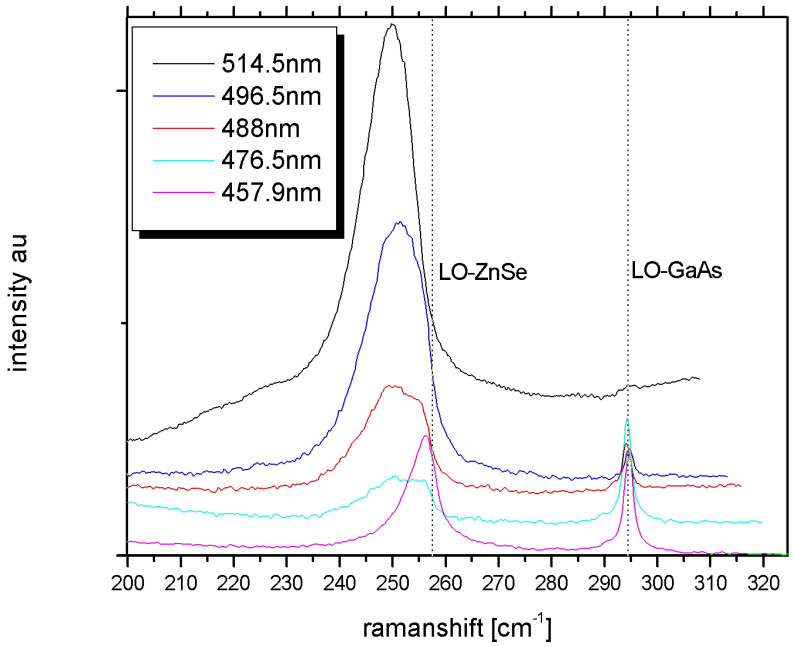

Figure 4.9: Raman spectra of a 4 ML CdSe / ZnSe-sample for different excitation wavelengths.

The resonant excitation condition is best explained for the 4 ML sample. For the highest excitation energy of 2.71 eV the spectrum consists of the GaAs LO phonon and the asymmetric and slightly shifted ZnSe LO phonon signal. The asymmetry most likely originates from areas of the sample in which a low Cd content is intermixed into the ZnSe e.g. the shell of the QDs. A low concentration of Cd results in a decreased bandgap of the ternary ZnCdSe. As the photon energy of 2.71 eV is only slightly below the fundamental bandgap of 2.8 eV of ZnSe (@ 80 K) these regions get resonantly excited and they contribute disproportionally to the spectra. With longer wavelength excitation the ZnSe intensity vanishes whereas the QD vibration signal is increasingly dominating the spectra. In the case of the 514 nm wavelength (2.41 eV) excitation the spectrum basically only shows the QD vibration and the GaAs signal virtually vanishes with respect to the

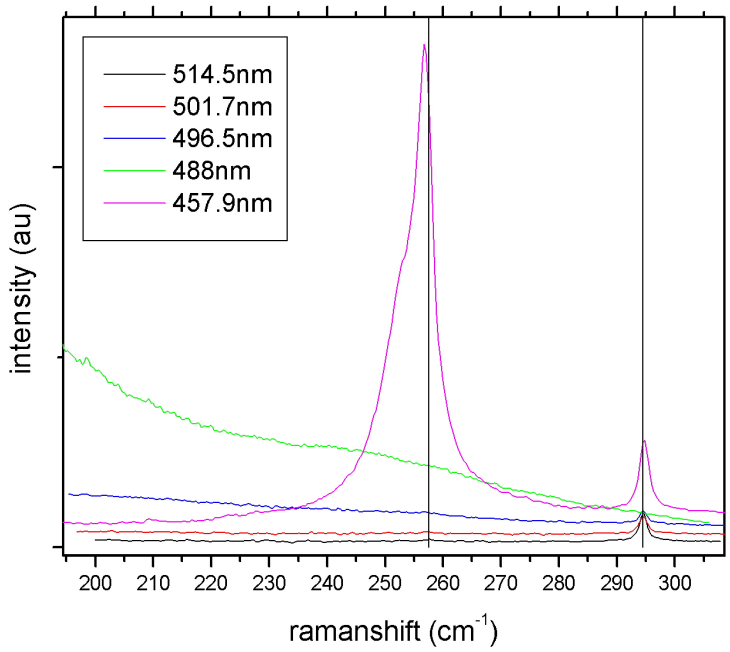

Figure 4.10: Raman spectra of a 2 ML CdSe / ZnSe-sample for different excitation wavelengths.

QD intensity, although the Raman scattering of the QDs is only from a layer with a nominal thickness of 4 ML. This is a consequence of the resonant excitation of the QDs as the excitation energy of 2.41 eV is only slightly above the mean band gap energy of the QDs of 2.27 eV.

Whereas the Raman scattering for the 2 ML sample shows distinct differences. For high energy excitation the spectra comprise the vibrations of GaAs, ZnSe, and the CdSe QDs. The spectrum for 477 nm excitation wavelength is totally dominated by the PL signal and is not shown. For 488 nm excitation the spectrum lacks the phonon signal of the QDs and the ZnSe as this photon energy of 2.54 eV is already below the bandgap of ZnSe (2.81 eV) and the QDs (2.56 eV) and therefore it is a non resonant condition for both. Only the GaAs signal is visible as for the other excitation wavelengths.

Already from the both excerpts shown in detail it is clear that there is no ZnSe-CdSe interface phonon present, although this could be expected (Her96). If this interface vibration existed there should be a phonon observable which is fixed in energy and occurring in all samples regardless of the nominal CdSe coverage. The dependence of the lattice vibration frequency of the QDs on the nominal CdSe coverage is illustrated in fig. 4.11. Even for the highest coverage of 4 ML there is no signal saturation which is a clear indication that the Cd concentration and/or the QD size are increasing. The maximum Cd-concentration reached in the 4 ML sample however is only around 50 % Cd. This value seems to be very low but there is no plausible explanation for a higher Cd-content without including unlikely scenarios, e.g. assuming a locally increased lattice mismatch

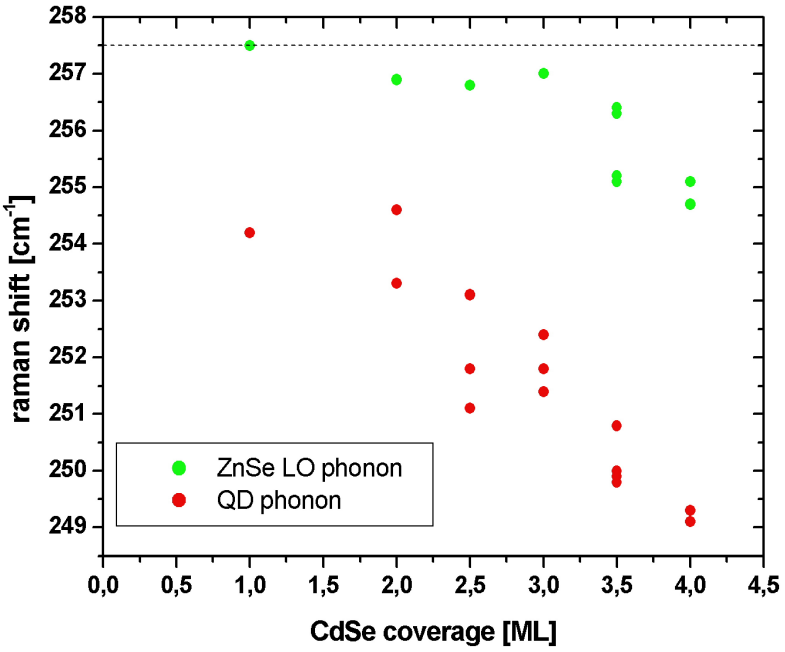

Figure 4.11: Dependence of the QD- and ZnSe-LO phonon frequency on the nominal CdSe coverage.

(beyond 7 %) as this is the only way to shift the LO frequency from a ternary layer with a Cd-content in excess of 50% to the vibration frequency measured in the experiments. If this scenario would apply, it would also be observed in the X-ray diffraction patterns of the samples as it would also contradict the finding that the samples are all pseudomorphic.

4.3 QDs from in-situ annealing

The basic idea for this growth process is given by Rabe et al (RLH98). Albeit there is one difference in the sample design. Their approach is to grow the CdSe layer on top of a thick and thus relaxed ZnSe buffer whereas here the ZnSe layer is pseudomorphically grown on the GaAs substrate.

The growth process itself consists of growing the ZnSe buffer at 280°C and cooling it down to 230°C under Zn flux. Subsequently the CdSe layer with the desired thickness is deposited. The growth of the CdSe is stopped by only closing the Cd cell shutter but leaving the Se cell open and thus keeping the sample in a Se-flux. The temperature is then increased to the annealing temperature of 310°C and is kept constant for an annealing time of 20 minutes. Subsequently the substrate temperature is decreased to 280°C and the final ZnSe cap (≈50 nm) is grown.

4.3.1 PL-Measurements

In spite of the modified growth procedure for this sample series the PL spectra are essentially similar to the ones gained from the conventional fabrication method showing the same trend. However there is one obvious difference. The PL energy values are throughout the sample series higher than those derived from the conventionally grown samples. For the nominal CdSe coverage value of 4 ML, the PL blueshift of the in-situ annealed QD with respect to those from conventional growth amounts to ≈ 60 meV. This is astonishing as it was expected that with the in-situ annealing the QDs should become larger and thus exhibiting a lower PL energy. The FWHM value for the 3ML sample matches the FWHM from the conventional QDs but the FWHM of the 4ML coverage is significantly higher meaning that there is a broader CdSe QD variation in size and/or composition. More importantly if there were large QDs in the CdSe layer then they should be a sink for the excitons in the proximity and thus should contribute disproportionally high to the PL signal resulting in a redshift. This redshift is not measured, so there are two explanations left: 1. there are no large QDs in the CdSe layer or 2. the large QDs already have stacking faults incorporated and thus the energy transition from the excitons in these QDs are non-radiative. A possible insight into this hypothesis can be gained with the Raman results as the phonon signal is more resistant against crystalline defects.

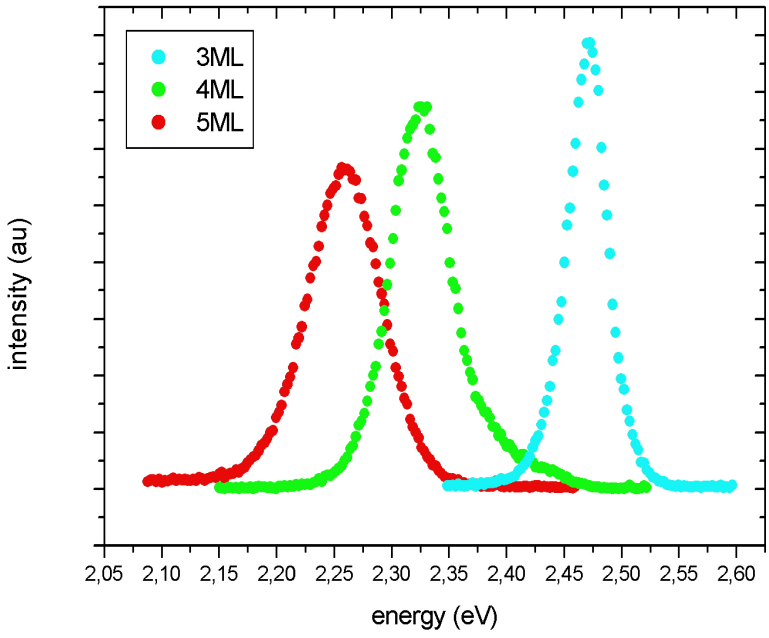

Figure 4.12: Photoluminescence of in-situ annealed QDs for different nominal CdSe coverage, recorded at 80 K.

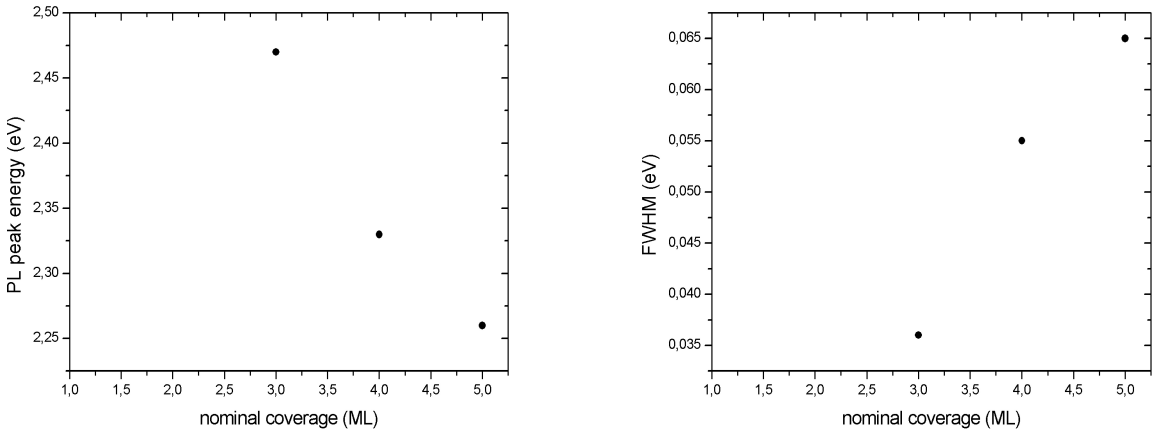

Figure 4.13: 80 K photoluminescence of in-situ annealed QDs: peak energy and corresponding FWHM dependence on the nominal CdSe coverage.

4.3.2 Raman results

In the paper by Rabe et al (RLH98) giving the idea for this growth procedure, the authors found three Raman phonons leading to the phonon replica in their PLE studies. The high energy phonon (31.8 meV = 256.5 cm^{-1}) can be unambiguously identified as the ZnSe LO vibration. The other two sample dependent modes have an energy of 26 meV (209.7 cm^{-1}) and 23.3 meV (188.0 cm^{-1}). It is appealing to assign the first value to the CdSe LO phonon, which amounts to 209 cm^{-1} at 300 K (LB99). However, this is only true at the first glance. In their sample the CdSe should not be completely relaxed and it is doubtful that the CdSe QDs consist of pure CdSe so the vibration energy should be much higher. Another fact but with minor impact on the phonon energy is the measurement temperature which is in their case 5 K, whereas the literature value applies for 300 K. The third vibration energy they detected was 188.0 cm^{-1}. This value can not be explained in terms of a TO vibration from the CdSe (literature value: 169 cm^{-1} (LB99)) nor can it be a combination of the other two values (ZnSe LO phonon and the phonon at 209 cm^{-1}). This means that the phonon signature of their measurements is not really understood and it is very interesting to see if in our samples series similar phonons are detectable.

The vibration signature of this sample series clearly shows that there is no phonon signal of 209 cm^{-1} visible for the 2-5 ML CdSe coverage. This is in contrast to the results from Rabe et al. This is a bit puzzling as the major difference to their sample series lies in the lattice mismatch difference for the CdSe layer of around 0.27%, resulting from the discrepancy between pseudomorphic and relaxed ZnSe. Another important aspect is the position of the QD vibration signal in comparison to the conventionally grown samples fig. 4.15. The two sample series are alike for coverages up to 3 ML. Beyond this thickness the trend diverges to a degree where the average QD phonon energy for the 5 ML sample is still higher than for the 4 ML sample grown by the conventional process. This means

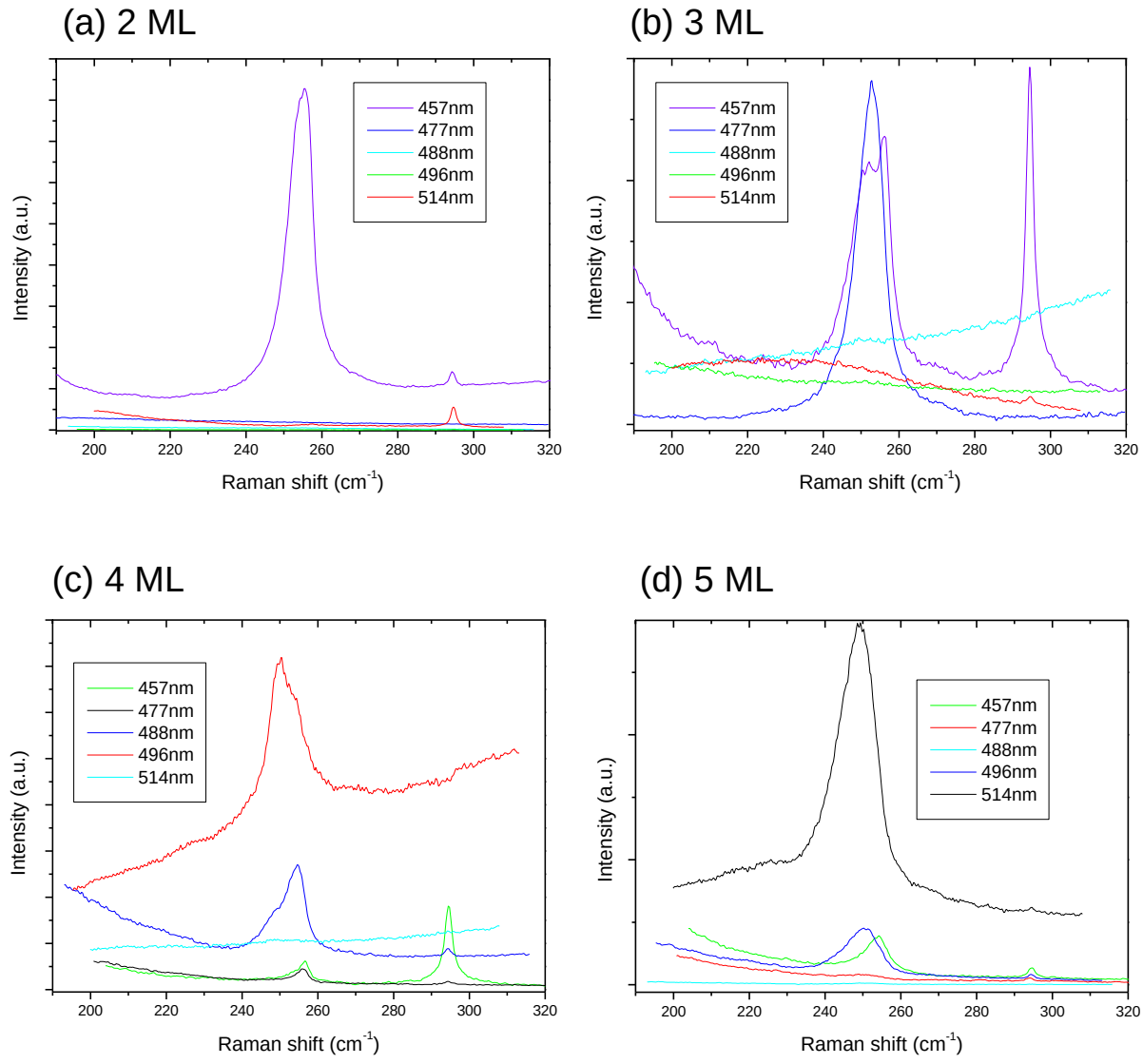

Figure 4.14: 80 K Raman spectra of the QD sample series prepared by in-situ annealing.

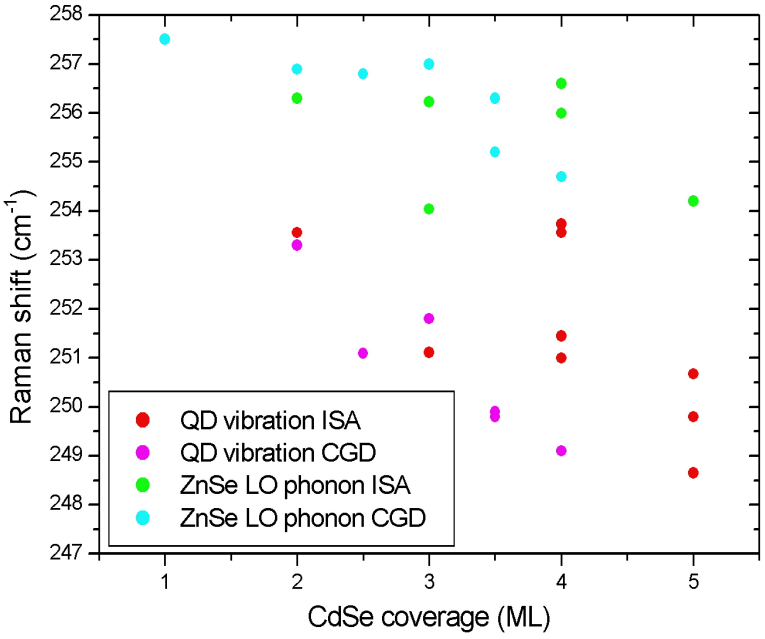

Figure 4.15: Phonon frequency dependence on the nominal CdSe coverage for the in-situ annealed samples series (ISA) and for the conventionally grown Dots (CGD)

that the Cd concentration of the QD for the high coverages is significantly lower and/or partial strain relaxation has occurred.

4.4 QDs formed by a-Se assisted growth

Following an idea of (RAB+06), the growth procedure of these QDs involves the following steps. The CdSe layer is grown at a substrate temperature of 230°C. Subsequently, the sample is cooled down to approx. 50°C (in 45-50min). In the following step, a 45nm thick amorphous Se-cap layer is grown. During the subsequent temperature ramp up to 280°C for the ZnSe overgrowth, the Se is desorbed while the QD structures are formed. For samples without the ZnSe cap, the AFM analysis reveals large and isolated QDs which however show a significant size spreading (heights vary from 4 to 15nm) (MKA+07).

4.4.1 PL-Measurements

The PL spectra were recorded at a sample temperature of around 80 K and the excitation energy was 2.71 eV (457 nm). The sample series shows a nice linear correlation between the nominal CdSe coverage and the corresponding PL peak energy. The FWHM reveals a monotonic increase with rising CdSe coverage, the only exception is the value for the 2 ML sample. One possible explanation could be a broader size and/or Cd-concentration distribution than for 3ML sample. This broadening has to be symmetric to the high and the low energy side as the PL peak energy of the 2 ML sample fits nicely in the linear trend. For the 3 ML sample the decreased FWHM denotes a better homogeneity.

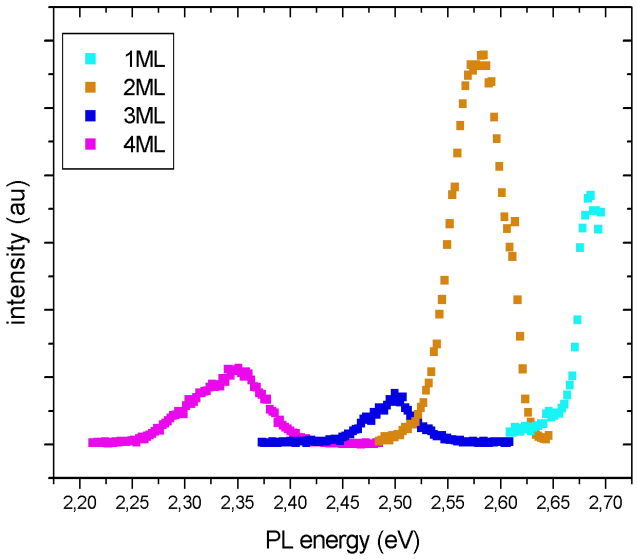

Figure 4.16: PL spectra of samples with different CdSe coverages prepared by the amorphous Se method.

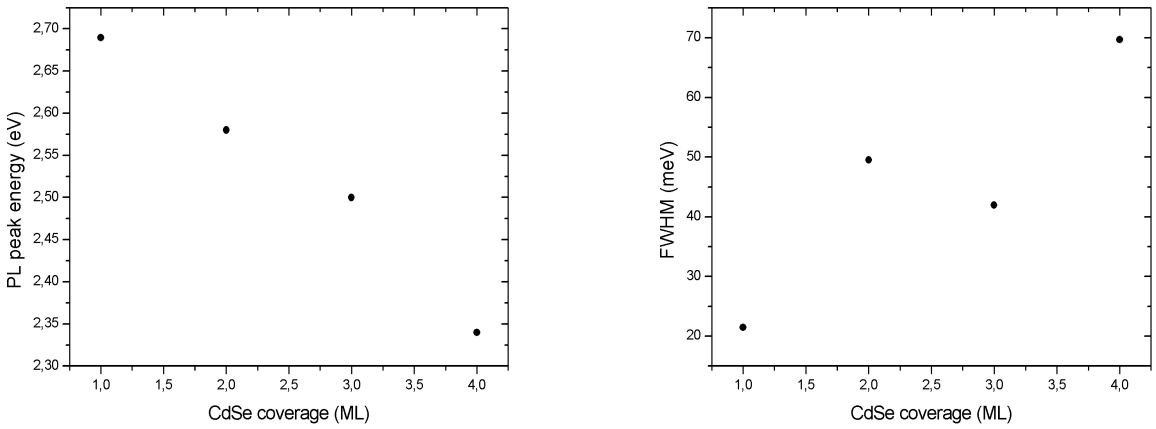

Figure 4.17: 80 K PL peak energy position and FWHM of samples with different CdSe coverages prepared by the amorphous Se method.

4.4.2 Raman measurements

The Raman spectra were also recorded at 80 K. For the 1 ML CdSe sample the evaluation of the Raman spectra is hampered by the dominating underlying PL intensity for the 457 nm excitation wavelength and by the strong straylight intensity for the remaining excitation energies (fig. 4.18 part (a)). The derivation of the peak position basically only reveals the ZnSe LO phonon. The analysis of the QD-phonons of the 2ML sample is performed for the 457nm and the 477nm laserline. Both excitation energies yield spectra with phonons from the QDs and also the GaAs LO phonon is visible. The occurrence of the GaAs phonon in spite of the light absorption in the QDs is due to the very small thickness of the QD layer and possible areas of low Cd content. For the remaining excitation energies no significant phonon scattering intensity from the QDs are visible. This behaviour is different for the 3 ML sample. Here the only excitation energy which is below the QD layer gap is the 514 nm laserline. However a QD phonon signal and the GaAs phonon are marked. Usually an excitation far below the PL emission energy results in negligible QD phonon contribution to the Raman spectra. This is a finding from the samples produced by the other fabrication methods. However the spectra for the other excitation energies fit well in the framework of the resonant Raman spectroscopy, as the signal intensity of the QD vibration is increasing with the excitation energy getting closer to the PL energy of the QD layer. Best seen when comparing the spectra of the 457 nm excitation wavelength consisting of ZnSe, QD and GaAs phonons with the other wavelengths (477, 488 and 496 nm). Here the spectra are dominated by the QD vibration signal. This characteristic is unchanged for the 4 ML sample, except for the fact that no excitation below the QD PL energy is possible with the employed Argon-Ion laser. The evaluation of the phonon energies in this case involved subtracting the background signal of the spectra by a linear function or by an exponential function depending on the course of the background signal.

The background signal can originate from the PL of the QDs or from laser straylight entering the monochromator resulting in an exponential signal increase towards the laser line at zero wavenumber.

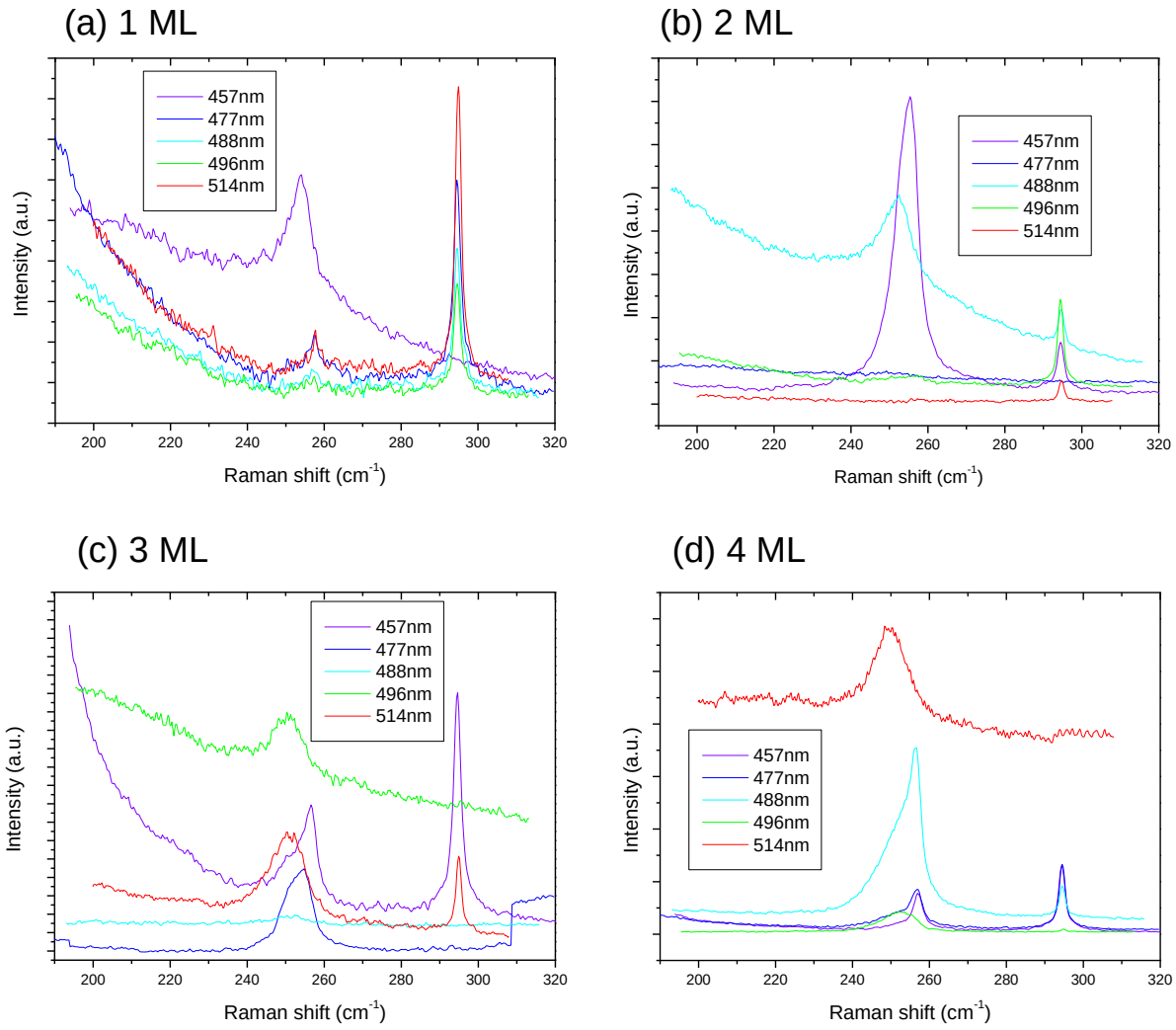

Figure 4.18: 80 K Raman spectra of the sample series with different nominal CdSe coverages prepared by the amorphous Se method.

4.4.3 Cd-"loss" and nominal coverage

This subsection describes the analysis of a series of samples, grown by the a-Se decap method, which were designed for the purpose of determining the possible Cd diffusion by the X-ray interference method. The basics of this concept are described as follows: The thickness of an MBE grown layer is normally determined by the time the cell shutter is open. The relation between growth time and layer thickness is achieved with a very high accuracy by calibration samples, in which the MBE layer of interest is overgrown by an

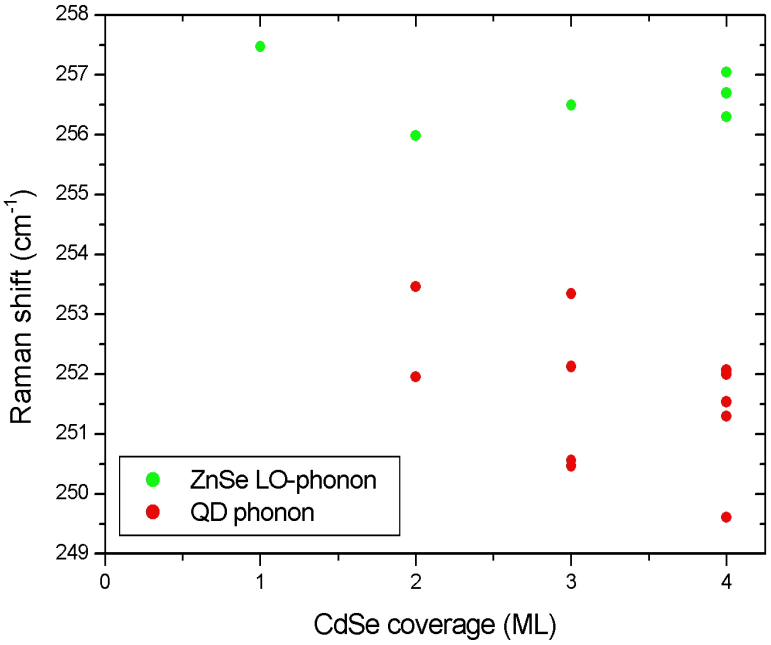

Figure 4.19: Phonon energy dependence on the CdSe coverage of samples prepared by the amorphous Se method (T = 80 K).

epitaxial cap layer. With X-ray diffraction, the thickness of the layer of interest is determined from the X-Ray interference (XRI) pattern, which originates from the interference of the X-rays, which are diffracted from the epitaxial cap layer and those from the material below the layer of interest. The thickness of the latter layer of interest determines the phase difference of both interference contributions, and thus the diffraction pattern. In this way, layers with very precise nominal thicknesses in the submonolayer range can be produced. When growing these QD samples and analyzing the CdSe coverage afterwards there was a significant discrepancy between the nominal deposited CdSe amount and the actual thickness, determined by interference fringes in XRI. As it became clear that this was a systematic deviation the question arose where the Cd "went". In principle there are different possibilities of the Cd "loss".

- The Cd desorbs during growth of the QDs.
- During the QD growth or overgrowth the Cd is incorporated in the ZnSe layer beneath or above the QDs. It is also possible that the Cd is incorporated in both ZnSe layers.
- Another possibility is that the XRI method has its limits when analysing dot layer thicknesses (Esc07),(Mah07).

To analyze this deviation a sample series with five different CdSe thicknesses d_{CdSe} was grown 4.1. The desorption temperature for the amorphous Selenium in this case was chosen to 230°C which was also the temperature for the ZnSe cap growth.

sample:	nominal d_{CdSe} (ML)
CB3205	0,9
CB3206	1,7
CB3207	2,2
CB3208	2,6
CB3209	3,0

Table 4.1: Nominal number of deposited CdSe monolayers in a-Se decap sample series, grown for X-ray interference analysis.

The Cd-loss of these samples is depicted in fig. 4.20. In the figure the ordinate is defined by $\Delta d = d_{nominal} - d_{measured}$.

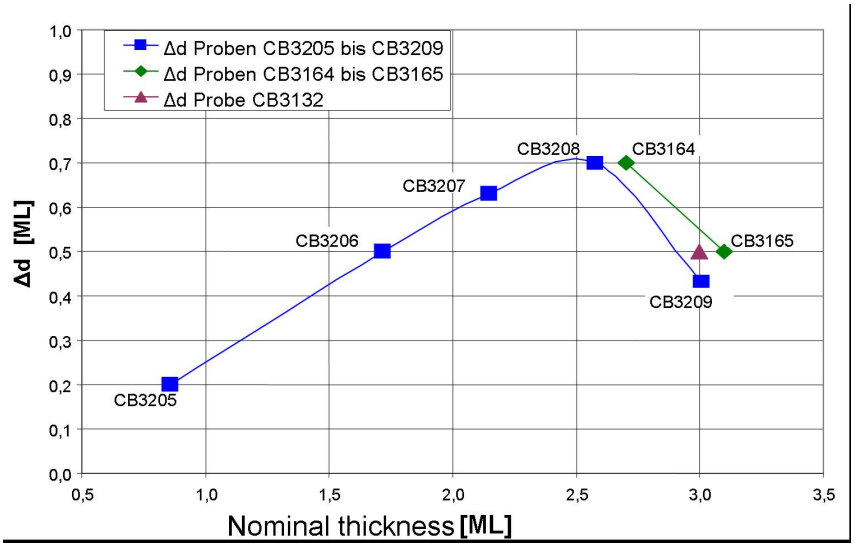

Figure 4.20: Nominal deposited CdSe thickness and the CdSe deficit (in monolayers of CdSe) (from (Esc07)).

In Raman spectroscopy, as already observed on other QD samples the ZnSe-phonon showed a slight shift in its frequency (esp. for high CdSe coverages). So the idea was to investigate whether there was a link between the determined Cd-loss and the ZnSe-phonon shift. With this information it is easy to conclude whether the Cd desorbs during growth or is at least partly incorporated into the ZnSe matrix. Raman spectra were recorded from the sample series, listed in tab. 4.1 with all available excitation wavelengths. As the focus of the evaluation here concerns the small shift of the ZnSe LO phonon, special attention has to be paid to the wavenumber accuracy. Therefore, the analysis of the peak position was performed in the following way. The peaks from the ZnSe, GaAs and CdSe were fitted with Lorentzian profiles and the energy distance between ZnSe/CdSe and the

GaAs signal was determined fig. 4.21. The GaAs signal position was used as a reference position of the spectrum so that also possible small inaccuracies in the monochromator calibration were compensated. The peak fits were performed for all laserlines whenever possible as the evaluation needs a visible GaAs and ZnSe signal. This can be hindered by the photoluminescence background or too weak Raman signal intensity from the ZnSe or GaAs depending on the excitation energy. The determined phonon position are comprised in 4.23. The dependency of the QD phonon position on the nominal CdSe thickness shows the expected linear course. However the shifted ZnSe LO phonon position has a minimum in its vibration energy for the nominal CdSe coverage of 2.6 ML. For the higher coverage the vibration energy is increased again, however it is still significantly lower than the bulk ZnSe LO phonon energy.

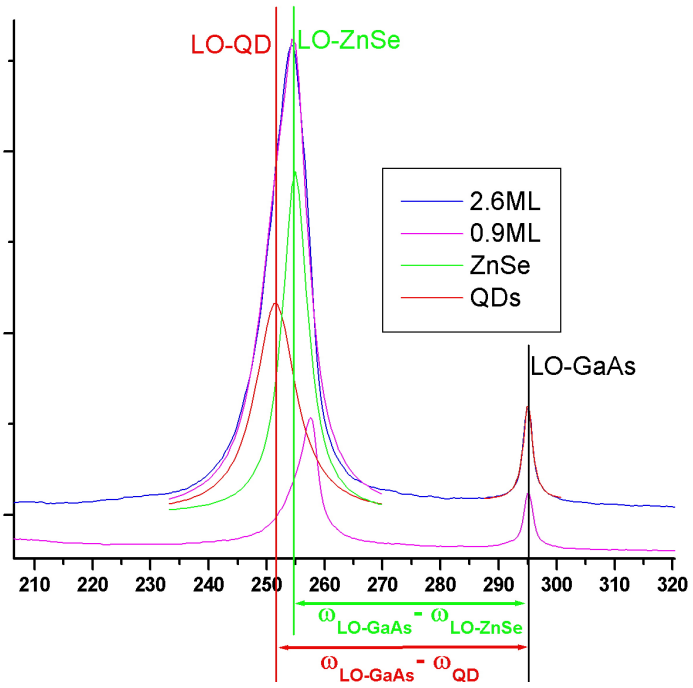

Figure 4.21: Exemplary 80 K Raman spectra of the 0.9 and 2.6 ML sample. For the 2.6 ML spectrum the fit (violet) of the LO phonon peak structure, consisting of the sum of two lorentzians, representing the LO-ZnSe (green) and the LO-QD (red) is also shown.

In conclusion the Cd-loss derived by XRI is consistent with the ZnSe-phonon shift measured by Raman spectroscopy. This is a clear indication of Cd-embedding in the ZnSe matrix. The loss of 0.7 ML of Cd for the 2.6 ML sample results in a local Cd-concentration of around 15% in the ZnSe-matrix, indicating an inhomogeneous alloying of the ZnSe matrix by segregated Cd. As the 3ML sample reveals a decreased Cd-loss and a decreased Cd-embedding in the ZnSe, this suggests a stabilization of the QDs. This hypothesis is backed by the fact that for conventionally grown samples with high QD density, the CdSe islands do not grow to the size wich is required for the stabilization of

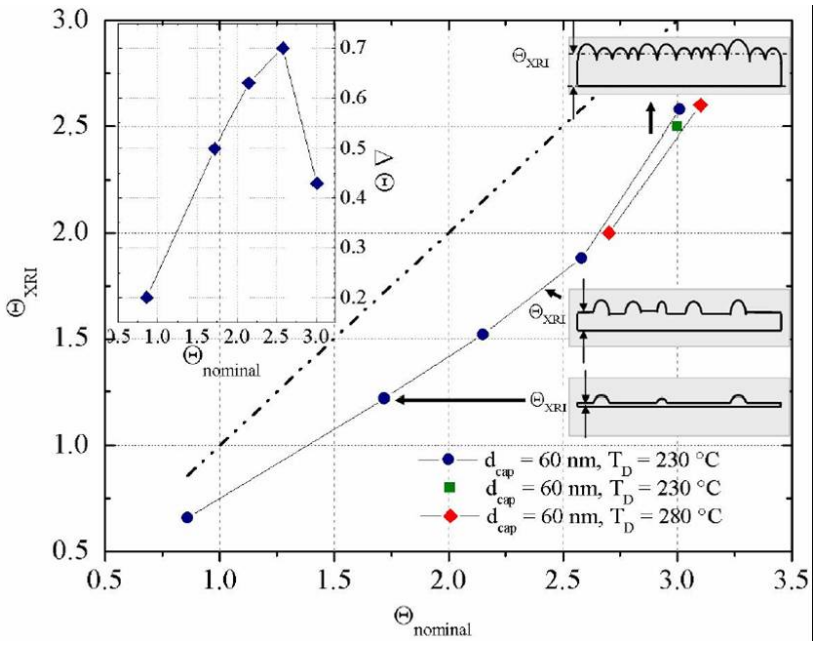

Figure 4.22: Comparison of the intended nominal CdSe coverage $\theta_{nominal}$ and the thickness θ_{XRI} derived by X-ray interference (from (Mah07)).

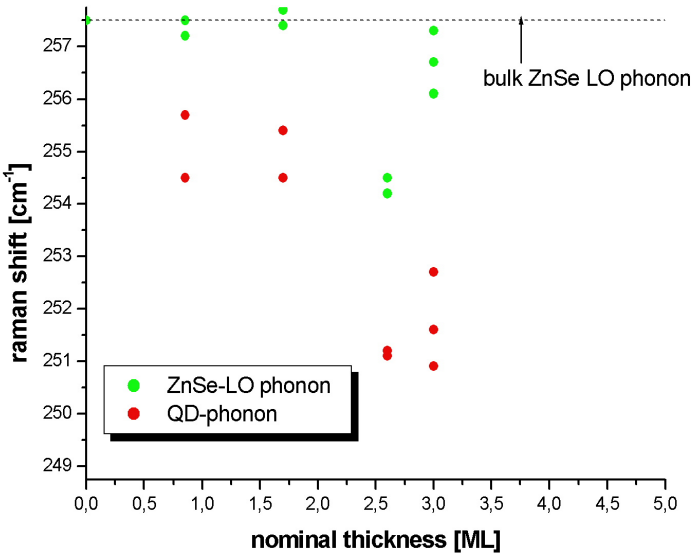

Figure 4.23: Phonon frequencies vs. nominal CdSe coverage

the QDs. This results in a monotonic increase of the Cd-concentration in the ZnSe-layer. The assumption of segregation is supported by the low surface diffusion length of Zn/Cd and the high strain between ZnSe/CdSe.

4.5 QDs formed by a-Te assisted growth

4.5.1 PL-Measurements

This section describes a samples series in which the QD formation was achieved by utilizing an amorphous Tellurium layer, which was subsequently desorbed. Thus, this sample series is an analogon to the amorphous Selenium assisted growth method. After the desired CdSe coverage was deposited, the sample was cooled down to approx. 50°C and a 10 nm thick amorphous Tellurium layer was applied. Subsequently, during the temperature ramp up to desorption temperature of T_D = 280°C, the tellurium was desorbed and "assisted" in the meantime the QD self-assembly. Finally, an epitaxial ZnSe cap layer was grown, whose thickness was around 45 - 50 nm.

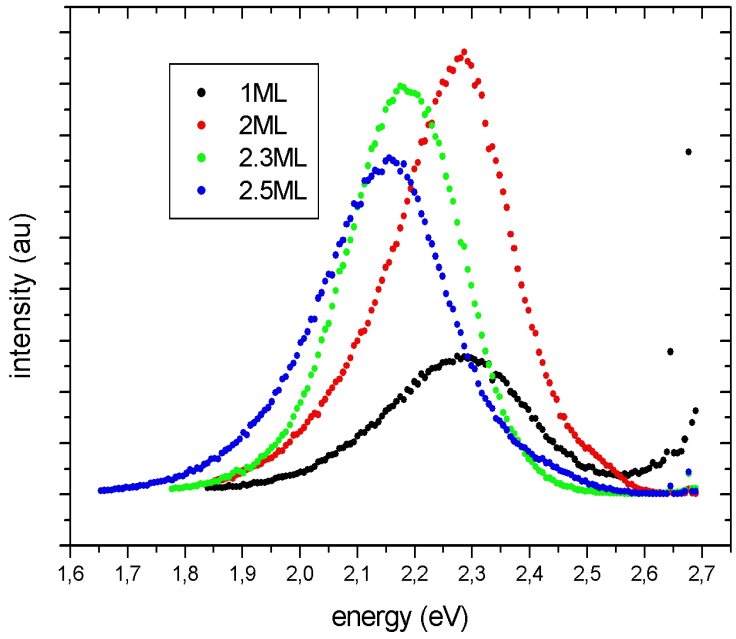

Figure 4.24: 300 K photoluminescence spectra of amorphous Te assisted QDs

The RT PL (fig. 4.24) of this sample series reveals some considerable difference to the other sample series concerning peak positions and halfwidths. This will be discussed in detail in the following.

The PL spectrum of the 1 ML CdSe sample consists of a single gaussian peak at an unexpected low energy of 2.28 eV and a significant ascent towards the excitation energy

of 2.71 eV. This strong rise is only seen in the 1 ML sample. The singular intensity maxima in the high energy part of the spectra are due to Raman scattering from phonons whereas the origin of the remaining background intensity is unclear. The halfwidth of the gaussian peak amounts to the very high value of 252 meV. This is around a factor of 10 higher than for conventionally grown QDs. At first glance, this might suggest completely different properties of this QD structure.

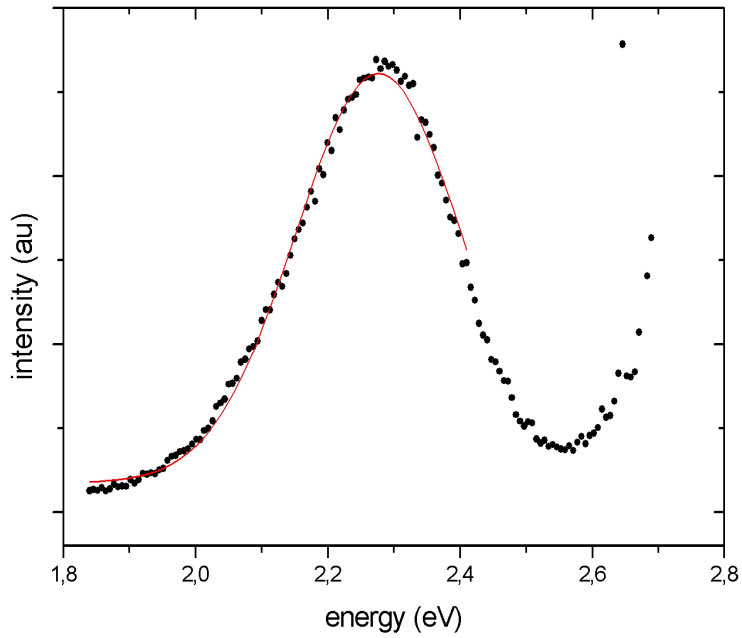

Figure 4.25: Gaussian fits of the 300 K PL of amorphous Te assisted 1 ML QDs

The 2 ML sample also gives a rather broad PL peak, as shown in Fig. 4.26. In contrast to the 1 ML case, now at least three gaussians are required for an accurate fit of the PL structure. The corresponding parameters of the gaussian fits are listed in 4.2. Interestingly the energy position of the peak with predominant intensity (nr. 2) corresponds to the single peak of the 1 ML sample, although with a decreased halfwidth. The low energy peak at 2.20 eV was not seen before and additionally is also very broad (FWHM = 0.279 eV). The high energy peak 2.48 eV only has a small but non-negligible intensity. The energy of this peak coincides with the position of conventionally grown QDs. As this peak is seen at 300 K where the excitons can perform a higher lateral diffusion before recombination, this indicates substantially extended regions of the layer without QDs with low gap energy. Otherwise virtually all excitons would diffuse into these energetically favourable dots and the recombination would occur at the corresponding energy levels.

The PL spectrum of the 2.3 ML sample basically consists of two gaussian shaped peaks. The high energy peak comprises the main intensity. Its position (2.19 eV) matches the low energy peak of the 2 ML sample. This is reasonable as the energy levels should

Coverage (ML)	Peaknumber	Peakposition (eV)	FWHM (eV)	rel. intensities
1	1	2.28	0.252	1
2	1	2.20	0.279	0.508
	2	2.29	0.156	0.468
	3	2.48	0.110	0.024
2.3	1	2.08	0.244	0.169
	2	2.19	0.187	0.831
2.5	1	2.09	0.291	0.449
	2	2.17	0.182	0.515
	3	2.40	0.139	0.036

Table 4.2: Compilation of the peak positions, halfwidths and relative intensities of the gaussian peaks, which constitute the PL spectra of the samples prepared by the Te-assisted growth process itemised by the amount of the nominally deposited CdSe (1-2.5 ML)

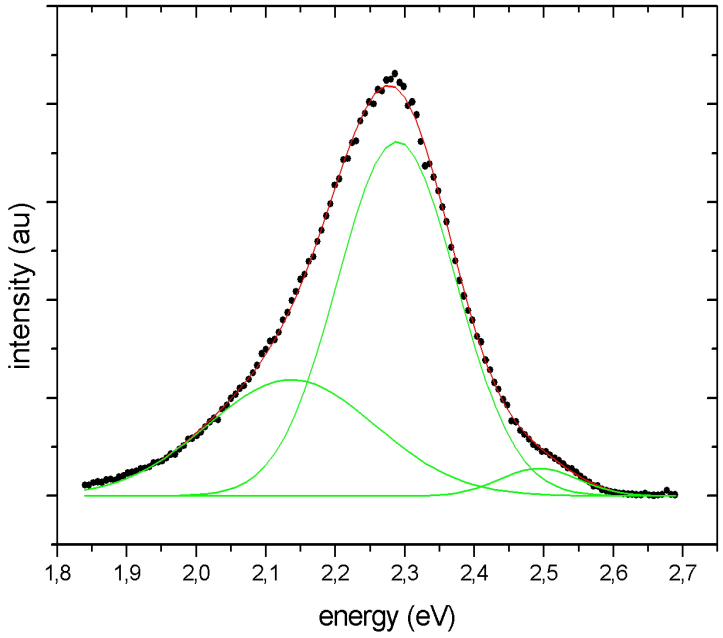

Figure 4.26: Gaussian fits of the 300 K PL of amorphous Te assisted 2 ML QDs

decrease with increasing CdSe thickness. The additional low-intensity peak at 2.08 eV owns a high halfwidth of 0.244 eV. The PL spectra of the 2.5 ML sample also owns the two peaks at 2.09 eV and 2.17 eV already seen in the 2.3 ML sample but surprisingly additionally contains a new high energy peak of 2.40 eV.

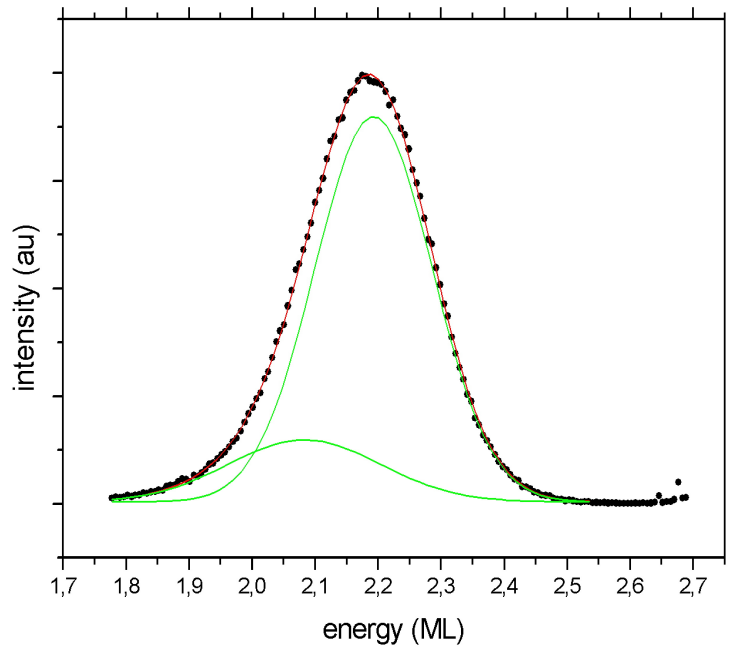

Figure 4.27: Gaussian fits of the 300 K PL of amorphous Te assisted 2.3 ML QDs

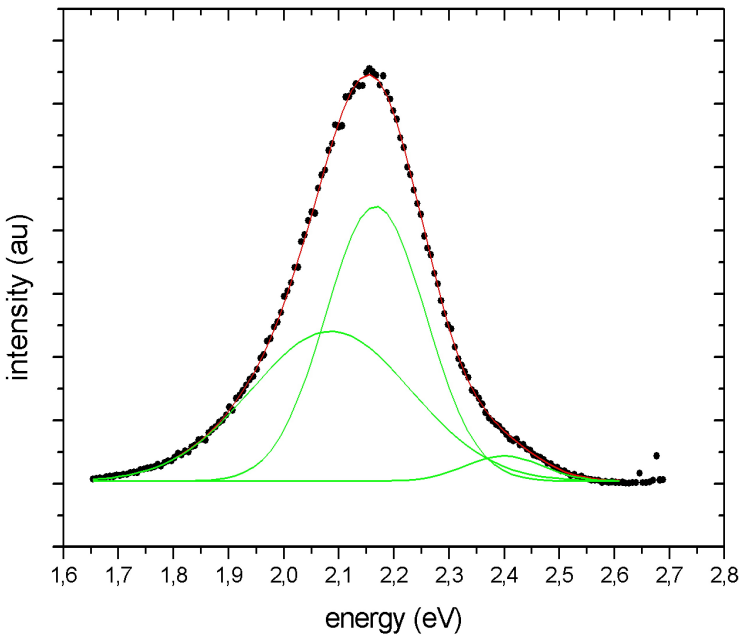

Figure 4.28: Gaussian fits of the 300 K PL of amorphous Te assisted 2.5 ML QDs

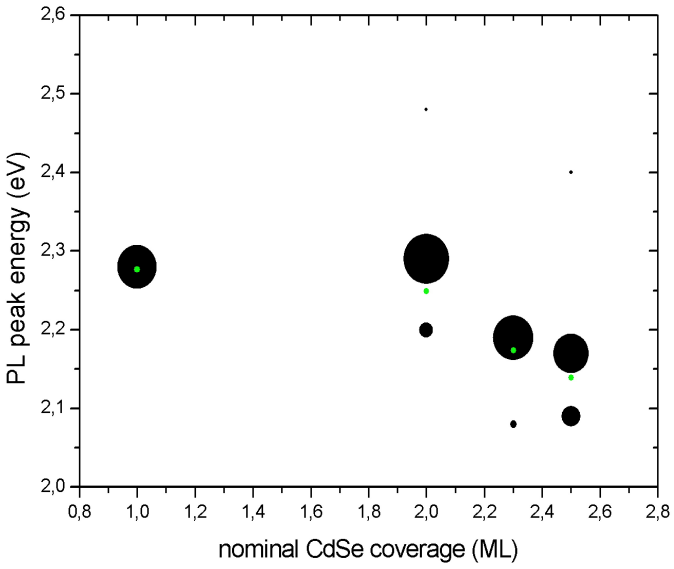

Figure 4.29: PL peak position dependency on CdSe coverage. The dot size indicates the peak height. The green dot indicates the center position of the spectral weight.

In graph 4.29 the PL peak positions of the sample series are illustrated. The peak heights of the fits are indicated by the dot size. This does not allow the comparison of the intensity between different samples but visually represents the intensity ratio for each sample separately.

The green dots in fig. 4.29 represent the center position of the spectral weight. They clearly confirm the trend of a decreasing PL energy with increasing CdSe coverage. The very broad PL signatures persist also at low temperature, even down to 1.6 K (Kie). This essentially T-independent broad PL will turn out to hamper the Raman experiments considerably (section 4.5.2). When evaluating the PL spectra of this sample series, it is insufficient to consider for the assignment of the PL peaks only recombination at the gap of the QDs. In fact the Tellurium incorporation in the ZnSe and additionally in the CdSe has to be taken into account. Tellurium atoms or clusters in ZnSe act as isoelectronic centers with a distinct photoluminescence signature. Pairs of Te atoms give rise to the S1 emission around 2.64 eV (also called blue-emission) and clusters with more than two atoms emit the so called S2 intensity around 2.50 eV (also referred as green emission). For low temperature PL unequivocally a strong intensity of these peaks was reported, while the temperature dependent intensity seems to be sample-dependent. Claims imply persistence of the S1 beyond 95 K and of S2 up to 200 K (DGH$^+$92), persistence of both peaks up to 180 K (CCS$^+$08), and of S2 up to 300 K (SKI$^+$08). The reasons for this different behaviour are unclear but it could be for example the crystalline quality as the samples from (DGH$^+$92) are grown by MOVCD and the others by MBE. Nonetheless the common property of the reported results is the remarkably high FWHM of the PL signal from the isoelectronic centers (in excess of 100 meV for all

measurement temperatures and regardless of originating from the S1 or S2 luminescence (SKI+08),(TIT+95),(GKvdV+05)). For this reason the PL signature of the sample series is analyzed with regard to additional PL intensity from Tellurium atoms in ZnSe. For the 1 ML CdSe sample which shows two features: a pronounced broad peak at 2.28 eV and also luminescence in the range from 2.6 eV to 2.71 eV, the broad peak is assigned to the Tellurium, as from the other growth procedures 1 ML CdSe never gave intensity at such low energy values. Also it would be quite surprising if the 1 ML CdSe in this case is not consumed to build up the wetting layer for the QDs. Also seen from fig. 4.29 the peak position does not fit in any way in the dependency of the nominal coverage vs. peak energy position. The conclusion is the following: The broad peak is Tellurium based and the signal from the wetting layer is in the range of 2.6 eV to 2.71 eV and may be additionally reduced or even quenched if the excitons from the wetting layer are recombining in the neighbouring Tellurium doped ZnSe layer. For the higher CdSe coverages there can be in principle four recombination channels. CdSe luminescence may arise from the wetting layer and from the QD structures. Moreover, the Tellurium can contribute by S1 and S2 isoelectronic centers. For the 2 ML sample, the main peak at 2.29 eV, which was also seen on the 1 ML sample is explained in terms of the S2 luminescence of Tellurium. The weak high energy peak (2.48 eV) of the spectrum is most probably due to the S1 luminescence. The QD luminescence can explain the small peak at 2.20 eV. As the coverage is rather low only few large QD-like structures can develop. Because of the low QD density, for a considerable part of the S2 centers the associated wave functions have no spatial overlap with a QD, and the PL of the S2 is not totally quenched and the spectrum consists of both signals. For the 2.3 ML sample the peak at 2.19 eV is only slightly shifted to lower energy, meaning that the size of the QDs does not significantly change but the density increases. The density increase can also explain the quenching of the S2 luminescence as the QDs "steal" its intensity and circumvent the S2 signal contribution. In addition, it is likely that some Tellurium is incorporated in the QDs, this results in a lowering of the QD PL energy. This could explain the peak at 2.08 eV and is also backed by the fact that the low energy tail of this peak reaches down to the bulk bandgap value of pure and unstrained CdSe. In the examined pseudomorphic samples a total relaxation to the bulk values of CdSe is highly unlikely as it should be detected by the X-ray measurements and also result in crystal defects. So the Tellurium incorporation in the QD is more or less the only possible way to shift the energy to such low values. For the 2.5 ML sample this trend continues. The QDs tend to be a bit bigger and their energy is redshifted. Although, the main difference to the 2.3 ML sample is that the luminescence contribution of the QDs is increasing. The small peak at 2.40 eV may be assigned to S1 and/or the wetting layer luminescence. Te incorporation in the QD is probably favoured by their larger extent and also by some degree of relaxation. Therefore the lattice mismatch is reduced. So for higher coverages it is reasonable to conclude that the CdSe dots contain some Tellurium. This explains the low-energy tail of the PL spectrum.

4.5.2 Raman results

As seen in the previous section, the PL of this sample series is very broad and almost totally covers the energy range which is accessible with an Argon Ion excitation source. For the 1 ML and 2.3 ML coverage this means that for the measuring temperature of 80 K the excitation energy values coincide with the PL energy. Therefore the Raman spectra fig. 4.5.2, 4.5.2 are completely obscured by the strong PL signal. For the 2 ML and 2.5 ML samples it was possible to get Raman spectra for the 457 nm excitation wavelength. They show two partially overlapping peaks, which are representing the lattice vibration of the ZnSe matrix and the QDs (figs. 4.31). With the 477 nm excitation wavelength, the 2.5 ML sample also shows a Raman signature (251.3 cm^{-1}) on top of the quite strong PL background which is in the range of the QD vibration. Due to the interfering PL intensity this Raman result should be treated with care. The other excitation energies overlap with the PL signal and yield no evaluable phonon information of the samples. The results of the 457 nm and 477 nm excitation are listed in fig. 4.32. For this sample series it was not possible to employ resonant Raman conditions and derive vibration information of wetting layer and QDs separately. Nevertheless, the spectra confirm a clear similarity with the Raman spectra of the former series. Although the morphology and the PL results are quite different to the other growth methods, the determined vibration energies are in the same range. However a quantitative assessment of the possible Tellurium incorporation in ZnSe oder CdSe can not be given, due to the fact that Tellurium and Cadmium both shift the ZnSe LO frequency in the same direction. If the Tellurium is included in the QDs then it most likely should be in the top region of the lesser strained part. This is accompanied by a low local bandgap therefore resonant Raman conditions are not applicable because of the strong PL background.

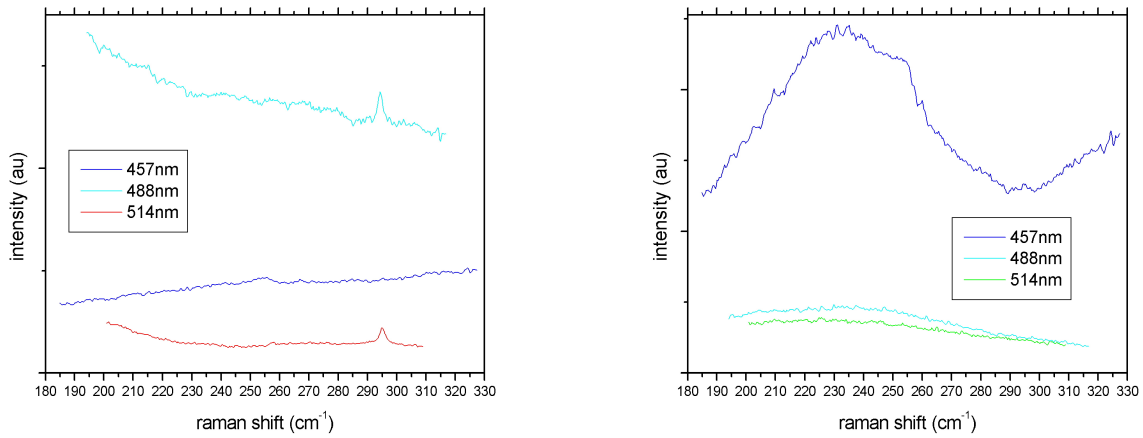

Figure 4.30: 80K Raman spectra of the Te-assisted growth of 1 ML (left side) and 2.3 ML (right side) CdSe QDs.

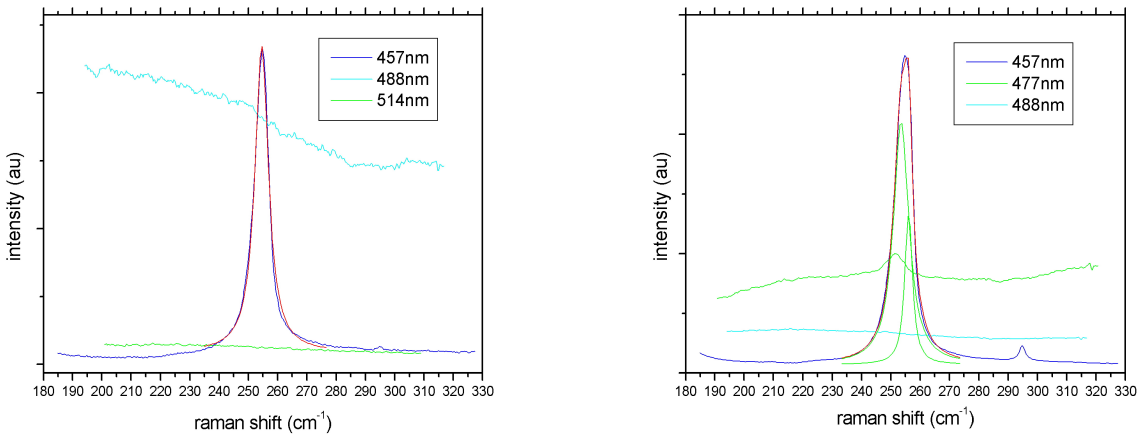

Figure 4.31: 80K Raman spectra of the Te-assisted growth of 2 ML (left side) and 2.5 ML (right side) CdSe QDs.

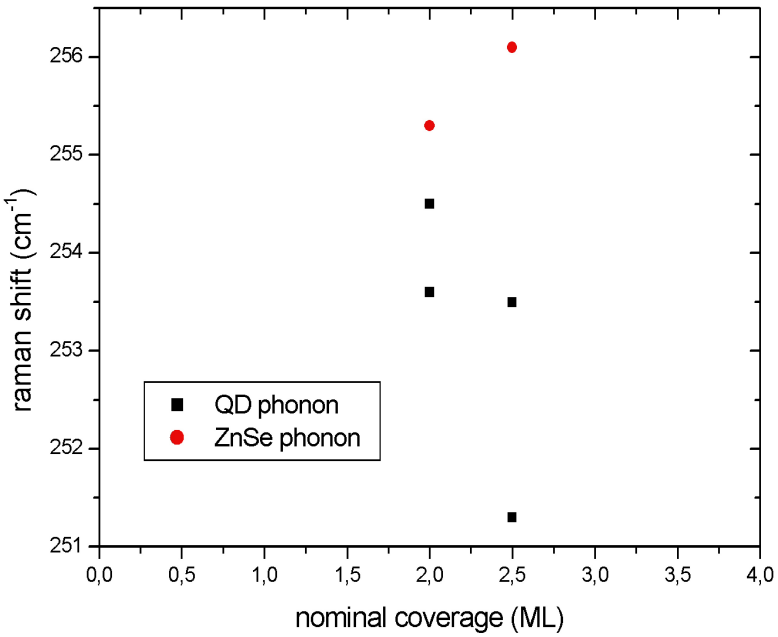

Figure 4.32: Phonon frequency dependence on the nominal CdSe coverage at 80 K measurement temperature

An alternative way to derive Raman results from this sample series was to increase the measuring temperature to 300 K. This is an uncommon way but in this special case the PL redshift was higher than the halfwidth increase and so it was possible to gain

Raman spectra without the interfering PL background signal. For the 457 nm excitation the spectra of the different CdSe coverages mainly consist of the resonant excitation of the LO-phonon of the ZnSe matrix fig. 4.33 . This is seen by the triangular lineshape and the peak position at 253 cm^{-1}. The resonance is so high that the GaAs LO signal in this case is completely covered by the PL background and the ZnSe LO-signal. Besides the ZnSe vibration there are no indications of other Raman signals. The excitation with 477 nm wavelength photons reveals the GaAs LO-phonon and a shifted ZnSe-like LO-phonon at around 250 cm^{-1} fig. 4.34. As the peak position spreading in the sample series is only 0.7 cm^{-1} (analyzed by fitting the GaAs LO and the ZnSe-like phonon and determining the energy difference between both values), one can safely conclude that this is not a vibration signal of the QDs. The different size and/or composition of the QDs results in a changed phonon energy and this should be seen in the Raman measurement if the signal is from the QDs. However, it is rather difficult to ascertain whether this is the Raman signature of the wetting layer (which should stay more or less the same in between the sample series) or a signal from either Cd or Te incorporation in the ZnSe matrix.

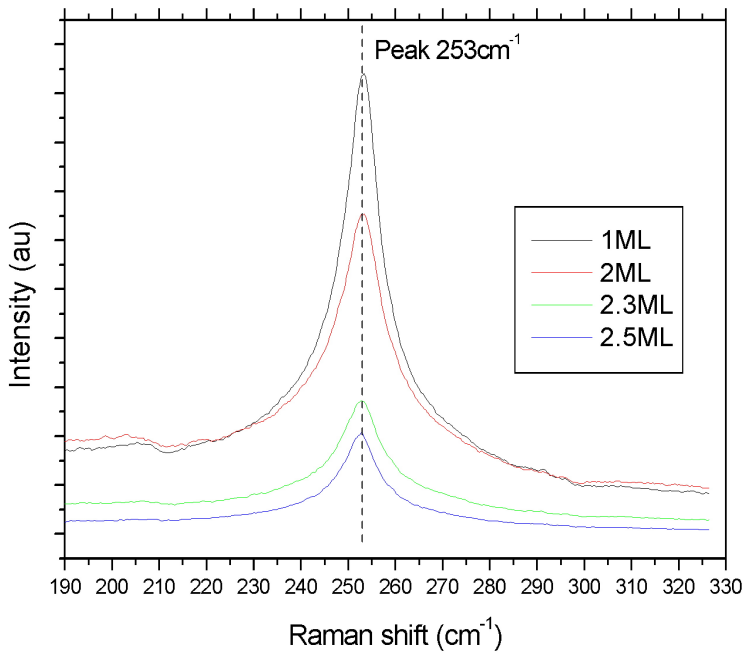

Figure 4.33: 300 K Raman spectra of the Tellurium assisted growth sample series, excited by 457 nm laserlight.

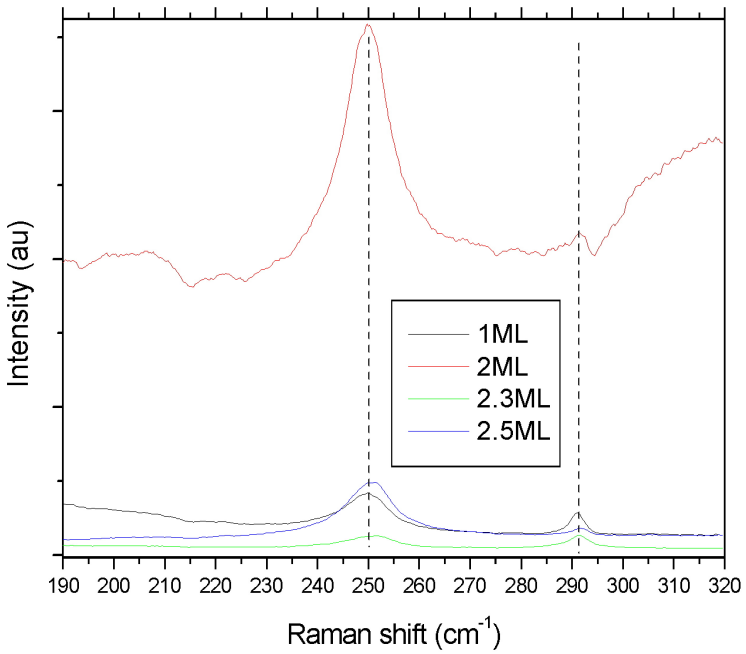

Figure 4.34: 300 K Raman spectra of the Tellurium assisted growth sample series, excited by 477 nm laserlight.

4.6 Uncapped QDs

All the optical investigations which were reported in literature up to now for CdSe quantum dots on ZnSe were performed on QDs with an epitaxial overlayer, whereas the AFM studies were carried out on samples with uncovered QDs which were transported to the AFM setup in air. This bears for the AFM studies some uncertainty whether the QD layer undergoes changes under the environmental influence of air and moreover, for the optical studies it is unclear whether the morphology was changed due to the overgrowth with ZnSe as this impresses additional strain from the top on the CdSe layer. Besides, during the ZnSe epitaxy process also diffusion of Cd in the ZnSe can occur as shown in TEM-pictures of this material system (fig. 4.3). In order to bridge this gap between optical spectroscopy and AFM analysis and avoid the imponderabilities mentioned above, one aspect of this thesis is Raman spectroscopy on uncapped QDs. This approach requires UHV conditions, for which purpose a dedicated UHV-optics vessel is employed. The aim of this Raman analysis is the observation of various stages of the development from a CdSe-layer towards the QD structure by annealing steps. Among the various procedures for QD formation, which were discussed above, the amorphous-Te or a-Se assisted QD formation procedure is the most eligible for this purpose. The a-Te or a-Se layer now has an additional function: beside its original role in the QD formation, it also protects the CdSe from environmental influences during the transfer under ambient conditions from the MBE to the UHV-optics vessel. As an additional protection, a double cap may be applied, e.g. an amorphous Selenium layer may be deposited on top of the a-Te layer (depicted in fig. 4.35). The amorphous Se or Se/Te double cap method for the sample transport in air was already successfully employed for BeTe(001) surfaces (WWH$^+$03) and for ZnSe(001) (DSZ$^+$96).

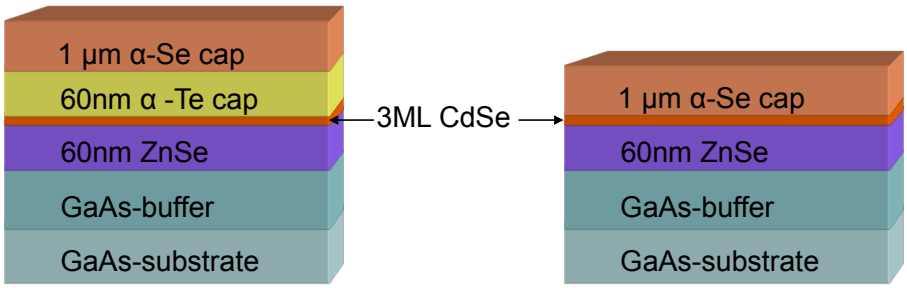

Figure 4.35: Sample layout employed for the UHV Raman analysis of uncapped CdSe-layers. The Te/Se or Se single cap are environmental protection during transfer and assist the QD formation during the decapping process.

Prior to the Raman analysis of the QDs, the cap is removed by thermal desorption under UHV-conditions in the optics vessel. The accomplishment of the desorption is checked by Raman spectroscopy, utilizing the Raman-active phonons of Se and Te.

Here, the description of the Raman analysis starts with the observation of the decapping, followed by the monitoring of the quantum dot formation in a series of annealing steps.

4.6.1 Decapping procedure

The sample structures for the Raman analysis of uncapped QDs (CdSe-thickness 3 ML) are shown in fig. 4.35. In both cases the Se-cap thickness is 1 μm, while for the double-cap additionally an underlying 60 nm Te layer is employed.

After their transfer to the UHV-optics vessel, the capped samples were analyzed by Raman spectroscopy before starting the decapping procedure. For recording this Raman spectrum a single-channel detector (photomultiplier) had to be applied instead of the OMA-based multichannel detection mode, as the rough surfaces of the cap layers induced too much straylight for the OMA detector, especially in the range below 200 cm^{-1}, which is required for the Raman detection of Te. This single-channel recording resulted in a significant enhancement of the acquisition time. Moreover, the maximum excitation power of the laser was limited by the requirement of avoiding local decapping in the focus area by laser heating. These restrictions led to Raman spectra with an enhanced noise level, fig. 4.36.

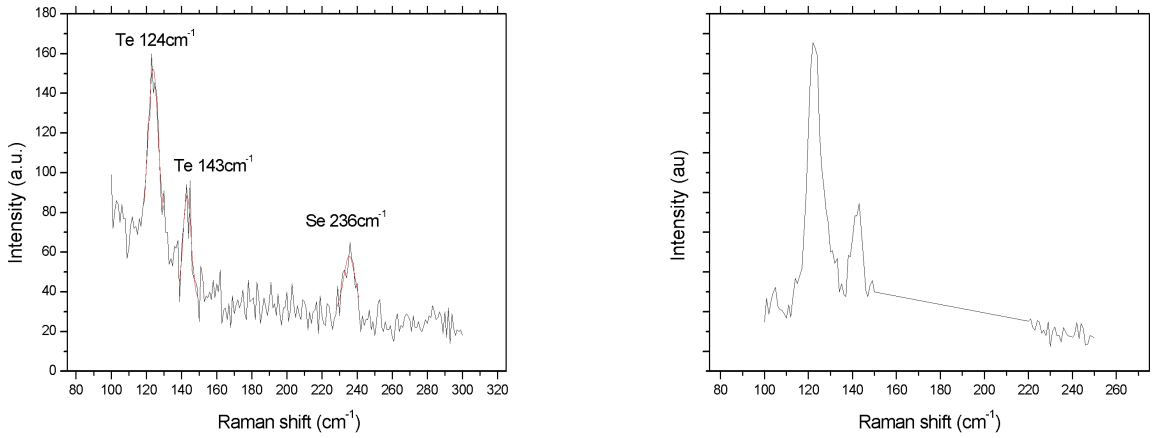

Figure 4.36: 300 K Raman spectrum of the double cap layer sample before annealing (left side) and after thermal removal of the Se cap (right side). Excitation wavelength in both cases: 514nm.

Nevertheless the phonon vibration of the Se at 236 cm^{-1} (LMT$^+$67) and the A1 mode at 124 cm^{-1} and the E-mode at 143 cm^{-1} (PD71) of the Te cap are clearly visible. The peaks are assigned to crystalline Tellurium, because for amorphous Te vibration energies around 157 cm^{-1} were reported (BGSY72). The slight shift (3 cm^{-1}) of both observed mode frequencies with respect to the reported values for single crystal Te in (PD71) is attributed to the micro- or nanocrystalline character and possible local strain of the very thin Te layer. The photon energy for this spectrum was chosen to be as low as possible to ensure a high penetration depth. However it is obvious from the spectrum that only the Se and Te layer are probed as there is no detectable Raman signal from the underlying CdSe, ZnSe and GaAs. Therefore no PL spectrum of the capped sample was recorded.

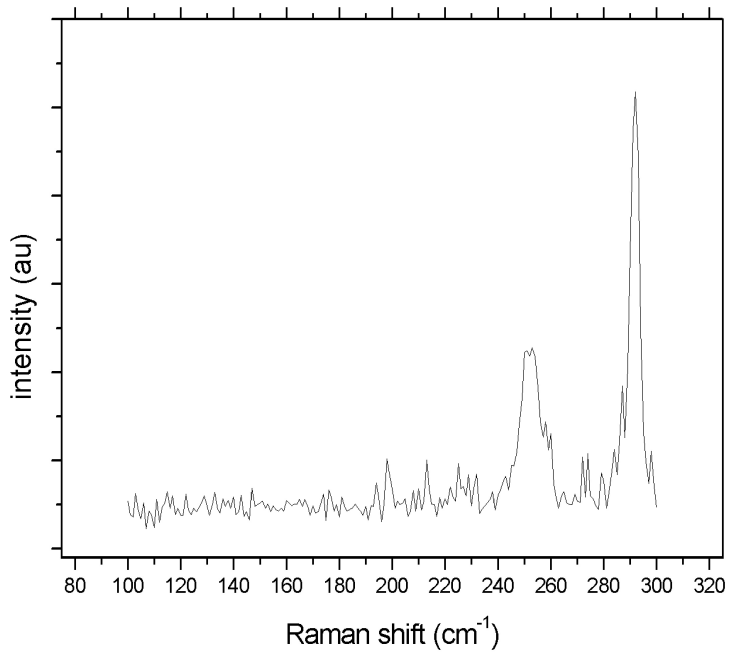

Figure 4.37: 300 K Raman spectrum of the double cap layer sample after thermal removal of the Se and Te cap layer, excited by 514 nm laserlight.

For desorbing in the first annealing step the protective Se cap layer, the sample was heated to a temperature of 130°C for about an hour. During this annealing step the surface changed from a dull to a glossy look indicating the removal of the Se-layer. This assumption is backed by the spectrum fig. 4.36 where there is no indication of remaining Se as it only consists of the crystalline Te vibration signal.

Subsequently, the Te cap was removed by annealing the sample at the elevated temperature of 230°C for an hour.

The Raman spectrum after this second annealing step confirms the removal of the Te layer fig. 4.37. The difference with the reported Te desorption temperature of 260°C (WWH$^+$03) is most probably due to the limited accuracy of the coupling of the thermal sensor. In detail, the successful Te desorption is confirmed by the clear occurrence of the GaAs LO phonon, and even more accurately by the absence of any Raman signature of Tellurium. The latter criterion is a very strict one, because the pronounced Raman activity of Te vibrations even allows the observation of a single monolayer, as shown previously for Te-dimers on a BeTe surface (WWG$^+$02).

4.6.2 Annealing-induced QD formation

In the following, Raman spectra are discussed which were taken to evaluate the CdSe- and ZnSe-phonon behaviour during a series of annealing steps. For reasons of accuracy, these spectra were taken at liquid nitrogen temperature after each annealing step.

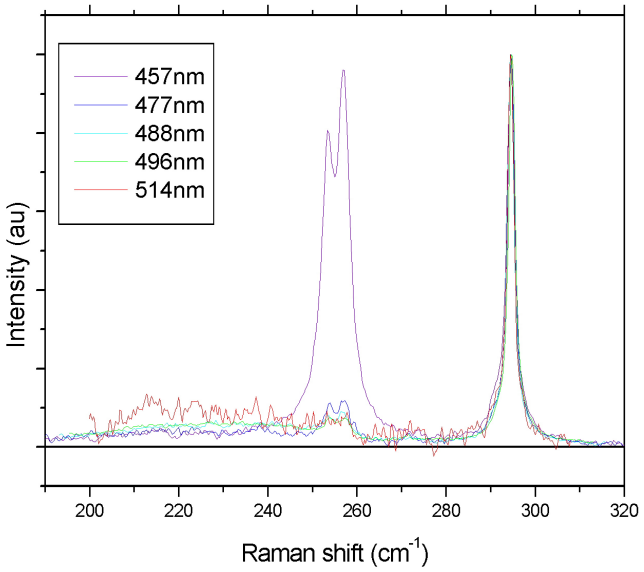

Figure 4.38: 80 K Raman spectra of the decapped sample for all Argon-laserlines normalized on the GaAs LO phonon.

As an introduction, fig. 4.38 shows a series of Raman spectra of a decapped sample, taken with laser lines from 2.71 eV to 2.41 eV. The essential result is the twin peak in the range 250 -260 cm^{-1} in the spectrum of the 2.71 eV laser line. The upper peak at 257.1 cm^{-1} originates from the ZnSe layer. Much more interesting for the QD formation is the lower peak at 253.4 cm^{-1}, which originates from the CdSe, as shown also in the previous sections. Its occurrence here for the uncapped CdSe is crucial, because this surface layer is not accessible by conventional optical analysis by photoluminescence because of nonradiative surface recombination processes.

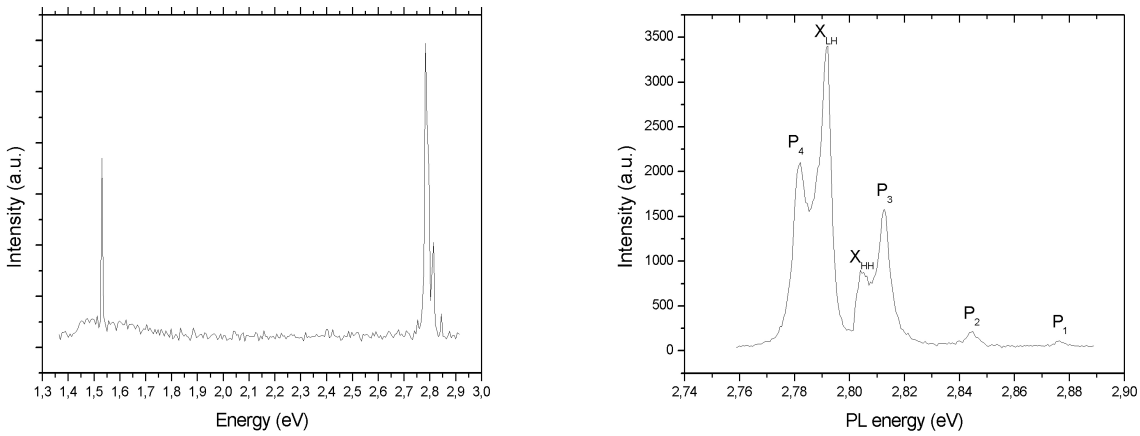

Figure 4.39: 80K photoluminescence spectrum after the decapping procedure (left hand side). Detailed section of the ZnSe PL signal (right hand side

.

The absence of the CdSe-induced PL is clearly shown in fig. 4.39, which is in strong contrast to all former PL-results on capped QDs, which showed an extraordinary high PL efficiency, centered in the green spectral range between 2.4 eV and 2.5 eV for 3 ML CdSe coverage. Therefore, the Raman signature constitutes the only optical tool for analysing the uncapped CdSe.

When comparing the various spectra in fig. 4.38, note the extraordinary resonance behaviour of the CdSe-induced peak. Its intensity is strongly coupled to its twin partner, the ZnSe-LO-peak. Both appear prominently for excitation at 2.71 eV, and strongly reduced at 2.60 eV, and even weaker for the other laser lines. This is the typical ZnSe resonance profile and in strong contrast to the behaviour of the capped QDs, discussed above, which have their own maximum in resonant Raman efficiency, coinciding with their PL peak energy.

The ZnSe-related Raman resonance behaviour of the CdSe-derived phonon and the absence of the PL-signature of the uncapped QDs have a common explanation: Because of the surface-induced non-radiative decay of the QD-excitons, the Raman scattering process of the CdSe-related phonon can only occur when the virtual electronic transitions in the underlying ZnSe act as mediators in the photon-phonon interaction. This spatially indirect process occurs due to the non-vanishing penetration of the ZnSe orbitals into the CdSe-layer.

Prior to discussing the behaviour of the CdSe- and ZnSe phonon during annealing, first the PL spectrum (left hand side of fig. 4.39) is considered in more detail. Its essential features are the GaAs-peak around 1.5 eV and the ZnSe PL structure, centered at about 2.8 eV. The latter has a multiple peak shape, shown in more detail on the right hand side in fig. 4.39. Two of these peaks are assigned to excitonic recombinations X_{LH} and X_{HH}, split due to strain in the ZnSe layer. Biaxial strain in a zincblende semiconductor

layer results in a splitting of the heavy and light hole exciton (RCC+91). With the lattice parameters of ZnSe and GaAs (MBH+94), the thermal expansion of ZnSe and GaAs (LB99),(S.82), the stiffness constants of ZnSe (H.70), the hydrostatic potential and the deformation potential (SOVdW88) the calculated energy splitting amounts to 12 meV at 80 K. This value almost matches the energy difference of the peaks X_{LH} and X_{HH}, which is about 13 meV. The small deviation of 1meV can be mainly explained by the uncertainties of the parameters employed for the calculation, e.g. the lattice parameter of ZnSe at 80 K (only linearly approximated) or the temperature dependence of the stiffness constants.

The remaining four peaks P_4-P_1 belong to LO phonons. They originate from high-order Raman scattering of the incident laser light (406 nm, 3.05 eV). Their intensity is resonantly enhanced, because of the proximity of the outgoing photons to the exciton energy (outgoing Raman resonance). This assignment is underscored by the temperature dependence of the peak positions in the range between 80 K and 140 K. The peaks X_{LH} and X_{HH} have a temperature coefficient of 0.33 meV/K and 0.38 meV/K, respectively, while the coefficient of the other peaks is below 10^{-2} meV/K. This fits well with the expected values for excitonic and phononic anharmonicity effects. The very strong enhancement of high-order LO Raman scattering at the exciton energy is a consequence of the pronounced polarity of the LO-phonon in II-VI compounds. The high FWHM of the phonon peaks (about 5 meV) reflects the spectral width of the exciting laser diode. It inhibits the deconvolution of the peaks into ZnSe-induced and possible ZnCdSe-induced contributions.

Now, the attention will be focused on the annealing behaviour of the CdSe- and ZnSe-phonon, which constitutes the main objective of this section. Because of the resonance enhancement, which was shown in fig. 4.38, the 457 nm laser line is applied for this purpose. The results for the Se-cap sample are shown in fig. 4.40 for annealing temperatures up to 310°C.

Starting from the first annealing step at 80°C, the twin peak with its narrow constituents appears. This structure persists up to the highest applied annealing temperature. The ZnSe phonon position amounts to 257.3 cm^{-1} and remains constant throughout the annealing. The initial CdSe phonon position is 255 cm^{-1}. This peak is actually shifted during the annealing. In fig. 4.41, its spectral position is plotted, together with the ZnSe LO-phonon position. Obviously, a step-like redshift of 0.7 cm^{-1} occurs between 200°C and 230°C.

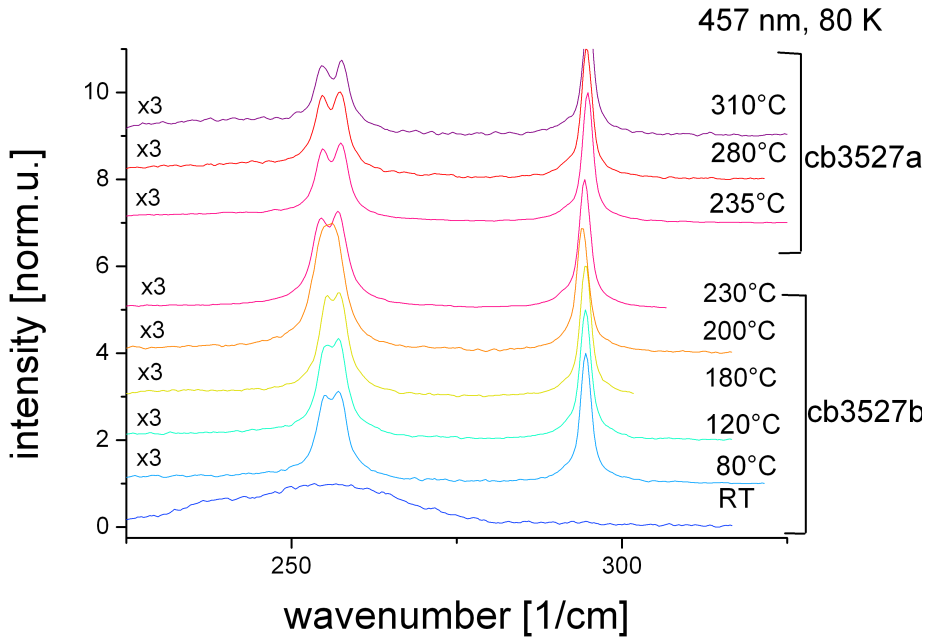

Figure 4.40: 80 K Raman spectra of an a-Se-capped 3ML CdSe sample at RT and after decapping and application of various annealing steps. Laser wavelength: 457 nm.

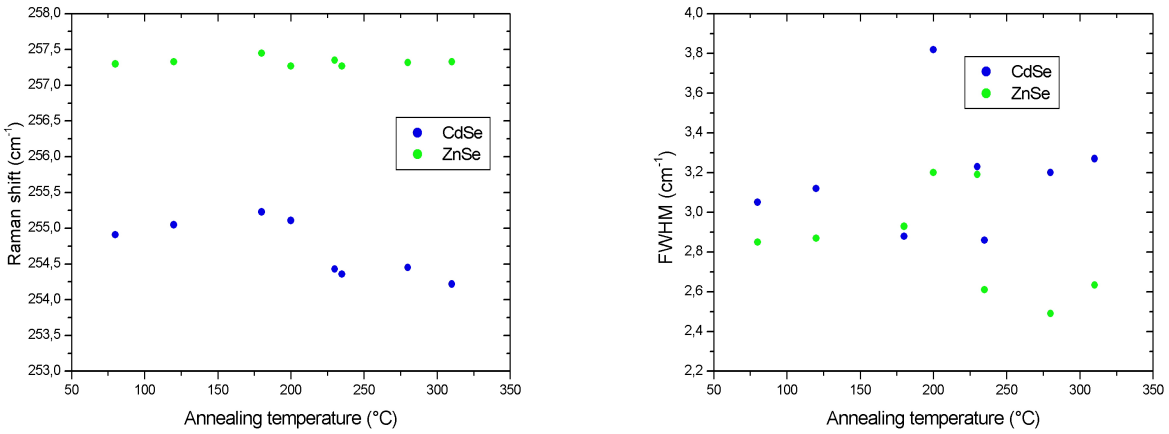

Figure 4.41: Peak positions (left side) and FWHM (right side) of the CdSe and ZnSe phonon peaks after removal of the Se-cap and application of different annealing steps.

In principle, such a peakshift may be a fingerprint of a change in composition and / or strain. Considering the impact of a composition change, the observed redshift would imply an decrease of the Zn-content in the (Zn,Cd)Se layer, i.e. a decrease of the intermixing. In view of the temperature enhancement, this seems highly improbable. If any thermally induced compositional change, one would expect an increased interdiffusion,

step	heat treatment
1	decapping of Te at 230°C for 1h
2	annealing at 280°C for 0.5h
3	annealing at 310°C for 0.5h
4	annealing at 310°C for 4.5h

Table 4.3: Synopsis of the heat treatment steps for the double cap layer sample

i.e. an enhanced Zn-content, reflecting itself in a blueshift. Considering as the second candidate for the peakshift a change of strain, one has to be aware that the starting position is a pseudomorphic CdSe-layer, i.e. a compressive strain, resulting in a blueshifted peak. Then the frequency shift actually is a reduction of this blueshift, i.e. a partial release of the compressive strain in the (Cd,Zn)Se layer. This effect is highly plausible in the given sample situation. It may be considered as a result of an increased undulation of the sample surface, the onset of QD formation. Finally, it should be noted that this QD onset might also imply a combination of both effects discussed above: for a strong undulation-induced strain relaxation together with a moderate increase of the Zn-content by intermixing, the net effect may well be a redshift, as observed in the spectra.

An investigation along the same line was also performed for the double cap (a-Te and a-Se) sample. However, in this case the study of the impact of the subsequent annealing steps is hampered by the Te-desorption temperature, which is as high as 230°C. By the inevitable exposure of the sample to this desorption temperature, the QD formation process may well occur prior to the subsequent systematic annealing steps at more elevated temperatures. Actually, this concern is confirmed by the results, shown in 4.42. This plot shows the CdSe- and ZnSe peak position after four consecutive annealing steps, whose conditions are described in tab. 4.3. Obviously, already at the first stage the CdSe peak has reached its final position, which value coincides with the high-temperature value of the single-cap sample. Therefore it is concluded that the QD formation already has occurred before, i.e. below 230°C.
When considering the peak widths, whose annealing dependence is also plotted in fig. 4.41 and fig. 4.42, the narrow shape of the CdSe peak is striking. Its FWHM values for almost all spectra for the single-cap and the double-cap sample are below 3.3 cm^{-1} and 3.8 cm^{-1}, respectively. These values are very close to the ZnSe peak width, and, moreover considerably narrower than all values, registered for the ZnSe-overgrown QD samples in the previous sections, which are about 7 - 13 cm^{-1}. This indicates that the inhomogeneous broadening due to Cd concentration fluctuations in the ZnSe-overgrown samples essentially develops by intermixing during the epitaxial ZnSe overgrowth.
Finally, attention is paid to the broad background structure in the frequency range 200 - 250 cm^{-1} of 4.38. It appears very weakly, essentially only in the 514 nm spectrum. Thus, its resonance behaviour is complementary to the CdSe- and ZnSe peaks. Therefore, the systematic study of its development with annealing, is shown in fig. 4.43 from a series of spectra which were recorded with the 514 nm laser line.

The peak structure corresponds to amorphous Selenium, its maximum originates from

the A1-mode of trigonal Se (LMT$^+$67), (BAM$^+$91). The temperature dependence in the range up to about 140°C compares with the report of the desorption of an a-Se cap from ZnSe(001) (DSZ$^+$96). Remarkably, the signature persists throughout the whole temperature range up to the highest annealing temperature of 310°C and even increases after the high-temperature annealing steps, although the Se cap layer should have been completely desorbed by then. For possible explanations of the prominent occurrence of the Se signal it must be considered that for the applied laser line the light absorption in the Se is very strong (Eg = 2 eV (Fis72)), and resonant scattering by the Se vibrations occurs, while the CdSe and ZnSe-modes are far off-resonant. Besides, the sharp peaks of the CdSe- and ZnSe-modes in the spectra of 4.40 do not give any indication for a deterioration of the crystalline quality. Polarization dependent experiments also confirm, that they fulfil the Raman selection rules very well, which is not the case for the Se signature. Therefore, the latter may be probably assigned to a very small fraction of Se inclusions and/or (nano)-droplets, which cause no detectable deterioration of the remaining crystal volume.

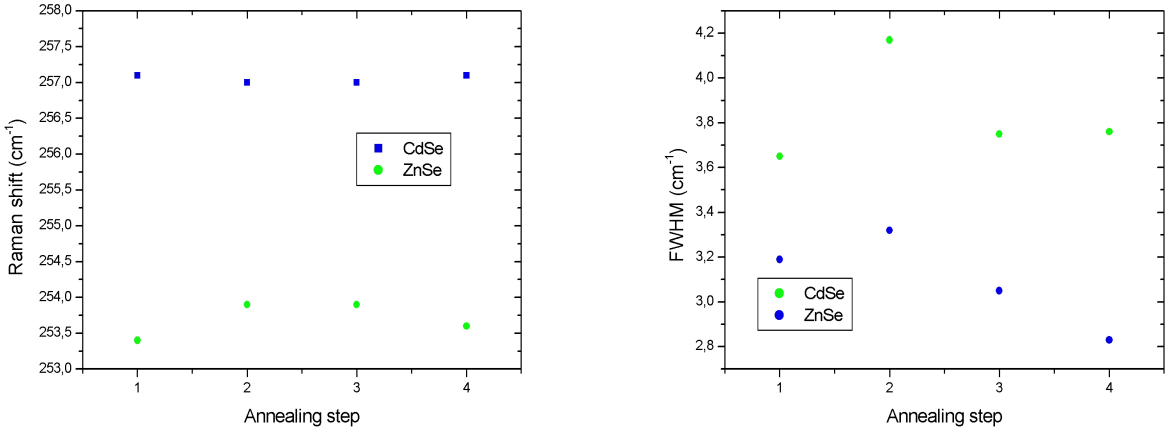

Figure 4.42: Peak positions (left side) and FWHM (right side) of the CdSe and ZnSe phonon peaks after removal of the Se- and the Te-cap and application of different annealing steps.

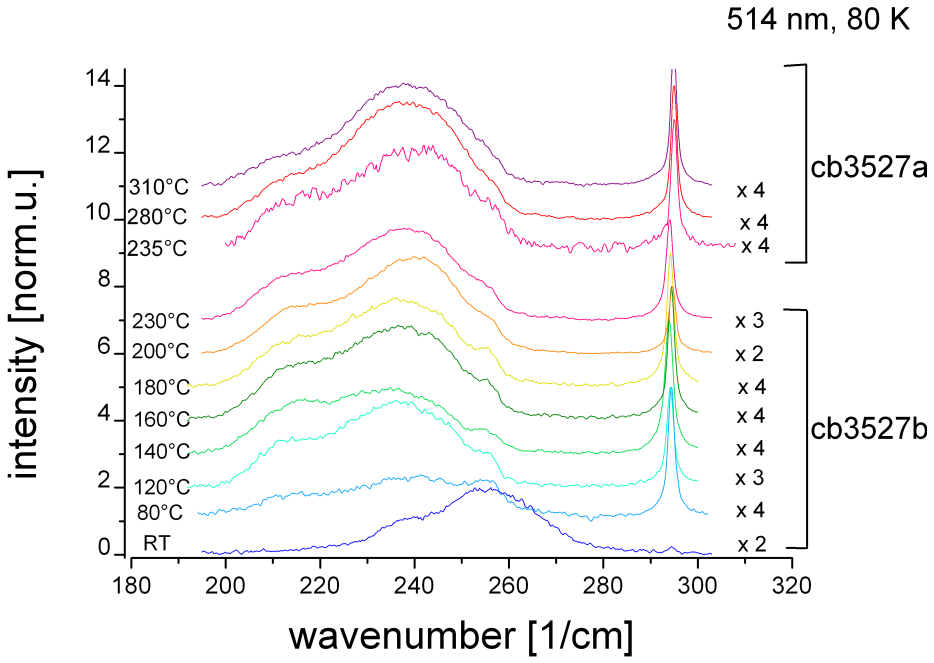

Figure 4.43: 80 K Raman spectra of an a-Se-capped 3ML CdSe sample at RT and after decapping and application of various annealing steps. Laser wavelength: 514 nm.

4.7 Comparison growth methods

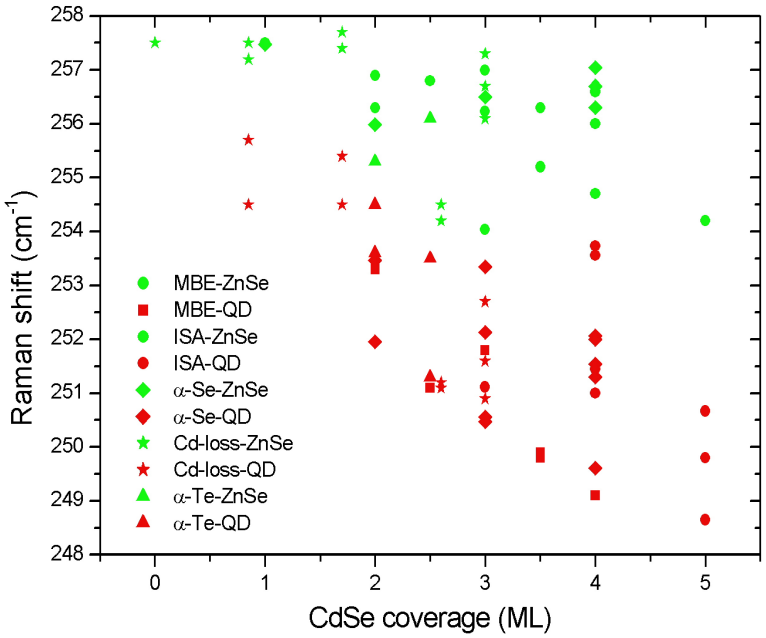

Figure 4.44: Comparison of 80 K ZnSe and QD LO-phonon frequencies of the QD samples from the different growth techniques. The abbreviation in the legend denotes: MBE are from samples by conventional MBE growth, ISA are samples from in-situ annealing, a-Se are samples from the amorphous Se-cap layer, Cd-loss are the samples also prepared by a-Se and investigated in the framework of the Cd-loss, and a-Te are from the amorphous Te-cap layer technique.

When concluding this chapter with a comparison of the results for the several investigated series of samples with different CdSe QD growth modes, first it can be stated, that all those QDs which were overgrown with epitaxial ZnSe show a remarkably strong photoluminescence efficiency, notably already at 300K. The optimum efficiency is achieved at about 3 ML CdSe nominal coverage. The subsequent reduction is attributed to a relaxation-induced formation of defects, which act as non-radiating centers. The photoluminescence peak position essentially shows a pronounced redshift with increasing CdSe thickness. In addition, the FWHM-values reflect a pronounced inhomogeneous broadening, attributed to the distribution of QD size and composition. All these features are similar for the various epitaxially ZnSe-overgrown CdSe QD series, essentially independent of the growth mode. The only exception are the QD samples produced by the a-Te procedure. Here in addition to the photoluminescence signal of the QDs, a prominent contribution of the PL intensity is the result of the isoelectronic Tellurium centers, incorporated in the ZnSe.

The Raman-derived peak position of the CdSe vibration mode from the QD and that

of the ZnSe phonon for all growth techniques are summarized in fig. 4.44. Also in this case a universal trend is observed for the several growth techniques: The CdSe-derived mode shows a clear redshift with increasing CdSe thickness, while the ZnSe mode also shows a redshift, although less pronounced. The evaluation of the QD phonon frequency in terms of the (Cd,Zn)Se composition yields for the 5 ML sample a maximum Cd-content of 45%. The Cd-concentration for the 3 ML samples from the different growth methods ranges between 21% and 37%. These values are in contrast to the high TEM-derived Cd-concentration for nominally similar CdSe QDs from (LSR$^+$08) but are consistent with the Cd-concentration from TEM, derived by (PRG$^+$00) shown in fig. 4.3.

By the Cd-"loss" analysis it was found that there is a correlation between the missing Cd in the XRI measurements and the phonon shift of the ZnSe. Therefore it can be concluded that the missing Cd is not solely desorbed during the ZnSe overgrowth but is incorporated in the ZnSe. This results in the formation of ternary (Zn,Cd)Se with locally up to 15% Cd intermixing.

For the uncapped samples the QD photoluminescence is quenched by surface traps. Therefore only the Raman spectrum gives optical information from these QDs. During step-annealing of Se-desorbed QDs (3ML), an obvious redshift of the QD LO phonon occurs at annealing temperatures of 200 - 230°C, which is explained by a reduction of the strain in the CdSe layer. This is interpreted as a morphology change of the layer towards more distinct QD structures. A compositional change due to increased intermixing with Zn or a thinning of the CdSe would result in a blue shift of the QD phonon frequency. So the effect of the morphology change at least constitutes the main if not solely contribution of the phonon redshift. This interpretation is underscored by the stability of the ZnSe LO frequency against the annealing steps: it remains constant and approximately at the bulk ZnSe frequency. This finding also implies that the moderate ZnSe phonon redshift which is observed for the capped QDs originates from the upper ZnSe epilayer due to Cd intermixing during overgrowth.

Chapter 5

n-ZnSe/n-GaAs Interfaces

5.1 Introduction

After having studied in the previous chapter the stoichiometry of quantum-dots by means of Raman spectroscopy from the lattice vibrations of the ternary $Cd_xZn_{1-x}Se$, this method will be applied in this chapter for studying the interface between doped ZnSe and GaAs for different procedures of the ZnSe growth start, which result in a large impact on the interface. Electrically this manifests itself by a drastic change of the resistance value. Raman spectroscopy offers the unique ability of a non-destructive analysis which gives besides specific information of each side of the interface. This possibility is applied in the framework of the investigation of the influence of the different growth start procedures of ZnSe on GaAs on the electronic properties of this doped heterolayer system. The focus is on the band potential characteristics, as this is of fundamental importance for spin dependent applications like the spin injection from a dilute magnetic semiconductor (DMS) into GaAs (RMG$^+$99),(GAK$^+$07), or for optical studies of coupled quantum wells in II-VI/III-V heterostructures (TSS$^+$05),(TSS$^+$06). These spin dependent devices are very sensitive to the electronic band characteristics (band offset and band bending) at the interface.

ZnSe on GaAs is serving as a prototypical system as it has been thoroughly investigated for more than 20 years. Raman spectroscopy has taken a prominent place in these investigations, which include samples from different growth methods like MBE (BBLG93), hot-wall epitaxy (JYH$^+$03), (YNO$^+$02), metal-organic vapor-phase epitaxy (MOVPE) (KAC$^+$99), (PRB$^+$91), pulsed Laser deposition (PLD) (GI99) or chemical vapor deposition (CVD) (LKK$^+$94). Additionally, Raman spectroscopy was also applied for in-situ growth monitoring (RZ98), (DLRZ94).

The electronic characteristics were analyzed by the band bending (ZTHH01), (WHW$^+$02) or the doping of the layers (KJL$^+$97), (SOP92), and by the generation of photocarriers (HCLLL$^+$97). The optical properties were addressed by photoluminescence while X-ray characterisation and Raman spectroscopy were employed to analyze structural properties, strain and relaxation (BBLG93), (Bra92), (BDK92).

However, no systematic study of the influence of the ZnSe growth start procedure (i.e.

the formation of the ZnSe/GaAs interface) on the band bending and carrier depletion layers in the interface region has been reported up to now.
From the viewpoint of fundamental physics, the heterovalent interface between a III-V and a II-VI layer poses a major challenge as the bonds from the two layers can not be perfectly matched. Additionally thermodynamic considerations reveal that a consummately abrupt interface of heterovalent layers is unstable. (FTdM$^+$91). Depending on the initial conditions, different atomic rearrangement and intermixing effects take place. The resulting atomic configuration at the interface determines the interface dipole moments, which have a strong influence on band alignment and depletion layers (KN94). Therefore the electronic properties may highly depend on the interface stoichiometry which can be intentionally altered by the growth start conditions of the interface. In order to study the effect of the growth start conditions on the electronic properties, i.e. the depletion layers and the conduction band barrier, a series of n-doped ZnSe/GaAs(001) heterostructures was grown by molecular beam epitaxy (MBE) with a controlled pre-deposition of different amounts of Zn or Se in the fractional monolayer range at the growth start of the ZnSe layer on the GaAs.

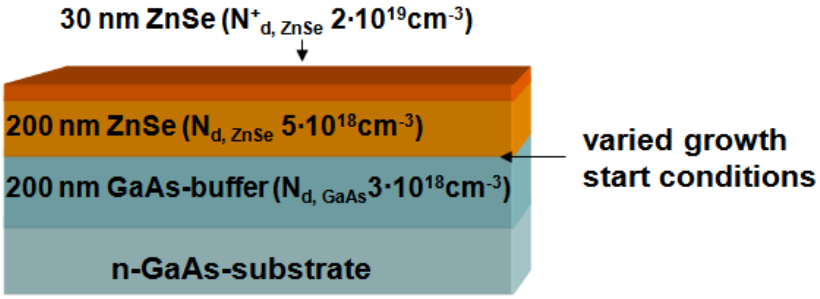

Figure 5.1: Schematic layout of the ZnSe/GaAs(001) sample series employed for the ZnSe-growth start influence on the electrical properties.

The sample layout is depicted in 5.1, it consists of an epiready n-doped GaAs-substrate(001) (N_d =1-5·10^{18} cm^{-3}) which was overgrown with a 200 nm thick GaAs-buffer layer (N_d =3·10^{18} cm^{-3}). The growth start conditions for the n-ZnSe layer was varied by a predeposition of Zn or Se. For Se-predeposition the amount of Se was additionally stepwise increased by the time (7 s, 11 s and 15 s) the GaAs surface was exposed to the Se flux. Afterwards a 200 nm n-ZnSe layer (N_d =5·10^{18} cm^{-3}) and a 30 nm n$^+$-ZnSe (N_d =2·10^{19} cm^{-3}) cap layer were grown. All samples are pseudomorphic, as confirmed by HRXRD. In an additional sample, the Zn-predeposition was followed by a ZnSe growth start in atomic layer epitaxy (ALE) mode. However this sample did not show the excellent crystalline quality as the samples grown by the conventional MBE process and thus it is not included in the optical experiments. The detailed growth parameters and the detailed description of the experimental aspects of the various analysis methods can be found in (FBM$^+$10).

5.2 Electrical Properties

The relevance of the growth start procedure for the electronic properties is illustrated in Fig. 5.2, showing the electrical transport characteristics across the interface, obtained from current vs. voltage (I-V) experiments (FBM$^+$10).

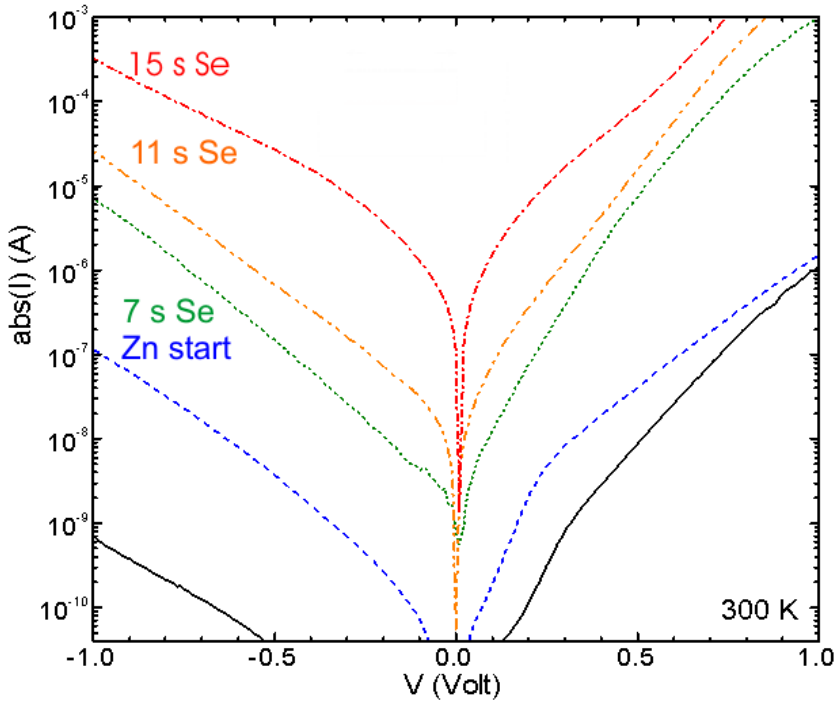

Figure 5.2: 300K current vs. voltage characteristics for different growth start procedures of the n-ZnSe on n-GaAs (adapted from (FBM$^+$10)).

There are two remarkable aspects within the sample series:
- The asymmetric curve shapes with respect to the bias voltage polarity immediately reveal that a potential barrier at the ZnSe/GaAs interface is limiting the transport. Forward-biased diode characteristics occurs for a positive potential on the GaAs-side. This confirms the positive offset of the ZnSe conduction band with respect to GaAs, as expected for type-I band alignment, because the ZnSe band gap value is about twice the GaAs one. The asymmetry is less pronounced for increasing Se-predeposition. The potential barrier height was addressed by temperature dependent I-V measurements. They reveal that there is a substantial reduction of the potential barrier height Φ_b by the Se-pre-deposition growth start, see tab. 5.1. The Φ_b value is reduced from 550 meV for the Zn-rich growth start down to 73 meV for a 15 s Se-pre-deposition.

- The second difference is the striking current increase, which is high as about five orders of magnitude, within the sample series. The highest current is recorded for the longest Se-predeposition time. However, even for the sample with a Se-predeposition time of 15 s, the resistivity is still orders of magnitudes higher than expected by the intended

growthstart	Φ_b (meV)
Zn-start	550
7s Se	300
11s Se	280
15s Se	73

Table 5.1: Potential barrier Φ_b derived from temperature-dependent I-V measurements at the ZnSe/GaAs interface for different growth start conditions (from(FBM+10)).

doping density and the size of the employed mesas for the I-V characterization.

In order to check, whether this current increase within the series is purely interface-related and, moreover, to identify the reason for the remaining considerable resistance, the possibility of sample-to-sample doping level differences of the ZnSe- and GaAs-layer, was checked by two independent techniques:
(i) As a non-destructive carrier-density analysis, far-infrared reflectance (FIR) spectroscopy was applied within this work.
(ii) In-depth carrier density profiles were derived from capacitance-voltage profiling (etch-CV) (FBM+10).

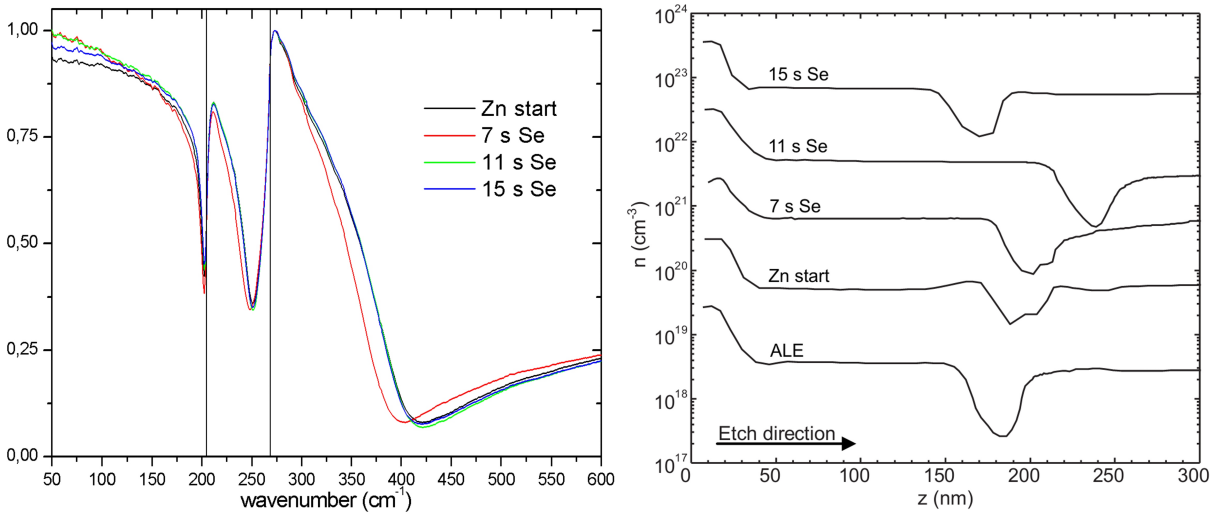

Figure 5.3: FIR reflectance of the growth start samples series (left hand side) and in-depth carrier density profiles derived by etch-CV (right hand side, adapted from (FBM+10)).

Their results are comprised in fig. 5.3. The IR spectra show that all samples nearly identically have a high reflectance level in the frequency range between 0 and 300 cm^{-1}, only interrupted by dips directly below the TO phonon frequencies of ZnSe and GaAs. Since this high reflectance is due to screening of the FIR electric field by free carriers, it can safely be concluded that all samples have about the same carrier concentration. This finding is confirmed by the etch-CV results. Apart from the highly doped capped ZnSe layer, the carrier density remains constant and approximately at the projected level

intended by the doping in the ZnSe/GaAs layers. However for all samples a depletion layer with an overall extent of about 50 ± 10 nm occurs, which is essentially constant for all growth start procedures. Within the accuracy of the etching depth scale, the in-depth location of this layer corresponds to the interface region. However, an allocation of contributions from the ZnSe-side and /or the GaAs side to the depletion layer is definitely impossible due to the large error bar of the etching depth scale.

These two findings from FIR and etch-CV confirm the exclusive relevance of the interface region for the electrical characteristics. For a better understanding of the strong growth-start-induced potential barrier variation together with the constant electron deficit, the knowledge of the individual depletion layer widths w_d at both sides of the interface, $w_{d,ZnSe}$ and $w_{d,GaAs}$, is highly desirable. This goal was addressed by Raman spectroscopy in the following.

5.3 LO-Phonon and Plasmon-LO-Phonon modes

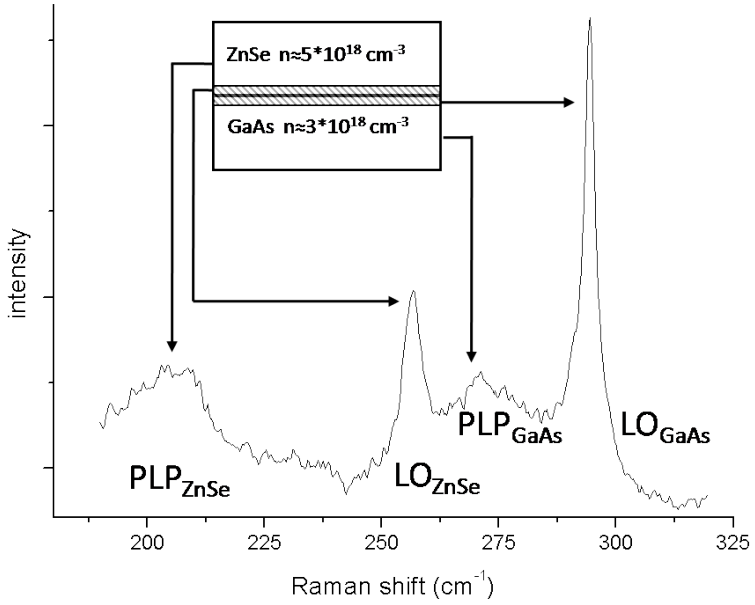

Figure 5.4: Raman spectrum of ZnSe/GaAs(001)with the longitudinal optical (LO) phonon and plasmon-longitudinal-phonon (PLP) contributions of the different layers of the sample structure.

The principle of the detection of the individual depletion layers on the ZnSe- and the GaAs side by Raman spectroscopy is illustrated in Fig. 5.4. In the frequency range of the ZnSe and GaAs lattice vibrations, the essential Raman peaks originate from the longitudinal optical (LO) phonon modes (LO_{ZnSe} = 256 cm^{-1}, LO_{GaAs} = 294 cm^{-1}) and from the coupled plasmon-LO-phonon modes (PLP), located at PLP_{ZnSe} = 207 cm^{-1}

and PLP_{GaAs} = 272 cm^{-1}. These peaks allow the determination of the individual depletion layer widths $w_{d,ZnSe}$ and $w_{d,GaAs}$ because only these depletion layers give rise to the phonon modes LO_{ZnSe} and LO_{GaAs}, respectively. In the bulk-like doped ZnSe epilayer and in the bulk-like doped GaAs behind the hetero-interface, coupled plasmon-LO-phonon modes PLP_{ZnSe} and PLP_{GaAs} arise below the LO frequency, as discussed in section 3.3. Their downshifts with respect to the LO frequency originate from a partial screening of the restoring forces of the polar LO vibrations by the free carriers (CG82). Additionally, plasmon-like upshifted coupled PLP modes occur. However, the latter are not subject of this analysis, because already the downshifted PLP modes give sufficient information for an unambiguous analysis of the depletion at boths sides of the interface. For the quantitative analysis, calibration procedures are required in order to take into account the consequences of the material-dependent Raman scattering efficiencies and possible signal attenuation by light absorption in case of finite penetration depth. In this regard, the transparent ZnSe and the opaque GaAs show complementary optical behaviour. Therefore the depletion layer thicknesses $w_{d,ZnSe}$ and $w_{d,GaAs}$ are derived separately along different quantitative procedures, and the Raman-experimental details, such as e.g. laser wavelength, are optimized for each of them individually, as described in the following sections. Common for the measurements are the sample temperature which was kept at liquid-nitrogen temperature in a cold-finger cryostat and the scattering configuration: 001(010,100)00-1 (Porto notation), thus only allowing the Raman signal from deformation potential scattering (details in section 2.3).

5.3.1 Raman analysis of the ZnSe-side of the interface

In the ZnSe layer, the LO-phonon Raman intensity is directly proportional to $w_{d,ZnSe}$, because in this transparent material (E_g = 2.8 eV at T = 80 K) no light attenuation has to be considered. The LO scattering efficiency was obtained from calibration with an undoped ZnSe layer of known thickness (d = 109 nm), using the same laser line (477 nm) and the same experimental conditions as for the ZnSe/GaAs (input laser power, Raman collection optics aperture, monochromator slit widths etc.). An LO_{ZnSe} contribution from the surface depletion layer is negligible in the investigated sample series. This layer is extremely thin due to the high doping level of the 30 nm n^+-ZnSe top contact layer with $N_{d,ZnSe} = 2{\cdot}10^{19}$ cm^{-3}.

Thus by the direct comparison of the LO intensity from the undoped ZnSe sample with well-know thickness and the LO intensity from the doped ZnSe epilayer with a carrier-free depletion layer, the thickness of this depletion layer is derived. As the samples are cooled for the optical experiments, care has to be taken when comparing absolute intensities as the focus can migrate during prolonged measuring time due to i.e. the change in the liquid nitrogen level in the coldfinger cryostat. All efforts were undertaken to keep the measuring time as short as possible to minimize this effect. This also implies the choice of the light polarization direction. The grating monochromator which was employed here has in the blue spectral range by far the highest sensitivity for vertical light polarization. Therefore the incident photon polarization was turned to horizontal polarization as the

scattered photons are then in vertical polarization because of the off-diagonal scattering Raman tensor characteristics, resulting from the symmetry selection rules, described in 2.3. However, this approach also implies a Raman scattering contribution from TO phonons. This contribution is forbidden for strict (001) backscattering geometry (i.e. perfect normal incidence and zero aperture angle). It appears here, because the employed quasi-backscattering geometry (slightly oblique incidence and finite aperture angle) gives rise to a small partial projection onto the (110) backscattering geometry, in which Raman scattering from the TO phonon is allowed for the polarization employed here. However, this scattering contribution is not interfering with the evaluation as the position and the FWHM of the TO-phonon signal are known and thus it can (simply) be subtracted in the spectrum. (Additionally, for this evaluation of the depletion layer thickness in the ZnSe, the only relevant scattering intensity is from LO-phonons and they are unperturbed either from TO signals from the ZnSe and/or the GaAs.)
For excitation the 477 nm laserline was chosen in order to take into account a possible bandgap variation due to the doping. Therefore the excitation energy should be off resonance to enable a comparison of the scattering intensities of the undoped reference sample with the doped sample series as the scattering efficiency is very sensitive when the excitation energy is near an electronic transition, see equation 2.3.
The Raman spectra of the ZnSe reference and the sample with 11 s Se predeposition are shown in fig. 5.5. Also plotted are the fits of the LO_{ZnSe} and the PLP and TO signal of the GaAs. As stated above the quantitative evaluation of the depletion layer thickness $w_{d,ZnSe}$ under these experimental conditions is done by comparison of the scattering intensities of the LO_{ZnSe} signal of the reference and the sample series.

growthstart	$w_{D,ZnSe}$ (nm)
Zn-start	20
7s Se	50
11s Se	41
15s Se	37

Table 5.2: Depletion layer thickness on the ZnSe-side of the ZnSe/GaAs interface for different growthstart conditions

The depletion layer thicknesses in the ZnSe layer for the different growth start conditions are listed in tab. 5.2. For the Se-growth start the depletion layer thickness decreases from 50 nm (7 s Se) down to 37 nm (15 s Se). However for the Zn-growth start it only amounts to 20 nm. Thus, we observe a significant enhancement due to Se predeposition but only a limited dependence on the quantitative amount of predeposited Se.

5.3.2 Raman analysis of the GaAs-side of the interface

In contrast to the depletion layer thickness evaluation of the ZnSe, for the GaAs-side analysis of the depletion layer light attenuation must be considered as the excitation energies

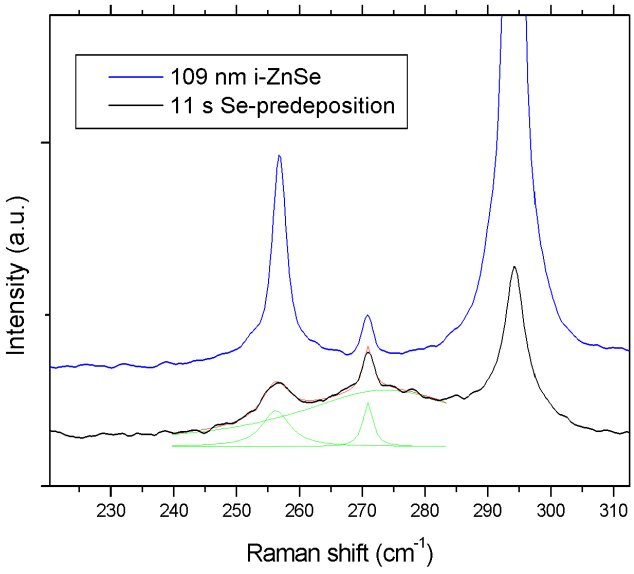

Figure 5.5: Comparison of the 477 nm @ 80 K Raman spectra of the intrinsic ZnSe layer and from the sample with a 11 s Se predeposition before ZnSe-growth. The intensity of the ZnSe LO-phonon signal directly reflects the depletion layer width $w_{d,ZnSe}$ when compared with the intensity of the LO-phonon from the reference sample with known ZnSe thickness of 109 nm. Additionally the fits for the ZnSe LO-phonon, the GaAs TO-phonon, and the GaAs PLP mode are shown in green.

are all above the bandgap of the GaAs of 1.4 eV. In order to guarantee a sufficient penetration depth, the 514 nm Ar ion laserline was used for excitation. This laserline allows an information depth in the GaAs of around 70 nm. Following the method described in detail in (JG93) the intensity ratio I_{LO}/I_{PLP} is considered in order to take appropriately into account the light attenuation influence on the analysis of the depletion layer thickness of the GaAs-side of the interface. The principle of this evaluation can be briefly described by the determination of the intensity ratio of I_{LO}/I_{PLP} of a sample with known depletion layer thickness. This intensity ratio is then the gauge for the depletion layer thickness and thus allows the derivation of the scattering intensity ratio vs. depletion layer thickness. For the calibration of the I_{LO}/I_{PLP} ratio with the depletion layer thickness a bulk doped epiready GaAs (001) substrate served as a reference sample. For uncovered GaAs the surface Fermi level is midgap pinned and thus the surface potential amounts to $V_{bb} = 0.7$ eV (Her96). This surface potential leads to a depletion layer at the surface (see section 3.5). For the calculation of its thickness (ref. 3.14) the knowledge of the doping level N_D is mandatory. This was addressed by an IR reflectance measurement of the epiready sub-

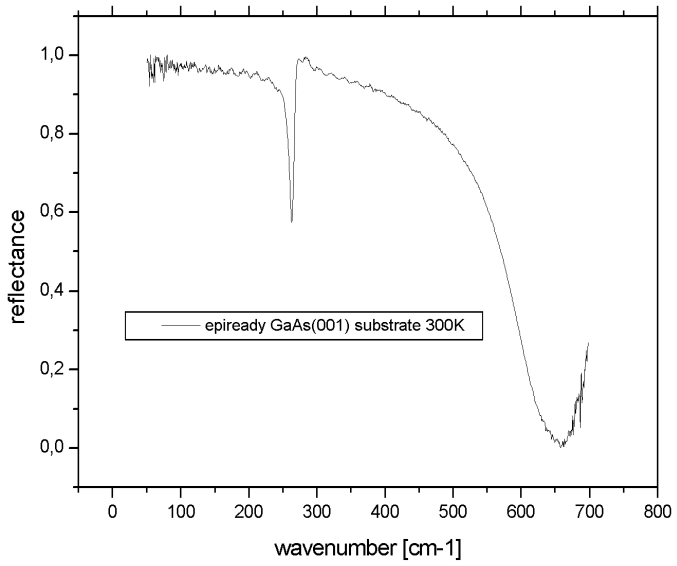

Figure 5.6: FIR reflectance spectrum of the epiready GaAs(001) substrate at 300 K. The reflectance decline at 597 cm^{-1} due to the plasma frequency of the free carriers directly reflects the actual doping density of the substrate of N_D of $2.9{\cdot}10^{18}$ cm^{-3}.

strate, shown in fig. 5.6. With the program Reffit the course of the reflectance was fitted, yielding a plasma frequency of 597 cm^{-1} which equals to a doping level N_D of $2.9{\cdot}10^{18}$ cm^{-3}. Herewith the surface depletion layer of the reference sample was calculated to 18.2 nm. For this sample the experimentally obtained intensity ratio for excitation wavelength $\lambda = 514$ nm amounts to $I_{LO}/I_{PLP} = 0.225$. This value comprises the overall effect of the scattering efficiency ratio of LO and PLP and the absorption-induced light attenuation

for this excitation wavelength. In the following, it will be used for the quantitative evaluation of the GaAs intensity ratios I_{LO}/I_{PLP} of the ZnSe/GaAs series in terms of the GaAs depletion layer widths.

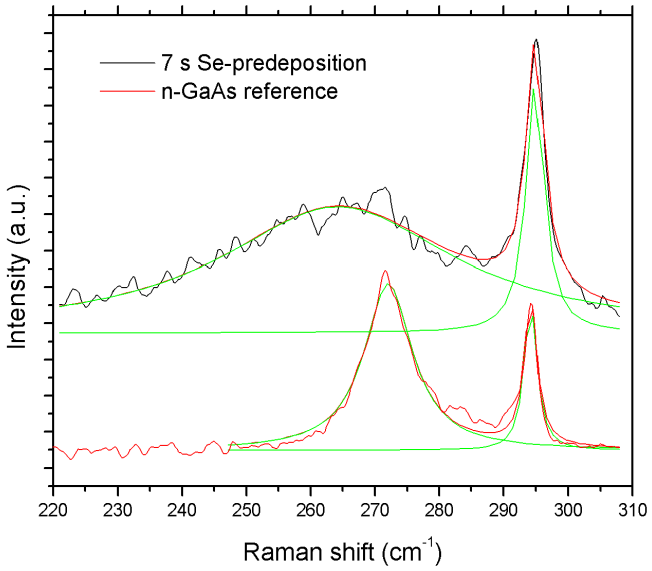

Figure 5.7: 514 nm @ 80 K Raman spectra and fits of the LO-phonon and PLP-mode of the GaAs for the sample with 7 s Se predeposition and the epiready GaAs(001) substrate reference.

Therefore, the comparison of $I_{LO,GaAs}/I_{PLP,GaAs}$ of the various growth-start samples with this reference value yields their depletion widths $w_{d,GaAs}$. Fig. 5.7 shows an exemplary Raman spectrum of the sample with t_{Se}=7 s Se-predeposition and the GaAs reference sample. Its GaAs-peak intensity ratio is $I_{LO,GaAs}/I_{PLP,GaAs} = 0.319$, yielding the GaAs depletion width $w_{d,GaAs} = 26$ nm.
The depletion layer thicknesses of the remaining samples are comprised in tab. 5.3.

growthstart	$w_{D,GaAs}$ (nm)
Zn-start	25.8
7s Se	15
11s Se	16.3
15s Se	16.1

Table 5.3: Depletion layer thickness on the GaAs-side of the ZnSe/GaAs interface for the different ZnSe growthstart conditions

Conclusions

The corresponding depletion-layer values are listed in tab. 5.2 and 5.3. Thus, throughout the sample series the determination of the individual depletion layer thicknesses $w_{d,ZnSe}$ and $w_{d,GaAs}$ by Raman spectroscopy reveals a partial shift of the depleted interface region, which is for the Zn-start sample symmetrically shared by the ZnSe and the GaAs, towards a dominating contribution on the ZnSe side for the samples with Se pre-deposition. A modeling of possible interface configurations according to different scenarios and the resulting depth profiles of the conduction band energy and electron density are presented in ref. (FBM$^+$10). In the modeling procedure not only the band offset and the interface state density, but also atomic interdiffusion and segregation, as well as the possible occurrence of continuous in-depth doping profiles are considered. As the quintessence of this procedure the following effects of the Se-predeposition were obtained:
(i) the reduction of the conduction band offset to a value below 0.1 eV, i.e. modified interface dipole moments,
(ii) an interface-state density below $2{\cdot}10^{12}$ cm^{-2},
(iii) a modified carrier-density profile, that may be explained by a change of the interdiffusion of atoms across the interface, which may act as compensating acceptors in the ZnSe and the GaAs interface regions.
In summary, the impact of the growth start procedure on the electronic properties of MBE-grown n-type ZnSe/GaAs(001) hetero-interfaces was studied, focusing on the conduction band barrier and the depletion layers w_d on both sides of the interface. This study reveals that Se pre-deposition drastically reduces conduction band barrier from 550 meV for Zn-rich start to 73 meV for the highest Se pre-deposition, indicating strongly modified interface dipole moments. Raman spectroscopy analysis of the depletion layer widths w_d shows upon Se pre-deposition a reduction of $w_{d,GaAs}$ and an enhancement of $w_{d,ZnSe}$. This shift may be explained in terms of a changed interdiffusion of atoms, which act as compensating acceptors in the n-doped layers.

5.4 Photoluminescence results

Apart from the Raman investigation also PL spectra from the sample series were recorded to gain additional informations by their luminescence properties. As an exemplary spec-

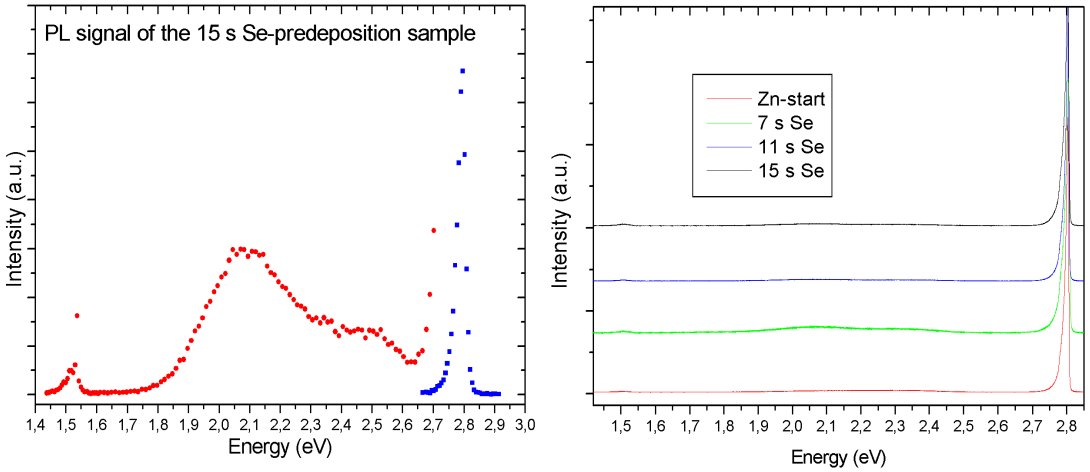

Figure 5.8: Left side: PL spectrum for $\lambda_i = 405$ nm @ T = 80 K of the 15 s Se predeposition, the red dots show the PL signal from the sample in the energy range from the GaAs and the broad luminescence peaks related to zinc-vacancies, the signal indicated by the blue dots is from the ZnSe bandgap emission (the signal intensity was reduced by a factor of 40 to enable comparison). Right side: Waterfall plot of the PL spectra of all samples with the different applied growthstart conditions.

trum the PL from the sample series with 15 s Se-predeposition is shown in fig. 5.8. The spectrum was taken at a sample temperature of 80 K and by excitation with 405 nm laserlight. Besides the strong bandgap related signal of the ZnSe at 2.8 eV (indicated by the blue dots) and the GaAs PL signal at 1.5 eV, there are two very broad peaks centered at an energy of 2.0...2.1 eV and 2.4...2.5 eV. The origin of those two peaks will be derived individually in the next two passages and the difference in the luminescence intensity within the sample series will be analyzed in terms of the changed growth start conditions. By the energy position it is intuitive that the origin of this luminescence lays in the ZnSe or in the interface of the heterosystem. For the evaluations, the peaks are assigned along the lines of a review article by Gutowski et al (GPK90) on the luminescence properties of ZnSe.

5.4.1 Luminescence band at 2.4 eV

In literature there are two possible explanations for the luminescence band around 2.4 eV. The common explanation for the origin of this band is the unintended incorporation of Copper-atoms into the ZnSe during the manufacturing process of the layer. Corresponding to its energy position this luminescence is thus denoted Cu-green emission. However, even if this Cu-incorporation is in principle possible it is still highly unlikely for the samples investigated here. The only parts in the MBE setup with copper are the seals

at the CF-flanges. As those flanges are not at an elevated temperature, a desorption and incorporation of copper can thus be virtually excluded. Additionally, for the other samples with a ZnSe layer characterized within this work, the PL characterization never revealed any signal intensities in this spectral range. Therefore the second possible explanation for the luminescence origin seems way more reasonable. This luminescence can also result from an exciton which binds to a zinc vacancy V_{Zn}. This hypothesis is backed by two important experimental findings:
- The luminescence intensity of this peak strongly depends on the excitation energy as it vanishes for excitation energies below the bandgap of ZnSe. This behaviour is shown in fig. 5.9. In principle an exciton creation at a Zn vacancy is possible for excitation energies above 2.4 eV but in this case the incoming photon must hit the V_{Zn} directly and so the conversion efficiency is low. In the case of excitation above the bandgap of the ZnSe the luminescence intensity is way higher because then the Zinc-vacancies can trap the free excitons in their vicinity and thus are an efficient recombination channel for the excitons.

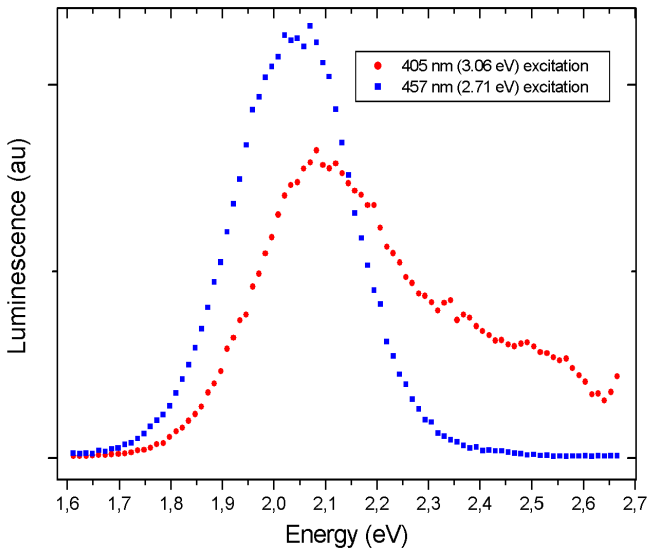

Figure 5.9: 80 K luminescence of the 15 s Se predeposition sample for two different excitation energies (above and below the bandgap of ZnSe).

- The second aspect which makes the exciton recombination at a V_{Zn} even more likely is the fact that a V_{Zn} acts as an acceptor. For high doping of a semiconductor, self-compensation is energetically favorable (CHA94). Thus the formation of V_{Zn} acceptor like states is a possibility for self-compensation. This also explains why the intrinsic samples in this work did not show this luminescence.

5.4.2 Luminescence band at 2.0 eV

The luminescence band around 2 eV is often referred to as the self-activated (SA) emission of ZnSe. However this description is not very precise as the emissions in this energy range are often called SA without a possible explanation of the origin. One source is the luminescence from a Gallium atom at a Zn-place accompanied by a V_{Zn}-neighbour. This molecule-like complex also acts as an acceptor and thus is also a possible way for the self-compensation of the doped ZnSe. The excitation energy dependence of this band is clearly different from the 2.4 eV peak, already shown in fig. 5.9. The 2.0 eV luminescence intensity is below the perception threshold for excitation wavelengths longer than 496 nm (2.50 eV). The different absorption behaviour for sub bandgap excitation may be attributed to the spatial extend of the complex as compared to the strongly localized, essentially Frenkel-like, exciton at the Zn vacancy.

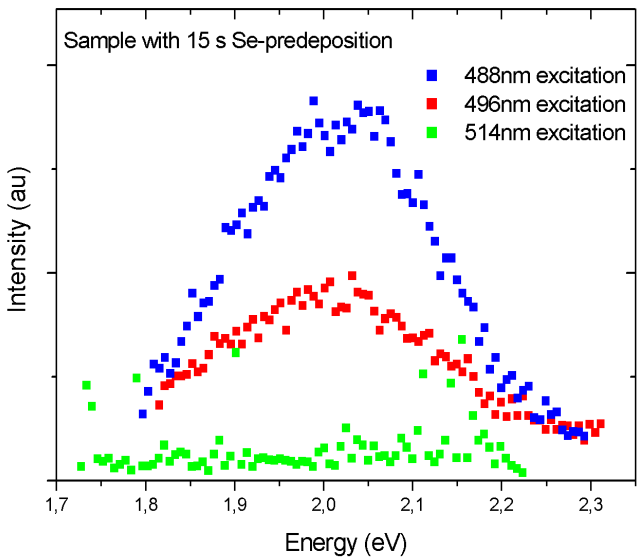

Figure 5.10: 80 K PL spectra for different excitation energies (2.54 eV, 2.50 and 2.41 eV) of the sample with 15 s Se predeposition. For excitation line λ_i= 514nm (2.41 eV), the PL signal at 2.0 eV is below the perception limit.

5.4.3 Influence of the growth start conditions on the luminescence bands

The self-compensation of a highly n-doped ZnSe leads to the formation of Zn-vacancies. This is an intrinsic mechanism for doped ZnSe. However the additional intermixture with Ga, leading to the SA-emission, is a diffusion process which can be affected by the growth start conditions. When comparing the intensity ratio between Ga_{Zn}-V_{Zn} and V_{Zn} emission, a trend within the sample series is ascertainable, see tab. 5.4.

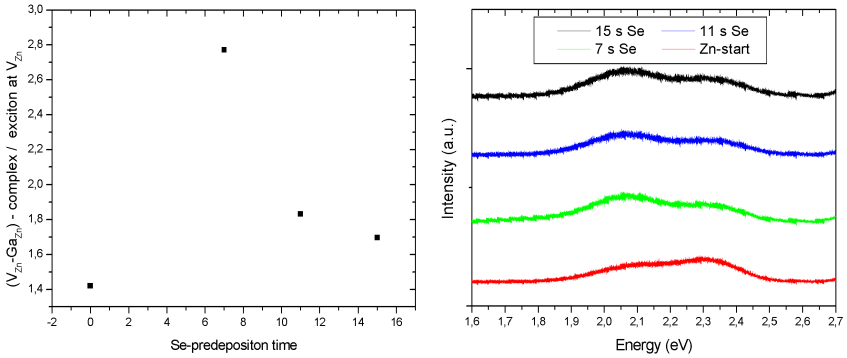

Figure 5.11: Intensity ratio of Ga_{Zn}-V_{Zn}-complex to the exciton at a V_{Zn} emission for the different Se-predeposition times derived by the PL-measurements at 1.2K and UV excitation. The employed spectra for this evaluation are shown on the right hand side.

growthstart	Zn	7 s Se	11 s Se	15 s Se
$(Ga_{Zn}$-$V_{Zn})/V_{Zn}$	1.42	2.77	1.83	1.70

Table 5.4: Ratio of Ga_{Zn}-V_{Zn}-complex to the exciton at a V_{Zn} emission for the different Se-predeposition times, derived by the PL-measurements at 1.2K and UV excitation.

For the Se predeposition the ratio is decreasing with increasing Se-predeposition time indicating a reduced diffusion of Ga-atoms in the ZnSe-layer. However the smallest ratio is derived for the Zn-start of the ZnSe layer. This result reproduces the course of the depletion layer thickness gained for the ZnSe. Therefore it could be assumed that the SA-signal is originating from near the interface or is even constricted to the depletion layer thickness in the ZnSe. For a complete analysis by the PL signal of sample series the energy range below the bandgap of GaAs would be necessary. This is however not feasible in the employed setup due to implemented detector and gratings.

Chapter 6

Summary

The subject of this thesis was the analysis of II-VI quantum dots (QD) and II-VI/III-V-hetero-interfaces, grown by molecular beam epitaxy (MBE). Specifically, the QD studies were performed on CdSe QDs, grown on ZnSe(100), while ZnSe/GaAs(100) was employed as a prototype hetero-interface. For the QDs, the aspects of composition, intermixing and residual strain were in the focus, while the ZnSe/GaAs(100) interface the electron depletion layers were the object of study. In both cases the impact of various MBE growth procedures was analyzed. The main experimental technique for both systems was Raman spectroscopy. In the QD studies, the elementary excitations in the Raman spectra were phonons, while for the hetero-interface analysis besides LO-phonons also coupled plasmon-LO-Phonon modes were studied.

The CdSe QD studies comprised several series of epitaxially overgrown QDs with various thicknesses and from different growth procedures. Moreover, uncapped QDs were investigated under UHV conditions. Notably, all the overgrown QDs gave a particularly high photoluminescence emission, covering the range from blue (2,68 eV) to green/yellow (2,26 eV) with increasing CdSe thickness up to 5 ML. Its high spectral width is explained in terms of a QD size and composition distribution. The influence of the various growth technique on the PL spectrum turns out to be low, apart from the samples from the amorphous Tellurium procedure. Here distinct Te-derived contributions occur due to its incorporation in the ZnSe as isoelectronic centers. The LO-phonon Raman peak positions follow a universal trend: a clear redshift of the CdSe-QD-derived mode with increasing coverage and a less pronounced redshift of the ZnSe LO phonon are observed. The evaluation of the QD phonon frequency in terms of the (Cd,Zn)Se composition yields for the 3 ML samples a Cd-content between 21% and 37%, while for 5 ML a maximum Cd percentage of 45% is determined. The above mentioned small redshift of the LO ZnSe phonon reveals the incorporation of Cd from the CdSe layer, leading to ternary (Zn,Cd)Se regions with a Cd content up to 15%. For the uncapped samples Raman spectroscopy turned out to be the only optical technique for QD analysis, because the photoluminescence from excitonic recombination is quenched by nonradiative channels at the surface. A morphology change due to local strain relief during annealing is reflected in a step-like CdSe phonon frequency redshift for 200 - 230°C annealing temperature. This process is

interpreted as the signature of QD formation.

The second system of interest was the n-ZnSe/n-GaAs interface as an exemplary case of II-VI/III-V heterovalent interfaces. The central question was the impact of various ZnSe growth start procedures with predeposition of different amounts of Zn or Se in the monolayer range. In the analysis, special reference was given to the interface-induced depletion layers at both sides of the interface. Their individual identification and the determination of their widths $w_{d,ZnSe}$ and $w_{d,GaAs}$ were successfully performed by Raman scattering from the LO phonons and the coupled Plasmon-LO-Phonon modes of ZnSe and GaAs, respectively.

Throughout the sample series the total depletion width turned out to be nearly independent of the growth start procedure. It amounts up to 65 nm. However, the Raman results reveal a partial shift of the depleted interface region, which is for the Zn-start sample symmetrically shared by the ZnSe and the GaAs, towards a dominating contribution on the ZnSe side in the range of 37 - 50 nm for the samples with Se pre-deposition.

This behaviour fits in the total scenario of interface formation, which was established with additional consideration of electrical transport properties (FBM$^+$10). They show a drastic reduction of the conduction band barrier from 550 meV for Zn-rich start to 73 meV for the highest Se pre-deposition, due to modified interface dipole moments. The depletion layer shift may be explained in terms of a changed interdiffusion of atoms, which act as compensating acceptors in the n-doped layers.

Additional information about the atomic diffusion was obtained by photoluminescence from localized states. Two types of states were considered: (i) Zinc-vacancies V_{Zn}, connected with the intrinsic trend towards self-compensation in heavily n-doped ZnSe, and (ii) complexes of V_{Zn} with Ga_{Zn} (Ga atom on Zn-site). The PL intensity results are explained in terms of a reduced Ga-diffusion into the ZnSe with increasing Se predeposition.

Chapter 7

Zusammenfassung

Das Thema dieser Dissertation war die Analyse von II-VI Quantenpunkten (QP) und II-VI/III-V Heterogrenzschichten die mittels Molekularstrahlepitaxie (MBE) hergestellt wurden. Als Materialsysteme für die Untersuchung wurden QP aus CdSe auf bzw. in ZnSe(100) verwendet, während ZnSe/GaAs(100) für die Grenzflächeuntersuchungen zum Einsatz kam. Bei den QP lag der Augenmerk auf der Komposition, der Durchmischung und der Restverspannung, wohingegen bei der ZnSe/GaAs Grenzfläche die elektronischen Eigenschaften, insbesondere der Verarmungszonen, bestimmt wurden. In beiden Fällen wurde der Einfluß des Herstellungsprozesses auf die optischen Eigenschaften untersucht. Als experimentelle Untersuchungsmethode für beide Analysen kam hauptsächlich Ramanspektroskopie zum Einsatz. Für die QP-Untersuchungen wurden Phononen als Elementaranregung vermessen während die Eigenschaften der Heterogrenzfläche durch Phononen und auch gekoppelte Plasmon-LO-Phononen bestimmt wurden.

Die CdSe QP-Studien umfassten mehrere Probenserien von epitaktisch überwachsenen QP mit verschiedenen Dicken, die nach verschiedenen Prozeduren gewachsen wurden. Zusätzlich wurden ungecappte QP im Ultrahochvakuum untersucht. Erwähnenswert ist hierbei die ausserordentlich hohe Intensität der Photolumineszenz (PL) der überwachsenen QP, die vom blauen Spektralbereich (2.68 eV) mit steigender nomineller CdSe-Dicke bis in den grün/gelben Spektralbereich (2.26 eV bei 5 Monolagen (ML) CdSe-Bedeckung) verschiebt. Die Breite der PL-Emission erklärt sich hierbei aufgrund der QP-Größen- und Kompositions-Verteilung, wobei der Einfluß der verschiedenen Herstellungsprozeduren auf das PL-Spektrum eher gering ist. Die Ausnahme bildet hierbei die Probenserie die mittels einer amorphen Tellur Opferschicht hergestellt wurde. Die zusätzlichen PL-Beiträge im Spektrum konnten durch den isoelektronischen Einbau von Telluratomen in die ZnSe-Schicht erklärt werden.

Die Peakposition der LO-Phonon der QP folgte einem einheitlichen Trend: Mit steigender CdSe-Bedeckung zeigten die QP-Phononen eine signifikante Rotverschiebung, während diese Verschiebung für die ZnSe-LO-Phononen deutlich geringer war. Die Auswertung der Phononenfrequenz im Hinblick auf die Komposition der (Zn,Cd)Se-QP ergibt für 3 ML Bedeckung eine Cd-Konzentration im Bereich zwischen 21% und 37%, die Cd-Konzentration erreicht einen Höchstwert von 45% für 5 ML CdSe-Bedeckung. Die erwähnte leichte

Rotverschiebung des ZnSe-LO-Phonons ist die Folge des Einbaus von Cd in die ZnSe-Schicht, diese Durchmischung ergibt Bereiche im ZnSe mit einer Cd-Konzentration bis zu 15%. Ramanspektroskopie erwies sich als einzige optische Untersuchungsmethode bei den ungecappten Proben, da die Photolumineszenz-Emission durch die nicht-strahlenden Rekombinationskanäle an der Oberfläche unterdrückt wird. Eine Morphologie-Änderung durch den Abbau von Verspannung äußerte sich hierbei in einer stufenförmigen Rotverschiebung der CdSe-Phononen bei Temper-Temperaturen von 200-230°C.

Im zweiten Teil wurde die Grenzfläche von n-ZnSe/n-GaAs als beispielhafte II-VI/III-V heterovalente Grenzfläche untersucht. Die zentrale Fragestellung betraf hierbei den Einfluß des ZnSe-Wachstumsstarts auf die Verarmungszonen an der Grenzfläche. Hierzu wurde die ZnSe-Wachstumsstartbedingung durch die Abscheidung von Zn oder Se in verschiedenen Mengen im Monolagen-Bereich variiert. Die individuellen Verarmungszonenweiten auf beiden Seiten der Grenzfläche $w_{d,ZnSe}$ und $w_{d,GaAs}$ konnten durch Raman-Streuung an LO-Phononen und den gekoppelten Plasmon-LO-Phonon Moden bestimmt werden. Innerhalb der Probenserie zeigte sich daß die kombinierte Verarmungszonenweite (ca. 65 nm) nahezu unabhängig vom Wachstumsstart ist. Allerdings konnte durch die Raman-Messungen eine partielle Verschiebung des verarmten Bereiches, der für den Zn-Start symmetrisch zwischen ZnSe und GaAs aufgeteilt ist, in einen dominierenden Beitrag der ZnSe-Schicht (37 - 50 nm) für die Selen-Abscheidung nachgewiesen werden. Dieses Resultat bestätigt das Modell der Ausbildung der Grenzfläche, das aus zusätzlichen elektrischen Messungen gewonnen wurde (FBM$^+$10). Diese zeigen eine drastische Reduzierung des Leitungsbandbarriere, von 550 meV bei Zn-reichen Wachstumsstartbedingungen hinab zu 73 meV bei Se-Vorabscheidung, durch modifizierte Grenzflächendipolmomente. Die Verschiebung der ladungsträgerverarmten Schicht kann hierbei durch eine Änderung der Diffusion der Atome erklärt werden, die als kompensierende Akzeptoren in den n-dotierten Schichten wirken. Zusätzliche Information über die Diffusion der Atome konnte durch die Photolumineszenz von lokalisierten Zuständen gewonnen werden. Hierbei wurden zwei Zustände betrachtet: (i) Zink-Fehlstellen V_{Zn}, verursacht durch den intrinsischen Trend der selbst-Kompensation in hochdotierten n-ZnSe-Schichten, und (ii) Komplexe aus eine Zink-Fehlstelle V_{Zn} und einem Ga-Atom auf einem Zinkgitterplatz Ga_{Zn}. Die PL Intensitäten deuten auf eine reduzierte Ga-Diffusion in die ZnSe-Schicht mit steigender Selen-Vorabscheidung hin.

Bibliography

[ABV+07] L.P. Avakyants, P. Yu. Bokov, N.A. Volchkov, I.P. Kazakov, and A.V. Chervyakov. Determination of the Carrier Concentration in Doped n-GaAs Layers by Raman and Light Reflection Spectroscopies. *Optics and Spectroscopy*, 102:712–716, 2007. 3.3

[AS83] D.E. Aspnes and A.A. Studna. Dielectric functions and optical parameters of Si, Ge, GaP, GaAs, GaSb, InP, InAs, and InSb from 1.5 to 6.0 eV. *Phys. Rev. B*, 27(9):985–1009, 1983. 3.10

[ASR+89] R. G. Alonso, E.-K. Suh, A. K. Ramdas, N. Samarth, H. Luo, and J. K. Furdyna. Raman spectroscopy of two novel semiconductors and related superlattices: Cubic $Cd_{1-x}Mn_xSe$ and $Cd_{1-x}Zn_xSe$. *Phys. Rev. B*, 40:3720–3728, Aug 1989. 3.1, 3.2

[ATCP79] G. Abstreiter, R. Trommer, M. Cardona, and A. Pinczuk. COUPLED PLASMON-LO PHONON MODES AND LINDHARD-MERMIN DIELECTRIC FUNCTION OF n-GaAs. *Solid State Communications*, 30:703–707, 1979. 3.6

[BAM+91] Baganich, A. A., Mikla, V. I., Semak, D. G., Sokolov, A. P., and A. P. Shebanin. Raman Scattering in Amorphous Selenium Molecular Structure and Photoinduced Crystallization. *physica status solidi (b)*, 166(1):297–302, 1991. 4.6.2

[BBLG93] S. Bauer, H. Berger, P. Link, and W. Gebhardt. Raman studies of the growth mechanism of ZnSe/GaAs(001) heterostructures. *JAP*, 74(6):3916–3920, 1993. 5.1

[BDK92] W. BalA, M. Drozdowski, and M. Kozielski. Investigation of strain at the ZnSe/GaAs interface by photoluminescence and Raman scattering. *physica status solidi (a)*, 130(2):K195–K200, 1992. 5.1

[BGSY72] M. H. Brodsky, R. J. Gambino, J. E. Smith, and Y. Yacoby. The Raman Spectrum of Amorphous Tellurium. *physica status solidi (b)*, 52(2):609–614, 1972. 4.6.1

[Bra92] O. Brafman. Study of strained epitaxial layers by Raman techniques. *J. Vac. Sci. Technol. B*, 10(4):1730–1734, 1992. 5.1

[Bui10] Benjamin Buick. *High Spatial Resolution Raman Spectroscopy on Single Nanostructures*. PhD thesis, UNIVERSITÀ DEGLI STUDI DI ROMA "'Tor Vergata"', 2010. Dissertation. 3.3

[CABA99] L. Chu, M. Arzberger, G. Böhm, and G. Abstreiter. Influence of growth conditions on the photoluminescence of self-assembled InAs/GaAs quantum dots. *J. Appl. Phys.*, 85(4):2355 – 2362, 1999. 4.1

[CCS+08] M. C.-K. Cheung, A. N. Cartwright, I.R. Sellers, B.D. McCombe, and I. L. Kuskowsky. Time-resolved photoluminescence of type-II quantum dots and isoelectronic centers in Zn-Se-Te superlattice structures. *APL*, 92:032106, 2008. 4.5.1

[CG82] Eds. M. Cardona and G. Güntherodt. *Light Scattering in Solids II*, volume 50 of *Topics in Applied Physics*. Springer, 1982. 4.2.2, 5.3

[CG89] Eds. M. Cardona and G. Güntherodt. *Light Scattering in Solids V*, volume 66 of *Topics in Applied Physics*. Springer, 1989. 3.2

[CHA94] DJ CHADI. The problem of doping in ii-vi semiconductors. *Annu. Rev. Mater. Sci.*, 24:45–62, 1994. 5.4.1

[CLC+03] J. Camacho, I. Loa, A. Cantarero, K. Syassen, I. Hernández-Calderón, and L. González. Pressure dependence of optical phonons in ZnCdSe alloys. *physica status solidi (b)*, 235(2):432–436, 2003. 3.1

[CM68] I. F. Chang and S. S. Mitra. Application of a Modified Random-Element-Isodisplacement Model to Long-Wavelength Optic Phonons of Mixed Crystals. *Phys. Rev.*, 172:924–933, Aug 1968. 3.1

[DDA08] M.S. Dresselhaus, G. Dresselhaus, and Jorio A. *Group Theory*. Application to the Physics of Condensed Matter. Springer, Berlin, Heidelberg, 2008. 2.1

[DGH+92] K. Dhese, J. Goodwin, W. E. Hagston, J. E. Nicholls, J. J. Davies, B. Cockayne, and P. J. Wright. Interpretation of the temperature-dependent behaviour of the emission from isoelectronic tellurium centres in epitaxial $ZnSe_{1-x}Te_x$. *Semicond. Sci. Technol.*, 7:1210, 1992. 4.5.1

[DLRZ94] D. Drews, M. Langer, W. Richter, and D. R. T. Zahn. Monitoring Heteroepitaxial Growth of ZnSe on GaAs by Raman Spectroscopy. *physica status solidi (a)*, 145(2):491–496, 1994. 5.1

[DSZ+96] D. Drews, A. Schneider, D. R. T. Zahn, D. Wolffframm, and D. A. Evans. Raman monitoring of selenium decapping and subsequent antimony deposition on MBE-grown ZnSe(100). *Applied Surface Science*, 104-105:485 – 489, 1996. Proceedings of the Fifth International Conference on the Formation of Semiconductor Interfaces. 4.6, 4.6.2

[Esc07] Fabian Eschenbach. Einzel- und Mehrfachschichten von selbstorganisierten II-VI-Halbleiter Quantenpunkten. Master's thesis, Bayerische Julius-Maximilians-Univeristät Würzburg, 2007. 4.4.3, 4.20

[FBM+10] A. Frey, U. Bass, S. Mahapatra, C. Schumacher, J. Geurts, and K. Brunner. Band offsets and band bending at heterovalent semiconductor interfaces. *Phys. Rev. B*, 82:195318, Nov 2010. 5.1, 5.2, 5.2, 5.1, 5.2, 5.3, 5.3.2, 6, 7

[Fis72] R. Fischer. Absorption and Electroabsorption of Trigonal Selenium near the Fundamental Absorption Edge. *Phys. Rev. B*, 5:3087–3094, Apr 1972. 4.6.2

[FSE04] J. Frannson, I. Sandalov, and O. Eriksson. A perfect spin-filter quantum dot system. *J. Phys.: Condens. Matter*, 16:L249–L254, 2004. 1

[FTdM+91] H. H. Farrell, M. C. Tamargo, J. L. de Miguel, F. S. Turco, D. M. Hwang, and R. E. Nahory. "'designer"' interfaces in ii-vi/iii-v polar heteroepitaxy. *JAP*, 69(10):7021–7028, 1991. 5.1

[GAK+07] M. Ghali, R. Arians, T. Kümmell, G. Bacher, J. Wenisch, S. Mahapatra, and K. Brunner. Spin injection into a single self-assembled quantum dot in a p-i-n II-VI/III-V structure. *APL*, 90(9):093110, 2007. 5.1

[GI99] Tapas Ganguli and Alka Ingale. Raman and photoluminescence investigations of disorder in ZnSe films deposited on n-gaas. *Phys. Rev. B*, 60:11618–11623, Oct 1999. 5.1

[GKvdV+05] Y. Gu, Igor L. Kuskovsky, M. van der Voort, G. F. Neumark, X. Zhou, and M. C. Tamargo. Zn-Se-Te multilayers with submonolayer quantities of Te: Type-II quantum structures and isoelectronic centers. *Phys. Rev. B*, 71:045340, 2005. 4.5.1

[GM93] N. Grandjean and J. Massies. Epitaxial growth of highly strained $In_x xGa_{1-x}As$ on GaAs(001): the role of surface diffusion length. *Journal of Crystal Growth*, 134(1-2):51 – 62, 1993. 4.1

[GPK90] J. Gutowski, N. Presser, and G. Kudlek. Optical Properties of ZnSe Epilayers and Films. *physica status solidi (a)*, 120(1):11–59, 1990. 5.4

[GRuKE11] Simon Gustavsson, Clemens Rössler, and Thomas Ihn und Klaus Ensslin. Wenn einzelne Elektronen zählen. *Physik Journal*, 10(5):33–37, 2011. 1

[H.54] Fröhlich H. Electrons in lattice fields. *Advances in Physics*, 3:11:325–361, 1954. 2.4

[H.70] Lee B. H. Elastic constants of ZnTe and ZnSe between 77°-300°K. *J. Appl. Phys.*, 41:2984–2988, 1970. 4.6.2

[Har89] Walter A. Harrison. *Electronic Structure and the Properties of Solids*. Dover Publications, 1989. 4.1

[HCLLL+97] I. Hernández-Calderón, E. López-Luna, J. Luyo, M. Meléndez-Lira, O. de Melo, P. Díaz, L. Hernández, J. Fuentes, R. León, and H. Sitter. Investigation of the structural properties of MBE grown ZnSe/GaAs heterostructures. *Journal of Crystal Growth*, 175-176, Part 1(0):571 – 576, 1997. <ce:title>Molecular Beam Epitaxy 1996</ce:title>. 5.1

[Her96] Jan Hermans. *Optical Analysis of Structural and Electronic Properties of II-VI Heterostructures*. PhD thesis, RWTH Aachen, 1996. Dissertation. 3.2, 3.5, 4.2.2, 5.3.2

[IOY+08] M. Ii, M. Ohishi, M. Yoneta, Y. Sato, M. Shintani, K. Yoshino, and H. Saito. Growth and characterization of ZnSe/CdSe/ZnSe quantum dots fabricated by using an alternate molecular beam supplying method. *Applied Surface Science*, 254(23):7913 – 7917, 2008. <ce:title>9th International Conference on Atomically Controlled Surfaces, Interfaces and Nanostructures 2007 (ASCIN-9)</ce:title>. 4.1

[JG93] J. and Geurts. Analysis of band bending at iii–v semiconductor interfaces by raman spectroscopy. *Surface Science Reports*, 18(1-3):1 – 89, 1993. 5.3.2

[JKB+00] P. B. Joyce, T. J. Krzyzewski, G. R. Bell, T. S. Jones, S. Malik, D. Childs, and R. Murray. Effect of growth rate on the size, composition, and optical properties of InAs/GaAs quantum dots grown by molecular-beam epitaxy. *Phys. Rev. B*, 62:10891–10895, Oct 2000. 4.1

[JYH+03] T.S. Jeong, P.Y. Yu, K.J. Hong, T.S. Kim, C.J. Youn, Y.D. Choi, K.S. Lee, B. O, and M.Y. Yoon. Optical properties of the ZnSe/GaAs heteroepitaxial layers grown by hot wall epitaxy. *Journal of Crystal Growth*, 249(1-2):9 – 14, 2003. 5.1

[KAC+99] A. G. Kontos, E. Anastassakis, N. Chrysanthakopoulos, M. Calamiotou, and U. W. Pohl. Strain profiles in overcritical (001) znse/gaas heteroepitaxial layers. *JAP*, 86(1):412–417, 1999. 5.1

[Kam08] Prashant V. Kamat. Quantum Dot Solar Cells. Semiconductor Nanocrystals as Light Harvesters. *J. Phys. Chem. C*, 112:18737–18753, 2008. 1

[KCG+11] Danny Kim, Samuel G. Carter, Alex Greilich, Allan S. Bracker, and Daniel Gammon. Ultrafast optical control of entanglement between two quantum-dot spins. *Nature Physics*, 7:223–229, 2011. 1

[Kie] Tobias Kiessling. Low temperature pl of a-te qds. private communication. 4.5.1

[KJL+97] T.W Kim, M Jung, D.U Lee, E Oh, S.D Lee, H.D Jung, M.D Kim, J.R Kim, H.S Park, and J.Y Lee. Structural and optical properties of undoped and doped znse/gaas strained heterostructures. *Thin Solid Films*, 298(1-2):187 – 190, 1997. 5.1

[KJS+10] Jungtaek Kim, Puls J., Chen Y. S., Bacher G., and Henneberger F. Electron-nuclear spin control in charged semiconductor quantum dots by electrical currents through micro-coils. *APL*, 96:151908, 2010. 4.1

[KKP09] Svetlana V. Kilina, Dmitri S. Kilin, and Oleg V. Prezhdo. Breaking the Phonon Bottleneck in PbSe and CdSe Quantum Dots: Time-Domain Density Functional Theory of Charge Carrier Relaxation. *American Chemical Society Nano*, 3(1):93–99, 2009. 1

[Kli07] Claus Klingshirn. *Semiconductor Optics.* Springer, 2007. 3.4

[KML+00] I. Kegel, T. H. Metzger, A. Lorke, J. Peisl, J. Stangl, G. Bauer, J. M. Garcia, and P. M. Petroff. Nanometer-Scale Resolution of Strain and Interdiffusion in Self-Assembled InAs/GaAs Quantum Dots. *Phys. Rev. Lett.*, 85:1694–1697, Aug 2000. 4.1

[KN94] Alexander Kley and Jörg Neugebauer. Atomic and electronic structure of the GaAs/ZnSe(001) interface. *Phys. Rev. B*, 50:8616–8628, Sep 1994. 5.1

[LB99] Landolt and Börnstein. *Semiconductors, Complete Edition of Vols III/17, 22 and 41 on CD.* Springer, Berlin Heidelberg NewYork, 1999. B:II-VI and I-VI-Compounds; Semimagnetic Compounds. 2.4, 3.2, 4.3.2, 4.6.2

[Led11] N. N. Ledentsov. Quantum dot laser. *Semicond. Sci. Technol.*, 26:014001, 2011. 1

[LEEN+07] R. B. Laghumavarapu, M. El-Emawy, N. Nuntawong, A. Moscho, L. F. Lesterv, and D. L. Huffaker. Improved device performance of InAs/GaAs quantum dot solar cells with gaP strain compensation layers. *Appl. Phys. Lett.*, 91:243115, 2007. 1

[LKK+94] C. D. Lee, B. K. Kim, J. W. Kim, S. K. Chang, and S. H. Suh. Structural properties of ZnSe on GaAs grown by atomic layer epitaxy. *JAPI*, 76(2):928–931, 1994. 5.1

[LKS08] Stefan Legel, Jürgen König, and Gerd Schön. Generation and detection of a spin entanglement in nonequilibrium quantum dots. *New Journal of Physics*, 10:045016, 2008. 1

[LMT+67] G. Lucovsky, A. Mooradian, W. Taylor, G. B. Wright, and R. C. Keezer. Identification of the fundamental vibrational modes of trigonal, [alpha] - monoclinic and amorphous selenium. *Solid State Communications*, 5(2):113 – 117, 1967. 4.6.1, 4.6.2

[Lou63] R. Loudon. Theory of the first-order Raman effect in crystals. *Proc. R. Soc. Lond. A*, 275:218–232, 1963. 2.1

[LPP94] D. Leonard, K. Pond, and P. M. Petroff. Critical layer thickness for self-assembled InAs islands on GaAs. *Phys. Rev. B*, 50:11687–11692, Oct 1994. 4.1

[LSR+08] D. Litvinov, M. Schowalter, A. Rosenauer, B. Daniel, J. Fallert, W. Löffler, H. Kalt, and M. Hetterich. Determination of critical thickness for defect formation of CdSe/ZnSe heterostructures by transmission electron microscopy and photoluminescence spectroscopy. *physica status solidi (a)*, 205(12):2892–2897, 2008. 4.3, 4.1, 4.7

[LSSF98] W. S. Li, Z. X. Shen, D. Z. Shen, and X. W. Fan. Micro-Raman and photoluminescence investigation of $Zn_xCd_{1-x}Se$ thin film under high pressure. *J. Appl. Phys.*, 84:5198 – 5201, 1998. 3.1

[LV04] L.K. and Vodopyanov. Optical studies of ii–vi alloy lattice dynamics. *Journal of Alloys and Compounds*, 371(1-2):72 – 76, 2004. <ce:title>Solid Solutions of the II-VI Compounds-Growth, Characterization and Applications. Proceedings of the E-MRS 2002 Fall Meeting, Symposium G</ce:title>. 3.1

[Mah07] Suddhasatta Mahapatra. *Formation and properties of epitaxial CdSe/ZnSe quantum dots.* PhD thesis, Bayerische Julius-Maximilians-Universität Würzburg, 2007. Dissertation. 3.6, 4.2, 4.4.3, 4.22

[MBH+94] M. O. Möller, V. Beyersdorfer, D. Hommel, T. Behr, H. Heinke, T. Lippmann, and G. Landwehr. Structural characterization and interfacial studies of ZnSe based heterostructures on GaAs. *Journal of Crystal Growth*, 143(3-4):162 – 171, 1994. 4.6.2

[MHB+96] W. Meredith, G. Horsburgh, G.D. Brownlie, K.A. Prior, B.C. Cavenett, W. Rothwell, and A.J. Dann. Microprobe raman study of the variation of lo phonon frequency with the cd concentration in the ternary compound zn1 - xcdxse. *Journal of Crystal Growth*, 159(1-4):103 – 107, 1996. <ce:title>Proceedings of the seventh international conference on II-VI compouds and devices</ce:title>. 3.1

[MKA+07] S. Mahapatra, T. Kiessling, G. V. Astakhov, J. Renner, U. Bass, C. Bougerol, T. Schmidt, A. Bendounan, F. Schmitt, C. Schumacher, L. Worschech, W. Ossau, J. Geurts, L. W. Molenkamp, F. Reinert, A. Forchel, and K. Brunner. CdSe/ZnSe heteroepitaxy: Aspects of growth and self-organization of nanostructures. *phys. stat. sol. (c)*, 4(9):3129–3149, 2007. 4.4

[MYM+00] Kenzo Maehashi, Nobuhiro Yasui, Yasuhiro Murase, Akihiro Shikimi, and Hisao Nakashima. Formation of self-organized CdSe quantum dots on ZnSe(100) surfaces by molecular beam epitaxy. *Applied Surface Science*, 166(1-4):322 – 325, 2000. 4.1

[Noz02] A.J. Nozik. Quantum dot solar cells. *Pysica E*, 14:115–120, 2002. 1

[NRS81] U. Nowak, W. Richter, and G. Sachs. Lo-Phonon-Plasmon Dispersion in GaAs Hydrodynamical Theory and Experimental Results. *physica status solidi (b)*, 108(1):131–143, 1981. 3.3

[OSPC87] D. J. Olego, K. Shahzad, J. Petruzzello, and D. Cammack. Depth profiling of elastic strains in lattice-mismatched semiconductor heterostructures and strained-layer superlattices. *Phys. Rev. B*, 36:7674–7677, Nov 1987. 3.2

[PD71] A. S. Pine and G. Dresselhaus. Raman Spectra and Lattice Dynamics of Tellurium. *Phys. Rev. B*, 4:356–371, Jul 1971. 4.6.1

[PFG01] H. Preis, K. Fuchs, and W. Gebhardt. In-Situ RHEED Study of the Growth Mechanisms of CdSe Quantum Dots. *physica status solidi (b)*, 224(2):527–530, 2001. 4.1

[PRB+91] O. Pagès, M. Renucci, O. Briot, N. Tempier, and R.L. Aulombard. Raman characterization of ZnSe/GaAs MOVPE heterostructures. *Journal of Crystal Growth*, 107(1-4):670 – 673, 1991. <ce:title>Metalorganic Vapor Phase Epitaxy 1990</ce:title> <xocs:full-name>Proceedings on Metalorganic Vapor Phase Epitaxy and workshop on MOMBE, CBE, GSMBE, and related techniques</xocs:full-name>. 5.1

[PRG+00] N. Peranio, A. Rosenauer, D. Gerthsen, S. V. Sorokin, I. V. Sedova, and S. V. Ivanov. Structural and chemical analysis of CdSe/ZnSe nanostructures by transmission electron microscopy. *Phys. Rev. B*, 61:16015–16024, Jun 2000. 4.3, 4.7

[RAB+06] Ivan-Christophe Robin, Regis Andre, Catherine Bougerol, Thomas Aichele, and Tatarenko Serge. Elastic and surface energies: Two key parameters for CdSe quantum dot formation. *Appl. Phys. Lett.*, 88:233103, 2006. 4.4

[RCC+91] Benjamin Rockwell, H. R. Chandrasekhar, Meera Chandrasekhar, A. K. Ramdas, M. Kobayashi, and R. L. Gunshor. Pressure tuning of strains in semiconductor heterostructures: (ZnSe epilayer)/(GaAs epilayer). *Phys. Rev. B*, 44:11307–11314, Nov 1991. 4.6.2

[Ric76] W. Richter. Resonant Raman Scattering in Semiconductors, 1976. Springer Tracts in Modern Physics 78. 2.1

[RLH98] M. Rabe, M. Lowisch, and F. Henneberger. Self-assembled CdSe quantum dots Formation by thermally activated surface reorganization. *Journal of Crystal Growth*, 184-185:248 – 253, 1998. 4.3, 4.3.2

[RMG+99] Fiederling R., Keim M., Reuscher G., Ossau W., Schmidt G., Waag A., and Molenkamp L. W. Injection and detection of a spin-polarized current in a light-emitting diode. *Nature*, 402:787 – 790, 1999. 5.1

[RSL00] Patrik Recher, Eugene V. Sukhorukov, and Daniel Loss. Quantum Dot as Spin Filter and Spin Memory. *Phys. Rev. Lett.*, 85:1962–1965, 2000. 1

[RZ98] Dietrich R.T. and Zahn. Raman monitoring of wide bandgap mbe growth. *Applied Surface Science*, 123-124(0):276 – 282, 1998. <ce:title>Proceedings

of the Sixth International Conference on the Formation of Semiconductor Interfaces</ce:title>. 5.1

[S.82] Blakemore J. S. Semiconducting and other major properties of gallium arsenide. *J. Appl. Phys.*, 53:R123, 1982. 4.6.2

[SDH+00] M. Strassburg, M. Dworzak, A. Hoffmann, R. Heitz, U.W. Pohl, D. Bimberg, D. Litvinov, A. Rosenauer, D. Gerthsen, I. Kudryashov, K. Lischka, and D. Schikora. Resonant Gain in ZnSe Structures with Stacked CdSe Islands Grown in Stranski-Krastanov Mode. *physica status solidi (a)*, 180(1):281–285, 2000. 4.1

[SKI+08] G. Shigaura, M. Kanamori, Y. Ichinohe, K. Kyoh, K. Honma, Na. Kimura, No. Kimura, T. Sawada, K. Suzuki, and K. Imai. Photoluminescence of a Periodic Alloy of ZnSeTe Grown by Using MBE. *Journal of the Korean Physical Society*, 53(1):179–182, 2008. 4.5.1

[SOP92] Khalid Shahzad, Diego J. Olego, and John Petruzzello. Optical and vibrational properties of doped zinc selenide epitaxial layers. *Journal of Luminescence*, 52(1-4):17 – 39, 1992. 5.1

[SOVdW88] Khalid Shahzad, Diego J. Olego, and Chris G. Van de Walle. Optical characterization and band offsets in ZnSe-ZnS_xSe_{1-x} strained-layer superlattices. *Phys. Rev. B*, 38:1417–1426, Jul 1988. 4.6.2

[TIT+95] N. Takojima, Y. Ishizuka, I. Tsubono, N. Kimura, K. Suzuki, T. Sawada, and K. Imai. Green emission enhanced by Te isoelectronic traps in ZnSe grown by molecular beam epitaxy. *Journal of Crystal Growth*, 150:770–774, 1995. 4.5.1

[TSS+05] A. A. Toropov, I. V. Sedova, S. V. Sorokin, Ya. V. Terent'ev, E. L. Ivchenko, and S. V. Ivanov. Resonant spin-dependent electron coupling in a iii-v/ii-vi heterovalent double quantum well. *Phys. Rev. B*, 71:195312, May 2005. 5.1

[TSS+06] A. A. Toropov, I. V. Sedova, S. V. Sorokin, Ya. V. Terent'ev, E. L. Ivchenko, D. N. Lykov, S. V. Ivanov, J. P. Bergman, and B. Monemar. Iii–v/ii–vi heterovalent double quantum wells. *physica status solidi (b)*, 243(4):819–826, 2006. 5.1

[Veg21] L. Vegard. Die Konstitution der Mischkristalle und die Raumfüllung der Atome. *Zeitschrift für Physik A: Hadrons and Nuclei*, 5(1):17–26, January 1921. 3.2

[WHW+02] F J Wang, D Huang, X J Wang, X X Gu, and G C Yu. Carrier effects on Raman spectra from ZnSe/GaAs heterostructures. *Journal of Physics: Condensed Matter*, 14(21):5419, 2002. 5.1

[WWG+02] V. Wagner, J. Wagner, S. Gundel, L. Hansen, and J. Geurts. Chemical surface analysis by raman spectroscopy utilizing dimer vibrations. *Phys. Rev. Lett.*, 89:166103, Sep 2002. 4.6.1

[WWH+03] J. W. Wagner, V. Wagner, L. Hansen, G. Schmidt, J. Geurts, P. Vogt, N. Esser, and W. Richter. Preparation of different BeTe surface reconstructions by decapping and thermal treatment. *J. Appl. Phys.*, 93(3):1511 – 1514, 2003. 4.6, 4.6.1

[YC01] P. Yu and M. Cardona. *Fundamentals of Semiconductors.* Springer, New York, 3rd edition, 2001. 2.1, 2.2, 2.2, 2.4, 2.4, 2.4

[YNO+02] Y.-M Yu, S Nam, Byungsung O, K.-S Lee, P.Y Yu, Jongwon Lee, and Y.D Choi. Strain effect in ZnSe epilayers grown on GaAs substrates. *Journal of Crystal Growth*, 243(3-4):389 – 395, 2002. 5.1

[ZTHH01] X. B. Zhang, H. L. Tsoi, K. L. Ha, and S. K. Hark. Raman scattering studies of the ZnSe/GaAs interface. *Journal of Raman Spectroscopy*, 32(10):852–856, 2001. 5.1

Publications

- *"CdSe/ZnSe quantum dots formed by low temperature epitaxy and in-situ annealing: properties and growth optimization"*, Suddhasatta Mahapatra, Claus Schumacher, Tobias Kiessling, Georgy Astakhov, Utz Bass, Wolfgang Ossau, Jean Geurts and Karl Brunner, Acta Physica Polonica A 108, 769 (2005)

- *"Comparative study of self-assembled CdSe/ZnSe quantum dots grown by variants of conventional MBE"'*, Suddhasatta Mahapatra, Karl Brunner, Claus Schumacher, Tobias Kiessling, Georgy Astakhov, Utz Bass, Emanuela Margapoti, Wolfgang Ossau, Jean Geurts, Lukas Worschech, Alfred Forchel, and Laurens W. Molenkamp, Phys. Stat. Sol. (c) 3, 928 (2006)

- *"Analysis of lattice dynamics and magnetic properties of II-VI layers and interfaces by Raman spectroscopy"'*, Jean Geurts, Utz Bass, Michael Lentze, and Veit. Wagner, Phys. Stat. Sol (c) 4, 3297 (2007)

- *"CdSe/ZnSe heteroepitaxy: Aspects of growth and self-organization of nanostructures"*, S. Mahapatra, T. Kiessling, G. V. Astakhov, J. Renner, U. Bass, C. Bougerol, T. Schmidt, A. Bendounan, F. Schmitt, C. Schumacher, L. Worschech, W. Ossau, J. Geurts, L. W. Molenkamp, F. Reinert, A. Forchel, and K. Brunner, Phys. Stat. Sol. (c) 4, 9, 3129-3149 (2007)

- *"Band offsets and band bending at heterovalent semiconductor interfaces"*, Alex Frey, Utz Bass, Suddhassatta Mahapatra, Claus Schumacher, Jean Geurts, and Karl Brunner, Phys. Rev. B 82, 195318 (2010)

- *"Analysis of the depletion layers and conduction band barrier at the n-ZnSe / n-GaAs interface for different growth start procedures"*, Utz Bass, Jean Geurts, Alex Frey, Suddhasatta Mahapatra, Claus Schumacher, and Karl Brunner, Phys. Stat. Sol (c), submitted

Conference contributions

- *"Raman spectroscopy of embedded semiconductor monolayers: CdSe in BeTe and ZnSe"*, Utz Bass, Suddhasatta Mahapatra, Tobias Muck, Veit Wagner, Karl Brunner, and Jean Geurts, Beitrag zur Konferenz, Frühjahrstagung der Deutschen Physikalischen Gesellschaft 2005, DS 18.5

- *"Comparative Study of Self-assembled CdSe/ZnSe Dots Grown by Variants of Conventional MBE"*, Suddhasatta Mahapatra, Claus Schumacher, Tobias Kiessling, Georgy Astakhov, Utz Bass, Jean Geurts, Wolfgang Ossau, Karl Brunner, Beitrag zur 12th International Conference on II-VI Compounds 2005, Warschau

- *"Cd-loss of CdSe quantum dots in ZnSe during MBE growth"*,Utz Bass, Jean Geurts, Fabian Eschenbach, Suddhasatta Mahapatra, and Karl Brunner, Beitrag zur Konferenz, Frühjahrstagung der Deutschen Physikalischen Gesellschaft 2008, HL 31.36

- *"Optical spectroscopy study of c(4x2) Ge (001)-surfaces, covered with atomic Au wires"*, Utz Bass, Eugen Speiser, Sebastian Meyer, Jörg Schäfer, Norbert Esser, and Jean Geurts, Beitrag zur Konferenz, Frühjahrstagung der Deutschen Physikalischen Gesellschaft 2011, HL

- *"Raman study of band-bending at ZnSe/GaAs(001) interfaces"*, Utz Bass, Alex Frey, Suddhasatta Mahapatra, Claus Schumacher, Karl Brunner, and Jean Geurts, Frühjahrstagung der Deutschen Physikalischen Gesellschaft 2011, HL

Danksagung

Viele Personen haben in direkter oder indirekter Weise zum Entstehen dieser Dissertation beigetragen. Ohne Anspruch auf Vollständigkeit und auch ohne eine wertende Reihenfolge einzuhalten möchte ich mich bei folgenden Personen bedanken:

- Laurens W. Molenkamp, an seinem Lehrstuhl diese Dissertation anzufertigen und von den breiten Ressourcen im Lehrstuhl zu profitieren.
- Meinem Doktorvater, Prof. Dr. Jean Geurts, für die Möglichkeit der Erstellung dieser Dissertation in seiner Arbeitsgruppe. Besonderer Dank gebührt den Gesprächen und Diskussionen über Physik und die Welt und seinen didaktisch sehr wertvollen Erklärungen der zum Teil sehr komplizierten Aspekten in der Physik.
- den Mitgliedern der Aggeurts, insbesondere natürlich bei Constantin Weiler der im Rahmen seiner Zulassungsarbeit sehr viel Zeit in die Messungen zu den ungecappten Proben verwendet hat und bei Dr. Sven Issing für Aufnahme der IR-Reflektionsspektren.
- der AGOssau für die Bereitstellung der Tieftemperatur Photolumineszenz Spektren und die Diskussion über diese. Hierbei möchte ich im Besonderen Dr. Tobias Kiessling, Jan Hendrik May und natürlich Sepp Ossau erwähnen.
- der AGBrunner für die MBE Proben. Besonders natürlich bei den "Wachsern"der Proben: Sudhassatta Mahapatra, Fabian Eschenbach und Alex Frey.
- Prof. Khellil (Khaled) Bouamama für die ab-inito DFT Berechnungen der Schwingungsfrequenzen. Hier möchte ich mich auch bei Dr. Andrzej Fleszar bedanken der aufgrund seiner Erfahrung mit den Pseudopotentialen eine sehr grosse Hilfe bei der Auswahl dieser war.
- beim technischen Support des Gelb/Reinraum Teams, namentlich Petra Wolf-Müller, Anita Gebhard und Volkmar Hock. Ohne ihre Hilfe bzw. ihr technisches Knowhow wären einige Experimente im Rahmen dieser Arbeit nicht oder nicht so schnell gelungen.
- bei den Leuten aus der Mechanik- und Elektronik-Werkstatt und der Heliumverflüssigung, die mir sehr hilfreich waren bei Konzeption, Bau und Reparatur von Versuchsaufbauten und Laboreinreichtung und die mir immer die Fragen zu den CAD-Zeichnungen beantworten konnten. Im Besonderen möchte ich hier Rainer Brauner, Roland Ebert, Heinz Rüb und Franz Krause erwähnen.

- der Kaffeerunde für die Gespräche und Diskussionen.
- der IT-Crowd, Andreas Klein und Andreas Vetter.
- den Sekretärinnen Anja Brück-Poirier und Angelika Berger die immer eine grosse Hilfe bei der Bewältigung des Verwaltungsaufwandes waren.
- der Sekretärin Moni Seiffer im Rahmen meiner Arbeit in der Forschergruppe FOR1162. Sie hat mich sehr effektiv vor Korruptionsformularen u.ä. beschützt.
- bei meinen Eltern die mich all die Jahre unterstützt haben.